DYNAMICS OF ELEVATED JACK-UP STRUCTURES

1971

DYNAMICS OF ELEVATED JACK-UP STRUCTURES

PROEFSCHRIFT

Ter verkrijging van de graad van doctor
aan de Technische Universiteit Delft,
op gezag van de Rector Magnificus,
prof. drs. P.A. Schenck,
in het openbaar te verdedigen
ten overstaan van een commissie
aangewezen door het College van Dekanen
op donderdag 31 oktober 1991 te 14.00 uur

door

Ping Liu

geboren te Chengdu, China

civiel ingenieur

DELFT UNIVERSITY PRESS/1991

Dit proefschrift is goedgekeurd door de promotoren
prof. ir. J.G. Wolters en prof. dr. ir. J. Blaauwendraad

Published and distributed by:

Delft University Press
Stevinweg 1
2628 CN Delft
The Netherlands

Telephone +31 15 783254
Fax +31 15 781661

ISBN 90-6275-731-6 / CIP

Printed in The Netherlands

To:

my parents, Chong-guang and Guang-jiu

my educators, Prof. L. Li and Prof. Z. Zheng

my friends, the Massie family and the Spanjaard family

TABLE OF CONTENTS

Chapter 1
Introduction

Common offshore units can be categorized into two types: fixed structures (such as jacket platforms and gravity platforms) and mobile structures (drill barges, drill ships, semisubmersibles, for example). The fixed structures are held stable either by piles or their own weight, providing ultimate stability for offshore operations. The mobile structures maintain their locations at the sea by either anchoring or dynamic positioning, offering mobility and reusability. Combining the advantages of the above two concepts, a jack-up rig is a hybrid type platform with both stability and mobility. Basically, a jack-up is a self-elevating pontoon with retractable legs. When the legs are pulled up by means of a jacking mechanism, the jack-up rig is effectively a barge and can be towed by tugboats or carried by a heavy transport vessel to another location. When the pontoon is elevated above the sea level with legs extended down to the sea bed, the rig enters the platform mode (elevated operation condition), furnishing a relatively steady and stable working place offshore. Because of this unique combination of properties, jack-up platforms have been used extensively in the offshore industry for more than 30 years. There are about 440 of them at present, engaged primarily in hydrocarbon drilling operations.

The present work was carried out as a part of a Delft University of Technology Jack-up Project conducted by the Workgroup Offshore Technology (*WOT*), with objective to increase the detailed knowledge of the behavior of such platform components as well as the prediction of the overall structure's elevated behavior and (remaining) lifetime.
The need for such a study is demonstrated by the relatively high rate of structural failure for jack-up rigs as compared to fixed platforms and the considerable discrepancy existing among present various industry assessment methods and criteria for elevated jack-up platforms. The failure statistics of jack-up platforms based upon data from the Worldwide Offshore Accident Databank shows that jack-up platforms are at least 20 times more 'accident-prone' than fixed offshore structures. Additionally, when the present program was initiated in 1988, the industry criteria and procedures then in use were so inconsistent that they could easily result in failures rates which differ by a factor of 50 to 100 - see Efthymiou (1988). (References are listed in the text by author and year; a more complete reference list is to be found at the end of the main text of the

dissertation.) The reasons for this seem to be rooted in too simple an approach to the computational schematization of such platforms for design or evaluation purposes. Since then, considerable efforts from the worldwide jack-up industry have been made to bring about some degree of harmonization for the jack-up assessment. While a substantial consensus has been achieved after three years of joint industry activity, a spectrum of questions remain to be answered - see Anon (1990). Further investigations on various aspects such as spudcan fixity, hydrodynamic coefficient determination, assessment criteria selection, etc. are still to be carried out - see Anon (1991).
With jack-ups venturing into deeper water - say 130 m or more - for longer term use such as for production from marginal fields in more exposed locations, the adequate performance assessment and analysis of these platforms become even more crucial. Since such large jack-up structures are much less rigid, when compared with fixed platforms, dynamic effects can be expected to become remarkably more important. This will be true for survival condition analyses and especially for fatigue analyses. Additionally, the natural frequency of such rigs in sway can enter an energy-rich exciting wave frequency band. This, combined with dynamic influences, is expected to make overall structural responses even greater and damping precision critical.

1.1 TOTAL PROBLEM SURVEY

Numerous investigations have been conducted to analyze the dynamic behavior of elevated jack-up platforms and assess their structural safety - see, for example, Anon (1981 - 1983 and 1989), Brekke *et al.* (1989 and 1990), Lagers (1990), Leijten and Efthymiou (1989), Sliggers (1990), etc. The total jack-up durability problem definition and associated literature study were carried out in the earlier phase of this project by Massie, Liu and Boon (1989). They came to the conclusion that elevated jack-up platforms can be significantly nonlinear in their dynamic structural behavior. The most important of these involve interactions of the legs with:

the sea bed via a spudcan,
the deck via the deck-leg clamping system, and
the sea itself: waves and currents acting on the moving structure.

Within the TU Delft Jack-up Project a series of investigations have been performed to attack these various nonlinear interaction problems. For spudcan-soil interaction, the readers are referred to Holtrop (1989), Spaargaren (1989), Stuit (1989), and Klaver (1990), for deck-leg interaction Gründlehnler (1989) and Michels (1990), for

hydrodynamic interaction Spaarman (1989), Zeelenberg (1990) and Massie, Liu and Zeelenberg (1991). An overview of the progresses made so far in this program has been given by Massie and Liu (1990).

Another report by Liu (1989) inventoried and compared the (mathematical) methods available for the analysis of jack-up platforms. It was concluded that the extrapolated use of traditional analysis methods (such as quasi-static approach, design wave approach, etc) is no longer sufficiently dependable for predicting the nonlinear behavior of elevated jack-up rigs. A more advanced, stochastic, nonlinear, dynamic, time domain analysis approach must be chosen to simulate the nonlinear physical response of a jack-up platform.

1.2 SCOPE OF WORK

While retaining the overall vision of the total jack-up durability problem, the author's work has been concentrated on the investigation of the influence of hydrodynamic and structural nonlinearities on elevated jack-up rigs. The hydrodynamic study focuses on the wave load on legs. The influences of currents are not included in the present work. The examination of the structural nonlinearities concentrates on the jack-up structure itself; its interaction with soil is excluded from the present study.
The research was done following two tracks: On the one hand model tests on the jack-up platforms were carried out, and these were complemented on the other hand by numerical modeling of such rigs.

The different test models have been chosen such that they segregate the several types of hydrodynamic and structural nonlinearities. As for hydrodynamics the influence of drag is important and the question arises whether one should use the absolute motion of the water particles or the relative motion between leg and water particles to compute the hydrodynamic loads on the legs. The structural nonlinearities came from the leg-deck connection and possibly the P-δ effect (second order effect). The physical models were tested in both regular and irregular waves.

The numerical simulation required the development of a software package that accounts for the nonlinear hydrodynamic interaction and nonlinear structural behavior. As explained before, this program starts from a time domain approach.

Not restricted to simulating the behavior of the present physical models only, the software development is aimed to make available a more precise, verified, dependable and commonly accepted computational model, that will make it possible to properly and conveniently evaluate less exact but more efficient routine procedures for jack-up analysis and assessment. The first validation of this computational model was done using the experimental data from the present tests.

The mere fact that a numerical simulation will be successful does not necessarily mean that it is understood which nonlinearities are dominant and under which circumstances. To gain such insight the random wave test data were analyzed in two ways: Probability analysis was performed to study the distortion of statistical distributions caused by nonlinearities; frequency analysis exposed the influences of nonlinearities on the energy distribution and helped determine which nonlinearities had major impact on the system behavior. The software developed for these analyses is also supported by a responsible error analysis in both the probability and the frequency domain.

In conclusion, the work presented in this dissertation includes the following three aspects:

- Software Development
  Two software packages have been developed for the project: (1) *NOSDA* simulation software for the *N*onlinear *O*ffshore *S*tructure *D*ynamic *A*nalysis; (2) *RANDA* software for *RAN*dom *D*ata *A*nalysis. These codes are briefly described in Chapter 2.

- Physical Model Tests
  Testing on three jack-up models was carried out in the wave tank of the Ship Hydromechanics Laboratory, TU Delft. The models were not scaled to reproduce actual field conditions exactly but they do retain the some important characteristics of prototypes. The models and test program are discussed in Chapter 3.

- Experimental Result Analysis and Computer Simulations
  The processing of the measured data from the irregular wave tests was supported by a careful error analysis using *RANDA* software. The model tests in regular and irregular waves were simulated using *NOSDA* software. The experimental data analyses and associated computer simulations are presented in Chapter 4 through 7.

The main conclusions of entire work are presented in Chapter 8.

This dissertation is structured in such a way that whenever possible, the main body of the text is kept concise and descriptive; only the principles and essential results are presented. The detailed data and mathematics are described in the appendices.

1.3 NOTATION

The present work lies on the interface between disciplines such as hydrodynamics and structural mechanics (inclusion of statistical analysis complicates the notation system further). Each of these disciplines has its own, independent notation convention; it is unavoidable that they conflict at times. Compromises in notation are necessary in this dissertation. Consistency has been maintained, however, and - where possible - with an international standard. A symbol table is included at the end of the main text of the dissertation.

Chapter 2
Software development

Two software packages have been developed and used as computational tools for this study: *NOSDA* and *RANDA*. A principle description of each package is given in the remainder of this chapter.

2.1 *NOSDA* PACKAGE

NOSDA was developed as a special purpose software package for stochastic, nonlinear, dynamic analysis of offshore structures. More details of this software have been documented in a separate report by Liu and Massie (1988).
The structural analysis kernel of this software package has a strong heritage in another nonlinear dynamic analysis program, *TILLY*, developed by the Mechanics and Structures Department within the Faculty of Civil Engineering of the TU Delft - See Blaauwendraad (1989).

The dynamic analysis is performed in the time domain so that various types of nonlinearities associated with jack-up dynamic behavior mentioned in Section 1.1 can be accommodated. These nonlinearities can result from fluid particle kinematics, material properties, geometric deformations, fluid-structure and soil-structure interactions. A principle flowchart of *NOSDA* is included in figure 2.1.

The primary uniqueness of *NOSDA* involves the computation of hydrodynamic forces on a moving structure in waves and/or currents.
As the price of its precision and flexibility, *NOSDA* shares the disadvantage of all time domain nonlinear dynamic programs - they are computer time costly.
The *NOSDA* software is used as the computer simulation tool in Chapters 6 and 7. Some details of the implementation of *NOSDA* are also to be found in these chapters.

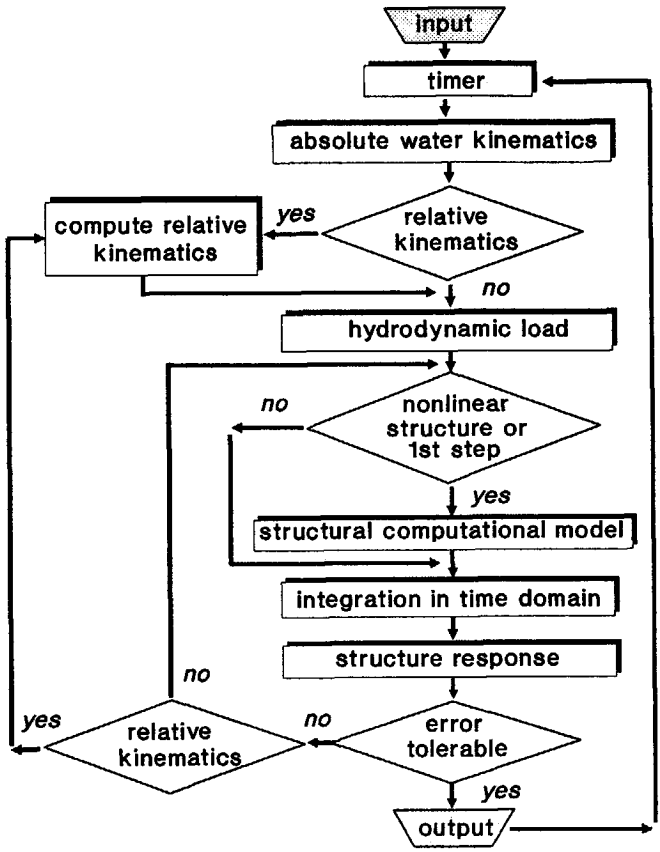

Figure 2.1 Principle Flowchart of NOSDA

2.2 *RANDA* PACKAGE

The *RANDA* software analyzes random data in the both probability domain and the frequency domain.

The *probability analysis* involves the computation of the statistical distributions of instantaneous values, peak values and extreme values of measured data at different transfer steps (wave elevation - wave kinematics - hydrodynamic loads - global structural response - detailed structural response, for example). Existence of nonlinearities will cause distortion in the statistical distributions from one step to another. The probability analysis results provide information about how the energy is distributed among the motion levels. Knowledge of the distortion caused by nonlinearities and thus the

resulting response distribution after each transfer step is important for both extreme and fatigue analysis of a jack-up.

The *frequency analysis* examines the autospectral properties of an individual measured time series and cross-spectral properties between two time series. With a nonlinear system the cross-spectral quantities will generally not be invariant, instead, they will be dependent upon the input energy level as well as energy distribution. The spectral analysis results shed light on the energy distributions and their transfer relationship as a function of frequency.

The random data processing in both domains mentioned above is supported by a responsible *error analysis*. This associated error estimate procedure is often essential for such type of analysis, since an irresponsible processing can cause so big an error in the results that any attempt to interpret them becomes totally meaningless.

A principle flowchart of the *RANDA* software is shown in figure 2.2. The two routes on the left hand side of the flowchart (namely, the spectral analysis and probability analysis) are employed for the random data analysis in Chapter 7. More details about this software package have been given by Liu (1991).

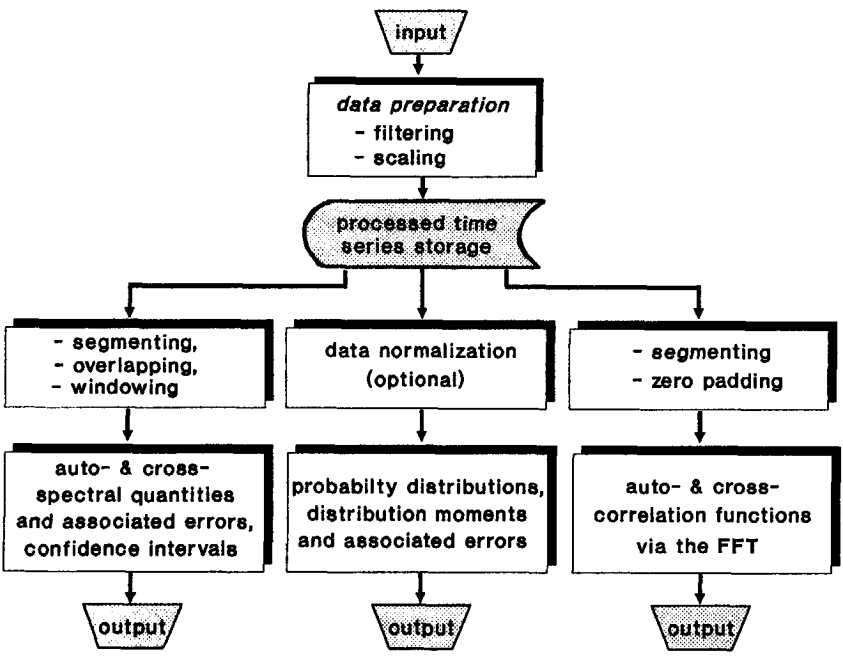

Figure 2.2 Principle Flowchart of RANDA

Chapter 3
Physical model tests

3.1 MODELS AND TEST SETUP

Two principle physical models of three-legged jack-up structures - named Model I and Model II, respectively - were designed and fabricated. These were tested in Towing Tank I of the Ship Hydromechanics Laboratory of the Faculty of Mechanical Engineering and Marine Technology. These tests were carried out using instrumentation from and by personnel of this laboratory.
These models each had three identical circular cylindrical legs. Model I was designed with relatively large diameter legs yielding inertia-dominated hydrodynamic forces; Model II had more slender legs and thus more drag-dominated forces.
For each model, the deck was placed about 2.4 m above the tank bottom and was assumed to be relatively rigid with (initially designed) completely clamped deck-leg connections.
The legs were hinged at their lower end with force meters located between the hinges and the model base plate on the tank floor.
A convenient tank water depth, d, was 2.0 m.

Additional testing of Model II with extra deck masses - then denoted as Model II-M - was carried out to expose the effects of deck load eccentricity - the P-δ effect and the effects of a variation in the natural period of the model. Figure 3.1 illustrates the model geometry.

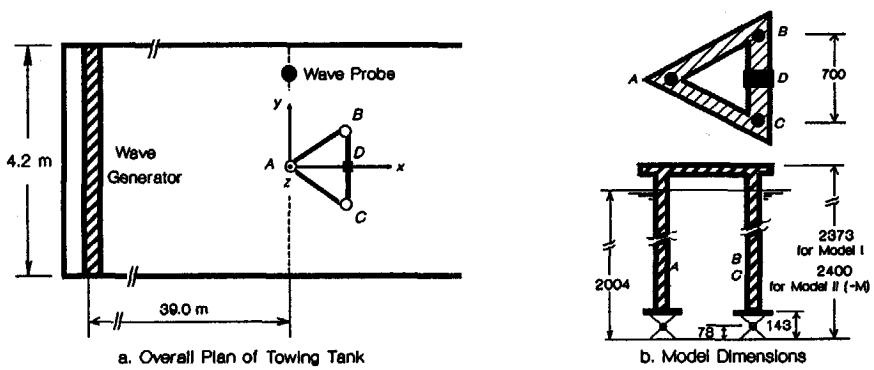

Figure 3.1 Physical Model Setup

The coordinate system is chosen as follows: The origin is located at the base of the bow leg, the x-axis is directed along the tank (away from the wavemaker), the z-axis is vertical (positive upwards) and the y-axis is perpendicular to the x-z plane according to a right-hand axis rule.
Necessary simplifications were made in the model design to concentrate attention on the physical processes to be studied. While some discussion of model scales is relevant, no attempt has been made to reproduce actual field conditions in the models. Instead, the physical models should be seen as full scale structures, themselves.

The structure's natural frequency, f_n , was chosen to be around 1 Hz for both Model I and Model II (the natural frequency of Model II-M became considerably lower due to the extra deck mass). The model leg spacing was chosen to include a reasonable hydrodynamic force cancellation effect. The design approach, further, was to choose the leg stiffness such that the model platform has a quasi-static deflection of 2% of the water depth at deck level if the peak force resulting from a design wave was applied to all 3 legs simultaneously. By choosing different leg materials and adjusting deck masses, it proved possible to essentially retain the natural frequency and quasi-static deflection (as outlined above) while using two quite different types of legs. The most important physical parameters for each of the three models are listed in table 3.1.
More details of the model set-up and test program can be found in a separate report by Journée *et al.* (1988).

Three dynamometers were mounted at the base of each leg to measure the force components along three axes. The forces measured by the dynamometers were labeled as F_{Ax} , F_{Ay} , F_{Az} , F_{Bx} , F_{By} , F_{Bz} , F_{Cx} , F_{Cy} and F_{Cz} , where the first subscript denotes the location of the dynamometers - see figure 3.1 - and the second refers to the direction.

A 5-g accelerometer was mounted at location D on the deck to measure x and y components of the acceleration there, $\ddot{u}_D$ and $\ddot{v}_D$. (Note that the displacements along the x, y and z axes are denoted as u, v and w and the associated subscripts indicate the location.)
Additionally, the horizontal displacements of the deck were measured at locations A and C, denoted by u_A , v_A , u_C and v_C so as to doublecheck the acceleration measurements and detect possible rotations around the vertical axis.

A two-wire conductance wave probe was mounted adjacent to the platform in the same line perpendicular to the tank wall as the windward leg A. This wave elevation was indicated by η_A .

Table 3.1 Physical Parameters of the Three Models

Item	Model I	Model II	Model II-M	Unit
Construction mass	18.20	5.90	5.90	kg
Additional deck mass	15.72	0.52	3.67	kg
Total model mass	33.92	6.42	9.57	kg
Deck material	alum./PVC	aluminum	aluminum	-
Leg material	hard PVC	red copper	red copper	-
Leg stiffness, *EI*	2118.0	133.1	133.1	$N.m^2$
Deck-leg connection	clamped	clamped	clamped	-
Leg-bottom connection	hinged	hinged	hinged	-
Leg outer diameter	0.090	0.016	0.016	m
Leg spacing (triangular)	0.700	0.700	0.700	m
Elevation from tank floor:				
Deck (topside)	2.373	2.403	2.403	m
Displacement meter	2.373	2.403	2.403	m
Accelerometers	2.373	2.403	2.403	m
Still water surface	2.004	2.004	2.004	m
Leg cylinder base	0.143	0.143	0.143	m
Leg hinge	0.078	0.078	0.078	m
Natural freq., f_n , (approx.)	0.87	0.80	0.50	Hz

3.2 TEST PROGRAM

The model testing program included exposing the models to regular and irregular uni-directional, long crested waves as well as static and free vibration tests. As a special case, some tests were completed with a superposition of two regular waves. The experiments of this type in the past have often been concentrating on the regular wave situation. Inclusion of irregular wave tests will help gain insight into the jack-up behavior in a real random sea.

Totally 230 wave runs were carried out (including 9 runs for the instrumentation control). The duration of each regular wave run was about 5 minutes (excluding transient motion) and that of each irregular wave run was about 20 minutes.

All of the experimental data were recorded in an analog form on magnetic tapes (*IR* recorder). Some data were also recorded on paper using a *UV* recorder. The *UV* recording provides sufficient data for further processing with the static, free vibration and regular wave tests, while before the irregular wave test results can be processed and analyzed the analog data on the tapes need to be digitized.

The static tests were carried out for each model by exerting static, horizontal loads at the deck level and recording the corresponding displacements.
The free vibration tests were carried out by giving a initial displacement at deck level then releasing the deck and recording the deflection trace.

During the model testing the pen recorder and analog magnetic tape recorder were connected in parallel to the sensors; the visual observation of the trace on paper could not guarantee the quality of recording on the magnetic tape. When digitizing the data on the tapes, severe truncations have been found in the recorded data with paired regular waves; no effort has, therefore, been dedicated to process this group of data further.

With regular wave tests, possible wave frequencies in the basin range from about 0.6 to 1.3 Hz with wave heights up to 0.080 m. (Higher frequencies were reached for lower

wave heights). The three models were tested in 103 regular wave runs. The wave states used are listed in table 3.2.

In the tests, the wave heights actually generated were often slightly different from their nominal values listed in the table. The measured wave heights were used in the later analysis.

Table 3.2 Regular Waves Tested

Model No.	Run No.	Nominal Height, H (cm)	Wave Frequency, f (Hz)
I	15 - 50	2	0.7 - 1.7
		4	0.7 - 1.2
		6	0.7 - 1.1
II	78 - 123	4	0.6 - 1.2
		6	0.5 - 1.15
		8	0.5 - 1.0
		12	0.5 - 0.8
II-M	162 - 182	4	0.55 - 0.8
		6	0.3 - 0.9
		8	0.3 - 0.7

36 successful irregular wave runs were performed with the three models: runs 55 through 63 for Model I, runs 133 through 140 for Model II and runs 210 through 218 for Model II-M. Truncations - especially in the wave elevation channel - occurred also in a few runs with this group of tests. Excluding the truncated runs, 22 wave state combinations listed in table 3.3 were analyzed in the present study (in the table H_s is the significant wave height and f_p the peak frequency.)

Table 3.3 Irregular Waves Tested

Model I			Model II			Model II-M		
Run no.	H_s (cm)	f_p (Hz)	Run no.	H_s (cm)	f_p (Hz)	Run no.	H_s (cm)	f_p (Hz)
55	3.154	0.800	141	3.216	0.739	210	2.328	0.739
56	4.444	0.800	143	2.262	0.739	211	3.300	0.778
57	3.928	0.800	144	2.384	0.856	212	4.622	0.739
58	2.930	0.800	145	3.388	0.817	215	4.906	0.661
59	3.490	0.800	147	2.610	0.934	216	3.160	0.545
60	3.992	0.800	149	5.204	0.895			
61	3.356	0.800	151	5.852	0.817			
62	3.894	0.800	152	6.300	0.934			
63	4.300	0.800						
Range	2.930 ↓ 4.444	0.800 ↓ 0.800		2.262 ↓ 6.300	0.739 ↓ 0.934		2.328 ↓ 4.906	0.545 ↓ 0.778

3.3 TYPICAL RESULTS

Only a small representative part of the test results will be presented here, more results are to be presented in the following chapters.
The static test results are plotted as force (exerted at the deck level) versus (deck) displacement. An example is given in figure 3.2.

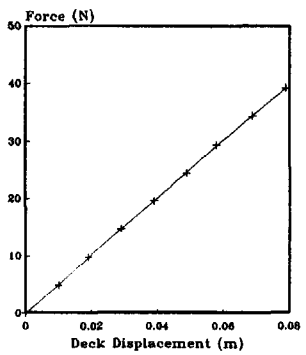

Figure 3.2 Measured Overall Static Constitutive Relation (Model I)

The free vibration tests result in decay curves such as shown in figure 3.3.

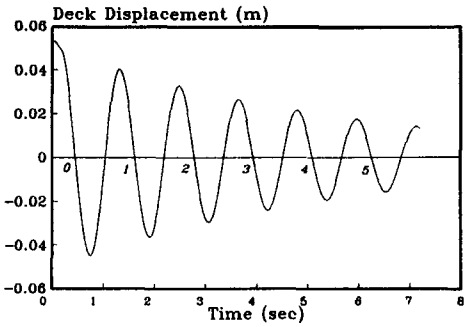

Figure 3.3 Free Vibration Trace Record in Air (Model I)

As an example, the Response-Amplitude-Operator (RAO) curves of Model I for different wave heights derived from regular wave tests are superimposed in figure 3.4. The RAOs in the regular wave case are determined by normalizing the deck displacement amplitude with respect to the input wave amplitude.

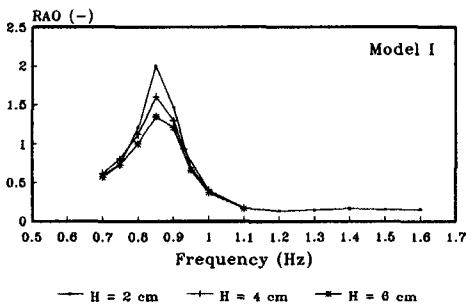

Figure 3.4 Measured RAOs for Deck Displacement with Various Wave Heights (Regular Waves)

As the typical results from the spectral analysis of the irregular wave test data, a wave elevation spectrum, its corresponding deck displacement spectrum and the associated RAO curve are presented in figure 3.5. The RAO with irregular waves is defined as the gain factor between the wave elevation and the deck displacement. (A gain factor is the modulus of the frequency response function which is determined here as the cross-spectrum divided by the input spectrum). The notation system as shown in this figure will be used frequently in the graphic presentations later in this dissertation: the

horizontal-axis is the frequency, f; the solid curve is the value of interest (the spectrum, gain factor, coherence function, and so forth), embraced by the 95% confidence interval (shown in the figure as the two fine dashed curves); and the coarse dashed curve down at the bottom of the figure is the normalized random error as a percentage. In the figure (-) denotes that the quantity is dimensionless. $G_{\eta\eta}$ is the wave spectrum, G_{uu} is the deck displacement spectrum and ε_r is the normalized random error.

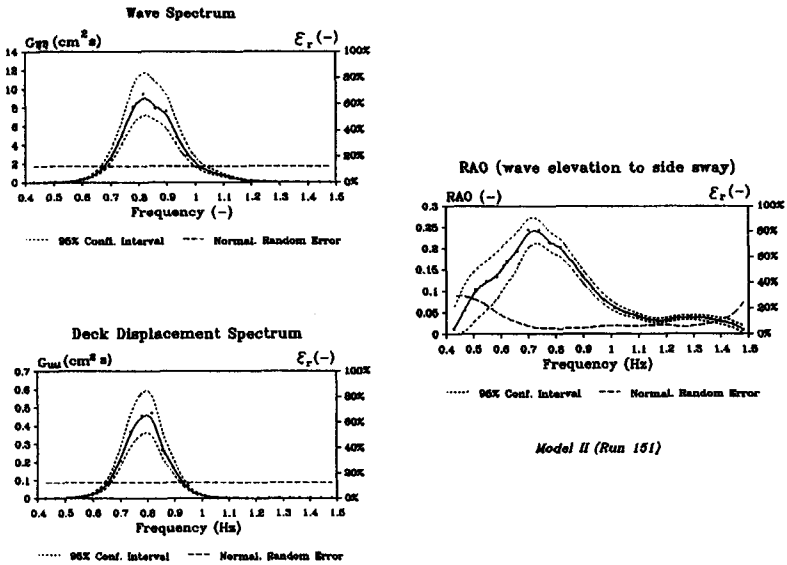

Figure 3.5 Measured Wave Spectrum, Deck Displacement Spectrum and Derived RAOs

Chapter 4
Static and free vibration test analysis

The data resulting from the static tests and free vibration tests in air are analyzed in this chapter. The results will be used to shed light on the establishment of the structural computational models in Chapter 6. Many global properties of the models such as structural stiffnesses, damping ratios, natural periods, etc., are derived from these two groups of tests.

4.1 STATIC STIFFNESS

The global lateral stiffness of each model (defined as the force exerted at the deck level divided by the resulting deck displacement) from static tests, K_s , is listed in table 4.1. - more detailed data are given in Appendix I.

Table 4.1 Model Static Stiffnesses

Model No.	Model I	Model II	Model II-M
Static Stiffness, K_s (N/m)	508.00	19.90	16.82

The only difference between Model II and Model II-M is that Model II-M has extra deck mass and therefore extra P-δ effect. The P-δ effect reduces overall structural stiffness; this is confirmed by the larger stiffness of Model II in the above table.
Note that the static stiffness of Model I in the table is calculated from the test data before the deck to leg connection of this model was modified - see Section 4.2.1.

4.2 FREE VIBRATION

The detailed experimental results and associated analysis of the free vibration tests in air are given in Appendix II. Only important results are summarized here.

4.2.1 **Natural Period**

During the free vibration tests in air, the response periods between two successive up-crossings of the deck displacement were found to decrease with increasing vibration cycles (in fact with decreasing response levels) for all models. This variation is primarily attributed to the imperfect deck-leg connections. These connections were different from their original (rigidly clamped) design.

The deck-leg connections of Model I were glued to improve their mechanical behavior (making the clamping more rigid).
The materials used in Model II(-M) were not suited for gluing, even though the imperfection in the deck-leg connection is expected to have a more significant impact on the structure's behavior with this model since its legs and deck beams are smaller than those of Model I - see Appendix II. Consequently, during a free vibration run, different natural periods were obtained for different response cycles - in fact for different response amplitudes just as was the case initially with Model I. These natural periods within one run were averaged over a few cycles to yield the 'representative' period.

Strictly speaking, a natural period for a nonlinear system does not exist and many 'mature' techniques developed for a linear system are not applicable to a nonlinear system. However, the output of commonly encountered slightly nonlinear systems can be seen to be composed of a 'fundamental' linear part plus a nonlinear modification. The techniques normally used for linear systems can be 'borrowed' to approximately treat a nonlinear system in a piece-wise (incremental) form or in an average sense. Using this analogy between linear and slightly nonlinear systems, the response period in free vibration will be called the natural period (the influence of damping on period is of minor importance; even a damping as high as 20% causes only a variation less than 2% in response period) and the virtual lateral stiffness of the structure will be called simply the structural lateral stiffness. This will be discussed further in the following section.

Representative natural periods, T_n , for each of the models obtained from the free vibration tests in air are listed in table 4.2.

Table 4.2 Model Natural Periods

Model No.	Model I		Model II	Model II-M
Natural Period, T_n (sec)	As Built	Glued	As Built	As Built
	1.16	1.02	1.25	1.93

4.2.2 **Inferred Stiffness**

The stiffness of each of the models can be inferred from its dynamic response if it is considered to be a single degree of freedom system. Its global 'dynamic' stiffness, K_d, can be derived from the natural period obtained in the free vibration tests and the model's equivalent mass.
On the other hand, by assuming that the connections ideally represent the original design, the theoretical structural overall stiffness, K_t, can be computed analytically using the construction material properties as given in table 3.1.
Furthermore, the global static stiffnesses of the models, K_s, have been derived in table 4.1 from the static tests.

The stiffnesses of the models obtained from these three approaches are compared in table 4.3; the detailed calculations of K_t and K_d are given in Appendix II.

Table 4.3 Stiffness Comparison

Model No.	K_t (N/m)	K_s (N/m)	K_d (N/m)	
	Theoretical	As Built	As Built	Glued
I	1568.1	508.0	786.57	1017.0
II	82.4	19.9	88.4	--
II-M	65.8	16.8	70.5	--

The inconsistency is apparent. The observed natural period in Section 4.2.1 has already led to distrust of the theoretical design values, K_t. The data in table 4.3 show two tendencies:

1. K_d is systematically larger than K_s ; this is especially evident with models II and II-M. This deviation indicates that the models behave more stiffly in a dynamic situation than in a static situation. This phenomenon is primarily attributable to the connection imperfections (or more specifically, locally concentrated damping). As will be shown in the next section, (especially with Model II and Model II-M) a large amount of damping is (locally) concentrated in the deck-leg connections; relative dynamic movement between the deck and legs generates remarkable resistance. This resistance increases with increasing relative velocities between the deck and legs. Hence, the effect of the high damping in the connections is analogous to a fixation against dynamic loading and thus equivalent to a large 'dynamic stiffness'. When the damping is high enough, the connection will behave dynamically as if it were clamped. As such, the localized high damping at the connections has significant influences not only on the overall structural damping behavior but also on the structural natural period and thus the inferred dynamic stiffness, K_d . However, this fixing mechanism exists only when the structure is experiencing a dynamic movement. If a loading is static, the structure shows appreciably lower stiffness, since only the stiffness of the connection counts then. This stiffness enhancement phenomenon in the dynamic situation has also been discovered in field measurements. The field tests done by Chiba *et al.* (1986) showed that the dynamic stiffness of a jack-up platform can be 2 times its static stiffness.
2. With Models II and II-M the average dynamic stiffness values, K_d , seem quite in agreement with the theoretical ones, K_t . This, however, does not indicate the agreement of these models with their original designs. From the discussion in point 1, above, it is clear that the calculated dynamic stiffness, K_d , generally does not represent the structural (static) stiffness, but an apparent (dynamic) stiffness. In fact, this gives extra supporting evidence for the assumption that the behavior of the deck-leg connection is close to a rigid clamping (the original design) under dynamic loading as a consequence of localized high damping.

4.2.3 **Structural Damping**

The structural damping of the models tested is mainly attributed to the following damping mechanisms:

- Viscous damping
- Dry friction
- Internal material damping
- Plastic deformations

Viscous damping is the only linear damping mechanism; the rest involve a nonlinearity indicated by their dependency upon the response amplitude. Because of the convenience of linear viscous damping in analysis, much effort has been invested (in the literature) in the conversion of other damping mechanisms to 'equivalent' viscous forms by averaging the damping values over several cycles.

The damping values for each of the models are computed in Appendix II. The results are summarized in table 4.4 where r is the structural equivalent damping coefficient, ξ the structural damping ratio, defined as the structural damping coefficient, r, divided by the critical damping coefficient, r_c ($\xi = r/r_c$), and $\hat{A}$ the corresponding deck displacement amplitude.

Table 4.4 Structural Damping Ratio

Model	$\hat{A}$ (cm)	r (kg/s)	ξ (%)
I	2.55	16.14	5.0
	2.15	13.78	4.2
	1.25	12.82	3.8
	1.00	10.46	3.2
	Average	13.37	4.1
II	1.65	5.99	18.8
	1.10	8.54	21.2
	Average	7.27	20.0
II-M	1.6	9.15	25.6
	0.9	12.67	27.8
	0.35	9.61	17.5
	Average	10.48	23.6

The damping values of the Models II and II-M show strong nonlinearity just as with the global stiffnesses; they are heavily dependent upon the structural response level. This dependence relation is, however, rather scattered. In contrast to this, the damping values of Model I are much lower and more consistent; it shows only a relatively slight decrease with decreasing response amplitude levels. This consistency is expected to result from the improved deck-leg connection.

More specifically, the following phenomena can be observed from the above table:

1. The damping ratios are surprisingly large especially for Model II and Model II-M. These values are much larger than the normally found structural internal damping. The only possible source of these high damping percentages is the imperfect connection at both ends. The lower end was linked to the bottom by hinges; this connection is easier to realize than the clamping at the upper end. It is, therefore, considered that the deck-leg connection is most likely the cause responsible for the high structural damping.
2. The average damping coefficient of Model II-M seems slightly higher than that of Model II, although both models are identical except for the deck weight. This deviation can possibly result from extra (dry friction) damping caused by that extra deck weight which was placed on top of the clamping rings - this increased the contact forces between the clamping rings and the deck connecting plates at the upper end as well as the contact forces in the leg bottom hinges at the lower end.

4.3 SUMMARY

The important observations from the discussion of the static and free vibration tests in air are summarized as follows:

1. The behavior of Model I is quite consistent. Gluing improved the connection. The data recorded with this model are reliable.
2. An obvious scatter in the data exists with Model II and Model II-M. The deck-leg connections with these models are found to be different from their original designs and highly complicated. This imperfection in the deck-leg connections results in the

dependency of structural response periods (and thus inferred structural dynamic stiffnesses) as well as structural damping on the response level. The general tendency is that the inferred stiffness decreases with increasing response level; this indicates structural nonlinearities. These connections also cause a surprisingly high structural damping.

3. The apparent dynamic stiffness is substantially larger than the static stiffness with all models.

Chapter 5
Model nonlinearities expected

The analysis of the data from the static and free vibration tests in the previous chapter has shown that the model structures tested are highly nonlinear. The nonlinearities originate from various sources. An inventory of the nonlinearities will provide an overview and shed light for the analysis later in the present work. The evaluation of the relative importance of the influences of various nonlinearities on dynamic behavior will be performed in the following chapters after thorough data analyses and computer simulations have been carried out.

5.1 STRUCTURAL NONLINEARITIES

The models tested mainly include the following two forms of structural nonlinearities:

- Imperfect Connections
  The deck-leg connections especially with Models II and II-M were different from their originally intended (rigid clamping) design and had a complex mechanical behavior. The imperfection of the deck-leg connections resulted in the dependency of structural natural periods (and thus structural apparent stiffnesses) as well as structural damping on the response level. It also causes a high overall structural damping. However, the deck-leg connections of Model I has been glued; this model showed a quite linear structural behavior.

- P-δ Effect
  A second-order moment will be resulted as the deck load becomes eccentric to the vertical reaction forces during horizontal displacements - the so-called P-δ effect. Physically, the P-δ effect decreases the structure's stiffness and increases its response to the hydrodynamic load. It should be noted that when the vertical deck load is constant, the P-δ effect does not introduce extra nonlinearities - the lateral deflection of the structure is linearly related to the lateral loading if the system is otherwise completely linear. The lateral deformation of the structure is, however, nonlinearly related to the vertical load. The resultant normal forces along the legs of the models change with the variation of the overturning

moment. This will cause nonlinearity, although its influence on the overall structural response in the investigated case is expected to be marginal. As such, the P-δ effect now manifest itself mainly as an enhancement of the structural flexibility (Euler amplification). The ratio of the equivalent deck weight to the Euler critical load gives an indication about the degree of the P-δ influence. In fact, this ratio roughly determines the reduction of the structure's stiffness due to the P-δ effect. The P-δ reduction ratios for each of the models have been calculated in Appendix II where they were needed to estimate the models' theoretical stiffnesses. Here, the ratios are summarized in table 5.1. For comparison purpose, an approximate value of the P-δ reduction ratio for a prototype jack-up is listed in the table as well.

Table 5.1 P-δ Stiffness Reduction Ratio

Model No.	I	II	II-M	Prototype
Stiffness reduction due to P-δ effect (%)	8.8	20.7	36.8	10.0

This table clearly shows that the P-δ effect is of importance in the present tests.

5.2 HYDRODYNAMIC NONLINEARITIES

The hydrodynamic nonlinearities stem from the waves themselves and their interactions with the structure. The water-related nonlinearities in the present model tests include the following four primary aspects:

- Wave Kinematics
  According to the analytical criterion of validity given by Dean & LeMehaute (1970), the waves for all three models are best described by the (nonlinear) 2nd Order Stokes Theory. Based upon Chakrabarti's experimental results (1980), however, the Airy Theory is still applicable (for more details, see Appendix III).

- Free Surface Effect

  Obviously, neither the local force in the splash zone nor the total resulting force on the legs at wave crests will be the same as those at troughs. When the contribution to the hydrodynamic load from wave motion above the still water level (*SWL*) up to the instantaneous surface is counted, the total hydrodynamic force on the structure is no longer proportional to the input wave elevation even for otherwise completely linear situations. Another difficulty arising from inclusion of actual wave surface instead of constant *SWL* is the correct prediction of wave kinematics near the free surface zone when the linear wave theory is used. The linear wave theory satisfies the governing wave field equation (the Laplace equation), but it assumes infinitesimal wave height in the free surface boundary. It is, therefore, natural that the predictive capacity of the linear theory is least satisfactory in the trough to crest zone when the infinitesimal wave height assumption is violated. Many techniques have been developed to adjust the kinematics prediction to achieve greater accuracy in this region - further discussion of this is given in Appendix IV.1.

  Since the model legs consist of vertical elements only, any slamming effect is expected to be negligible.

- Quadratic Drag

  Drag, which is quadratically linked to the wave elevation, plays an important role with Models II and II-M, while Model I is fairly inertia-dominated - see Appendix III for more details.

- Relative Motion

  When the structure response is not negligible compared with the absolute water flow motion, the structural motion should be taken into consideration in the hydrodynamic force computation. Note that the relative motion generates nonlinearity only in combination with the nonlinear drag term. The drag force depends quadratically on the resultant velocity in this case; a resulting 10% increase in velocity, for example, increases the drag force by more than 20%. With model I, the typical value of the ratio between the deck displacement and wave elevation - which gives an indication about the ratio of the model leg horizontal motion to the water particle horizontal motion - is around 1.5 with regular wave tests (near resonance) and 1.0 with irregular wave tests (in the root mean square sense). With Models II and II-M this ratio is around 0.3 with regular wave tests (near resonance) and 0.15 with irregular wave tests (in the root

mean square sense). It is, therefore, anticipated that the relative motion will be of more importance for Model I and of less significance for Models II and II-M.

5.3 SUMMARY

The models tested involved both hydrodynamic and structural nonlinearities. The different models have different types of nonlinearities. Roughly speaking, Model I includes a significant relative motion, Model II has a high drag contribution plus a complicated deck-leg connection; with an extra mass on the deck Model II-M demonstrates the influences of the P-δ effect further. This segregation of nonlinearities with different models helps isolate and thus better expose the influences of an individual nonlinearity on the behavior of the structures.

Chapter 6
Regular wave test analysis and computer simulations

6.1 INTRODUCTION

The computational models for the structures tested will be established in this chapter. They will involve discrete elements and computations will be carried out in the time domain. The experimental results from the regular wave tests will also be given here together with the computer simulation results.

6.2 COMPUTATIONAL MODEL

The computational simulation is done using the special purpose program *NOSDA*. The modeling involves two facets:

- Hydrodynamics
- Structural modeling

The special *NOSDA* possibilities important for the description of the above two facets include:

Hydrodynamic interaction options:
- Wave theory choice
- Free surface choice
- Relative or absolute velocity field
- Linearized (Borgman) or quadratic drag

Structural dynamics options:
- *P-δ* element
- Local damping

The discussion in this section is aimed at establishing the most complete computational models for the structures tested. This is checked against laboratory test data in Section 6.3. Some other options or simplifications will be used in Section 6.4 to expose their influences.

The detailed treatments of several nonlinearities together with the P-δ effect are collectively discussed in Appendix IV.

6.2.1 **Hydrodynamics**

Determination of hydrodynamic loading on the structures tested consists of two steps. The first step is the computation of wave kinematics. This describes the motion of the water due to waves. The second step is the calculation of the forces on the model legs, given the water motions. These two aspects are separable here because it is assumed that the presence of the model structures has a negligible effect on the water motions. This assumption is justified by the fact that the model legs are widely spaced and their diameters are less than 1/8 the wave length of interest - in other words, the latter criterion allows a wave frequency of up to 1.5 Hz with Model I and 3.5 Hz with Models II and II-M.
These two steps of hydrodynamic force determination are discussed respectively in the following two subsections.

6.2.1.1 Wave Kinematics

As noted in Section 5.2, the models worked in the area where the waves are best described by the 2nd Order Stokes Theory according to the analytical criterion of validity while the Airy Theory is still applicable based upon Chakrabarti's experimental results. For simplicity, the Airy Linear Wave Theory is chosen to describe flow kinematics for all wave states used; the 2nd Order Stokes Wave Theory will also be employed with some steeper regular wave conditions for comparison. Since the models were tested in intermediate to deep water, the complete form of linear wave theory is used.

The linear Airy Wave Theory describes the water motion only up to the (constant elevation) still water level (*SWL*). Much effort has been made in the offshore industry to modify the linear wave theory to improve the wave kinematic prediction near the free surface where the correct kinematic information is most essential for the offshore structure analysis and discrepancies between different wave theories are also most obvious. Common approaches for computing the water motion kinematics up to the instantaneous actual wave surface include: (1) 'primitive' functional extrapolation represented by application of the Airy wave theory almost exponentially up to the instantaneous wave level; (2) vertical uniform extrapolation which is realized by Airy Wave Theory up to the *SWL* and constant kinematics above the *SWL* - see Steele *et al.* (1988); (3) linear extrapolation which consists of using Airy wave prediction up to the *SWL* then linearly extrapolating the kinematic value of interest using the rate of change of that kinematic quantity with respect to z at the *SWL* as the slope - see Rodenbusch and Forristall (1986); and (4) stretching approach whereby the Airy kinematic profile between seabottom and the *SWL* is stretched to the instantaneous wave surface - see Wheeler (1970) and Chakrabarti (1971). More detailed mathematical formulations for the free surface treatment are to be found in Appendix IV. All four wave kinematic modification options as well as standard Airy Theory are included in *NOSDA*. Note that besides the modification models mentioned above, a great deal of other work has been done in attempt to improve the prediction of the kinematics near the free surface. Among these, Forristall (1981) demonstrates that the Wheeler stretching and the linear extrapolation provides a lower and upper bound respectively for horizontal velocities in the crests of waves. A combination of these two approaches leads to the Delta stretching profile - see Rodenbusch and Forristall (1986). Other schemes proposed for the free surface treatment include Gudmestad model (1990), Gamma extrapolation model - see Borgman *et al.* (1989), and so forth. No single modification model seems universally superior for predicting the kinematics in the crest-trough zone for all wave fields; the accuracy of the prediction of each approximate method depends on the wave conditions - see Zhang, *et al.* (1991). The present test setup was not designed to evaluate these crest-trough kinematic models (the wave kinematics were not recorded.) The waves tested were relatively low. The choice of the crest-trough kinematic model is, therefore, not expected to be vital for the model behavior simulation in the present case.

The Wheeler stretching profile is adopted here as the reference case for the model simulations.

6.2.1.2 Hydrodynamic loads

Wave forces per unit length acting on each leg, based upon the modified Morison Equation (including relative velocities and quadratic drag), are calculated at structural model nodes. These forces are then integrated using linear interpolation between two adjacent nodes.

Since the water particle kinematics and the corresponding hydrodynamic forces per unit length were not recorded during the tests, 'actual' Morison coefficients, C_d and C_m, cannot be derived. The best solution, then, is to extract these values from other tests dedicated to the determination of the hydrodynamic coefficients under similar conditions and reported in the literature. In the present tests, the Reynolds number ($Re = \hat{u}D/\nu$, where $\hat{u}$ is the amplitude of the water particle velocity at the *SWL*, D the outer diameter of the leg and ν the fluid viscosity) ranges from $4 \cdot 10^3$ to $2 \cdot 10^4$ with Model I, $1 \cdot 10^3$ to $7 \cdot 10^3$ with Model II and $1 \cdot 10^3$ to $3 \cdot 10^3$ with Model II-M. These Reynolds number ranges are rather low; little experimental data are available. The closest test series so far found are those by Chakrabarti (1982) which were carried out in a wave tank with *Re* varying from $2 \cdot 10^4$ to $3 \cdot 10^4$. His results, therefore, are used as a basis for later hydrodynamic coefficient determination.

6.2.2 **Structural Model Establishment**

The model subjected to time-dependent hydrodynamic loads is discretized both spatially and temporally to perform a numerical structural dynamic analysis.
A multiple-degree-of-freedom Discrete Element Method (*DEM*) is used to discretize the structure in space. The *DEM* schematizes the physical object as if it were composed of a finite number of discrete, undeformable elements interconnected by massless, deformable springs and dampers. The degrees of freedom (*DOF*s) are defined at the interconnections (the nodes). Lumped masses (or, more generally inertias) correspond with the *DOF*s of the model.
The *DEM* schematization results in a group of (differential) equations of motion. These equations are solved in *NOSDA* using a direct time integration - the Kok-γ method. The direct integration, in fact, discretizes the equations in time and turns them into a set of algebraic equations. The responses are then obtained through matrix manipulations.

6.2.2.1 Initial Structural Computational Models

The initial computational model for each of the structures tested is established using the building blocks available in *NOSDA* which are described in Appendix V. The structure stiffness is modeled by springs and the inertia by lumped mass elements. The *P-δ* effect is included as a negative extension spring linking two nodes of an element in the horizontal direction; the details about this type of special spring are given in Appendix IV.4. The rotational spring and dashpot can be considered to be a pair of extension springs and dampers, respectively. An example of such nodes is illustrated in figure 6.1.

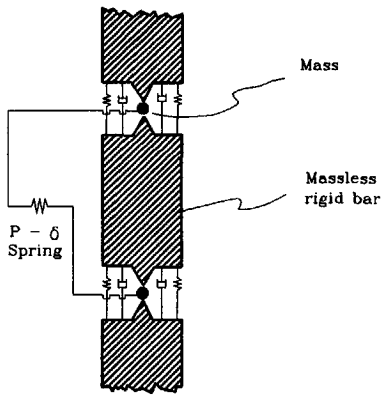

Figure 6.1 Nodes, Elements, Springs and Dampers in a Leg Section

More general descriptions about structural schematization will be given in Section 6.2.2.4 after the complete structural computational models are established.

All the internal damping coefficients along the legs as well as spring and damping coefficients at the upper and lower ends of the legs remain undetermined in these initial models. It is already known from the experimental data processing in Chapter 4 that the physical models more or less deviated from their original design. Some major differences were evident in the connections especially with Models II and II-M. These deviations introduce a stiffness and damping uncertainty at the connections at both ends of each leg.

Additionally, the internal structural damping values along the legs and even the overall internal structural damping ratio are also unknown, although they are expected to be small and not to play an important role in the response analysis.

6.2.2.2 Discretization in Time

The *DEM* spatial discretization yields a set of ordinary differential equations of motion. In *NOSDA* these equations are solved numerically using the Kok - γ direct integration method in the time domain - see Blaauwendraad and Kok (1987). In the actual computation, the integration parameter γ is chosen to be zero - see Liu and Massie (1988). The system then works using a constant displacement field and works identically to the Newmark - β method. This numerical method is unconditionally stable for a linear system. For the present nonlinear case, the stability is not automatically assured; its assumption is commonly considered to be reasonable, however. Luckily, divergence of an unstable simulation is usually quite obvious.

6.2.2.3 Calibration Using Experimental Data

The unknown damping coefficients along the legs as well as spring coefficients at the upper and lower connections in the initial models will be determined using the information obtained from the free vibration tests in the air.

Since the free vibration data recorded are generally overall structural responses, they do not shed much light on the detailed damping distribution within the structures. Instead, the decays of the free vibration responses give an indication of the overall damping for each structure. The detailed choice of the damper locations and the relative magnitude of the damping coefficients is somewhat subjective. The internal damping ratio (commonly not larger than 1%) can be converted to the internal damping element coefficients in the computational model using the procedure given in Liu (1989). Unfortunately, even this internal damping ratio is unknown for the model materials used. Nevertheless, it has already been assumed that the actual structural damping was largely concentrated at the deck-leg connection; the internal structural damping and leg bottom

damping only play a minor role; this relative proportion is qualitatively taken into consideration in the structural modeling.

The general approach of model calibration is to fit the simulated free vibration response traces to the measured ones by adjusting the model damping coefficients and the connection stiffness parameters. This is a 'try and correct' iteration process and will be done for each of the models until the natural period and decay of the simulated response match those of the measured response.

It has already been established from the analysis in Chapters 4 and 5 that in terms of structural behavior Model I is reasonably linear, while Models II and II-M show remarkable nonlinearity. It is straightforward to use simple linear rotational springs and dashpots to model the upper connection for Model I. As for Models II and II-M, it will be more scientifically reliable if realistic nonlinear (elasto-plastic) springs and dash-pots are used to model the deck-leg connections. However, since very little is known about the detailed mechanical properties of the connections for these two models, the choice of the nonlinear springs and dampers will be too subjective. Any attempt to 'speculate' connection nonlinearity is considered inappropriate here. Each of the three models is modeled, therefore, using mass, linear spring and linear damping elements with an extra group of P-δ elements.

It should be noted that the damping and stiffness are interrelated if plasticity occurs. If realistic elasto-plastic springs were used, hysteretic damping would be simulated under cyclic loadings.

The detailed damping and connection stiffness distribution so determined is somewhat arbitrary. For instance, two (and more) different sets of computational model coefficients for Model II could result from the calibration as shown in figure 6.2.
The deck-leg connection with data set 1 in figure 6.2 consists of soft springs with low stiffness and hard dampers, while in set 2 the connection springs have appreciably higher coefficients (twice the field spring coefficient value - see Appendices V.2 and V.3, in fact, this is the ideal clamping situation) and the dampers have lower coefficients. These two data sets differ only in the deck-leg connection elements (as listed in the table on the left side of the figure). The rest of the elements are identical. (For brevity their coefficients are not shown in the figure.) Both models generate almost identical free vibration

response in terms of the decay and natural period; the only perceivable difference is that the free vibration response trace resulting from set 1 shows somewhat more asymmetry with respect to the time axis. This asymmetry was also observed in some of the measured response traces, by the way. As will be shown later, these models also result in almost the same dynamic response under wave loads. It is interesting to note the fact that these two models have quite different static stiffnesses, while their apparent dynamic stiffnesses derived from the free vibration simulation are the same. The numerical results are given in table 6.1.

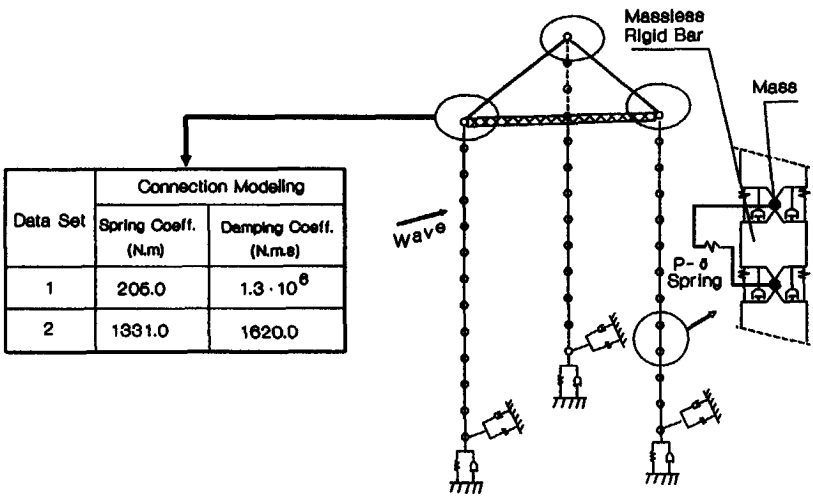

Data Set	Connection Modeling	
	Spring Coeff. (N.m)	Damping Coeff. (N.m.s)
1	206.0	$1.3 \cdot 10^6$
2	1331.0	1620.0

Figure 6.2 Two Computational Models (Model II)

Table 6.1 shows that data set 1 yields a static stiffness much closer to the measured value. Hence, this modeling set is used for the later simulation.

Table 6.1 Two Sets of Modeling for Model II

Data set	Deck Connection Modeling	Static Stiffness (N/m)	Dynamic Stiffness (N/m)
1	High Damping	38.0	88.4
2	High Stiffness	79.6	88.4

It should be noted that the phenomenon that the static stiffnesses are much lower than those derived from vibration tests has also been discovered in field measurements at several locations and with different jack-up platforms. The work done by Chiba *et al.* (1986) showed that the dynamic stiffness of a jack-up platform can be 2 times its static stiffness. Those authors attributed this discrepancy to the soil interaction. It seems reasonable from the analysis in this section that the stiffness enhancement in the dynamic situation could be also attributable, at least partially, to the trade-off of local deck-to-leg damping and stiffness.

6.2.2.4 Structural Computational Models (in air)

The computational model for each structure is completed using the calibration procedure above. Note that the schematizations established so far are 'dry models'; their mass elements will be modified to include water inertia effect when simulating structural response in waves.

The 'dry' schematization for Model I is given in figure 6.3 and the associated lumped masses, spring coefficients and damping coefficients are listed in table 6.2. Each leg of Model I is discretized into 11 massless rigid elements connecting 12 nodes. Each of the nodes includes a rotational spring, a rotational dashpot and a mass. Since both the structure and flow are symmetric, the system is modeled one-dimensionally in the x direction. The *DOF*s correspond to the nodes indicated as arrows in the figure. The highest two elements of each leg are slightly longer than the rest of elements, so the associated stiffness coefficients of the rotational springs are slightly lower. Additionally,

a negative spring is placed between two nodes of each element to represent the P-δ effect. The contribution of the leg weight to the P-δ effect is included by summing all node weights above the investigated segment. As a result of this, the coefficients of the P-δ spring decrease (become more negative) downwards along a leg. It should be noted that the coefficients of these springs are so determined that they only account for the P-δ effect due to the structure gravity; the additional dynamic axial load along the legs induced by the wave forces are not included. Since the attention in this work is concentrated on the global (deck) displacement, this negligence can be justified by the fact that the stiffness lost in the leeward leg(s) are approximately compensated by the extra stiffness gained in the windward leg(s). Inclusion of the effect of the axial load variation would cause the P-δ spring coefficients dependent on the instantaneous leg axial load; this would introduce a nonlinearity and subsequently increase computational effort.

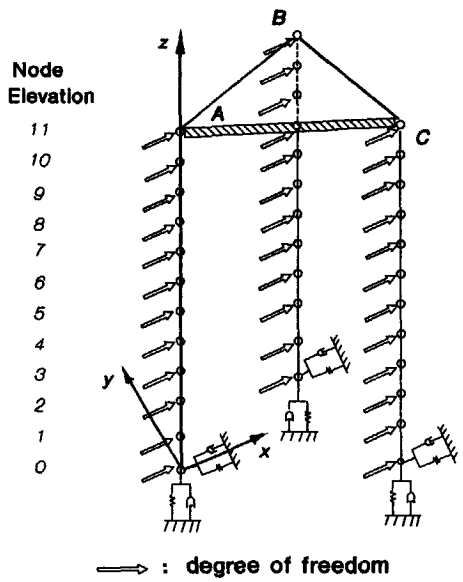

Figure 6.3 Schematization for Model I in Air

Table 6.2 Schematization Parameters for Model I in Air

Node Elevation	Mass (kg)		Spring Coeff. (N.m)	Damping (N.s/m)	P – δ Spring (N/m)	
	Leg A	Legs B, C	Legs A, B, C	Legs A, B, C	Leg A	Legs B, C
0	1.282	1.282	0.0	29.0	–488.9	–493.1
1	0.227	0.227	10590.0	10.0	–478.8	–482.9
2	0.207	0.207	10590.0	10.0	–468.6	–472.8
3	0.207	0.207	10590.0	10.0	–458.5	–462.6
4	0.207	0.207	10590.0	10.0	–448.3	–452.5
5	0.207	0.207	10590.0	10.0	–438.2	–442.3
6	0.207	0.207	10590.0	10.0	–428.0	–432.2
7	0.207	0.207	10590.0	10.0	–417.9	–422.0
8	0.207	0.207	10590.0	10.0	–407.7	–411.9
9	0.218	0.207	10085.7	10.0	–360.9	–364.7
10	0.228	0.228	9627.3	10.0	–350.7	–354.5
11	7.951	7.866	4550.0	120.0		
Foot Restraint	Spring (N/m)			Damping (N.s/m)		
	$7.0\ 10^7$			100.0		

Assuming a relatively high damping at the deck-leg connection, the parameter set 1 in figure 6.2 is used for Model II. The computational schematization is quite similar to that of Model I, except one more leg element is used here in order to maintain a convenient element length (Model II has a slightly different total leg length from Model I). The computational schematization for Model II is shown in figure 6.4 and the associated parameters are listed in table 6.3. Just as with Model I, the schematization for Model II is also one dimensional. For simplicity, the *DOF*s are not indicated in the figure.

The schematization for Model II-M is almost identical to that for Model II. Higher deck weight requires an adjustment of the *P-δ* springs as well as the mass elements at the deck corners. The damping level is slightly higher; this can be attributed to extra connection friction at the upper and lower ends - see Section 4.2.3. The schematization parameters are given in table 6.4.

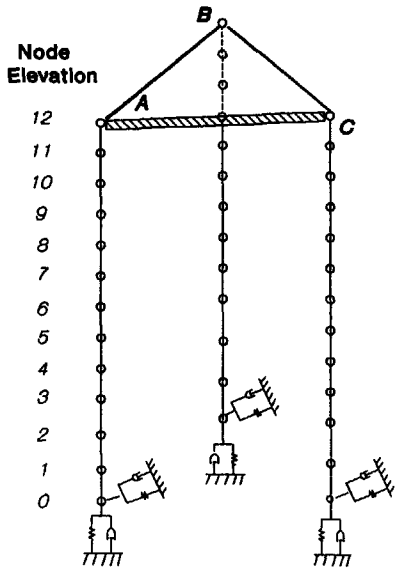

Figure 6.4 Schematization for Model II in Air

Table 6.3 Schematization Parameters for Model II in Air

Node Elevation	Mass (kg)		Spring Coeff. (N.m)	Damping (N.s/m)	P – δ Spring (N/m)	
	Leg A	Legs B, C	Legs A, B, C	Legs A, B, C	Leg A	Legs B, C
0	0.524	0.524	0.0	38.7	–82.7	–86.7
1	0.078	0.078	715.6	170.0	–78.1	–82.6
2	0.078	0.078	715.6	170.0	–74.0	–78.5
3	0.078	0.078	715.6	170.0	–69.9	–74.4
4	0.078	0.078	715.6	170.0	–65.8	–70.3
5	0.078	0.078	715.6	170.0	–61.7	–66.1
6	0.078	0.078	715.6	170.0	–57.5	–62.0
7	0.078	0.078	715.6	170.0	–53.4	–57.9
8	0.078	0.078	715.6	170.0	–49.3	–53.8
9	0.078	0.078	715.6	170.0	–45.2	–49.7
10	0.081	0.081	689.6	170.0	–38.0	–42.2
11	0.084	0.084	665.5	170.0	–34.0	–38.1
12	0.692	0.777	205.0	$1.3\ 10^6$		
Foot Restraint	Spring (N/m)			Damping (N.s/m)		
	$5.0\ 10^4$			100.0		

Table 6.4 Schematization Parameters for Model II-M in Air

Node Elevation	Mass (kg)		Spring Coeff. (N.m)	Damping (N.s/m)	P – δ Spring (N/m)	
	Leg A	Legs B, C	Legs A, B, C	Legs A, B, C	Leg A	Legs B, C
0	0.524	0.524	0.0	67.0	-136.4	-142.1
1	0.078	0.078	715.6	170.0	-132.3	-138.0
2	0.078	0.078	715.6	170.0	-128.2	-133.9
3	0.078	0.078	715.6	170.0	-124.1	-129.7
4	0.078	0.078	715.6	170.0	-120.0	-125.6
5	0.078	0.078	715.6	170.0	-115.8	-121.5
6	0.078	0.078	715.6	170.0	-111.7	-117.4
7	0.078	0.078	715.6	170.0	-107.6	-113.3
8	0.078	0.078	715.6	170.0	-103.5	-109.2
9	0.078	0.078	715.6	170.0	-99.4	-105.1
10	0.081	0.081	689.6	170.0	-89.6	-93.7
11	0.084	0.084	665.5	170.0	-85.4	-90.0
12	1.742	1.827	205.0	$9.8\ 10^6$		
Foot Restraint	Spring (N/m)			Damping (N.s/m)		
	$5.0\ 10^4$			100.0		

6.3 MEASURED VERSUS SIMULATED RESULTS

The hydrodynamic coefficients, C_d and C_m , are selected after considering the expected relative movement of the model with respect to the water using Chakrabarti's (1982) experimental results.

Model I was tested at low Keulegan-Carpenter Number ($KC = \hat{u}T/D$, where $\hat{u}$ is the amplitude of the water particle velocity at the *SWL*, T the wave period and D the outer diameter of the leg; this parameter indicates the ratio of the water particle orbit diameter to the structure diameter and provides a measure of the relative importance of the drag force) with a small KC variation range ($KC = 0.7 \rightarrow 2.1$). From Chakrabarti's results, the C_m value should be somewhere around 2.3 and C_d should be 0.5. However, these hydrodynamic coefficients were determined for a fixed cylinder. With Model I, the structural response is significant compared with the water motion (the ratio of the deck displacement to wave elevation reaches 2.2 near resonance); the influence of the relative motion on the hydrodynamic coefficients should be taken into consideration. The flexible cylinder tests by Delft Hydraulics at De Voorst show that structure motion can significantly increase C_d and correspondingly decrease C_m values - see Bearman (1988). The C_d values and C_m values actually used in the simulation for all wave states with Model I have (somewhat arbitrarily) been chosen to be 0.8 and 1.8 respectively.

The *KC* Numbers with Models II and II-M vary appreciably from one wave condition to another. The *KC* values range from 8.0 to 24.0 with Model II and from 8.0 to 25.0 with Model II-M. The C_m and C_d values are extracted from Chakrabarti's results for each wave state tested (the influence of relative motion on the hydrodynamic coefficients are considered of minor importance with these tests).

Knowing the C_m value, the computational model for Model I established in Section 6.2 is further modified to account for the water 'added mass' (about one third of the total equivalent mass). In the modeling, this distributed mass is lumped to the corresponding nodes and added to the nodal structure mass; this modifies the existing dry model given in figure 6.3 and table 6.2 to a new 'wet' computation model. The schematization remains basically the same, only the masses of the submerged nodes need to be changed. The new parameter set is listed in table 6.5 where the modified node masses are indicated by italic letters. These data will be used to simulate the dynamic response of Model I in waves.

Table 6.5 Schematization Parameters for Model I in Water

Node Elevation	Mass (kg)		Spring Coeff. (N.m)	Damping (N.s/m)	P – δ Spring (N/m)	
	Leg A	Legs B, C	Legs A, B, C	Legs A, B, C	Leg A	Legs B, C
0	*1.791*	*1.791*	0.0	29.0	–488.9	–493.1
1	*1.245*	*1.245*	10590.0	10.0	–478.8	–482.9
2	*1.225*	*1.225*	10590.0	10.0	–468.6	–472.8
3	*1.225*	*1.225*	10590.0	10.0	–458.5	–462.6
4	*1.225*	*1.225*	10590.0	10.0	–448.3	–452.5
5	*1.225*	*1.225*	10590.0	10.0	–438.2	–442.3
6	*1.225*	*1.225*	10590.0	10.0	–428.0	–432.2
7	*1.225*	*1.225*	10590.0	10.0	–417.9	–422.0
8	*1.225*	*1.225*	10590.0	10.0	–407.7	–411.9
9	*0.422*	*0.422*	10085.7	10.0	–360.9	–364.7
10	0.228	0.228	9627.3	10.0	–350.7	–354.5
11	7.951	7.866	4550.0	120.0		
Foot Restraint	Spring (N/m)			Damping (N.s/m)		
	$7.0\ 10^7$			100.0		

In contrast to the case of Model I, the water 'added mass' plays only a minor role for the remaining two models (especially for Model II-M); it is now one order lower than the equivalent dry structural mass. The hydrodynamic mass is, therefore, neglected; the dry models given in tables 6.3 and 6.4 will be used as wet models for Model II and Model II-M, respectively.

Various *NOSDA* options are used in the complete model simulations. The water kinematics are calculated using linear Airy Theory. The modified Morison Equation (including relative velocities and quadratic drag) is employed to compute hydrodynamic forces. The stretched wave profile is adopted to include the free surface effect. Leg shear and axial flexibilities are considered unimportant for the overall dynamic response on which the main attention in the present simulation is concentrated and thus ignored.

Numerical aspects associated with the simulations are carefully evaluated in Appendix VI. In the actual computation, the iteration error tolerance is set to be 10^{-7} m (compared with the magnitude of the model response at deck level of the order of 10^{-3} to 10^{-2} m). The integration time step, Δt , is chosen to be 0.03 s to guarantee the numerical convergence for all waves and a local truncation error - $O(\Delta t^4) = 10^{-7}$. The number of vibration cycles needed for filtering out the transient response depends heavily on the system damping level. With the damping data listed in table 4.4, the number of cycles for the response amplitude to decay to 1% of its initial value is about 18 for Model I and 4 for model II(-M). Since the present study concerns the structural steady state response, the transient response is excluded from the bookkeeping.

Inclusion of the free surface effect, as discussed in Appendix IV, introduces skewness to the total hydrodynamic forces and therefore shifts the response trace from the standard sinusoidal shape. In the following simulations, the maximum magnitudes of the responses are taken as the steady state peak responses.

Most of the results in this work are presented via Response-Amplitude-Operator (RAO) curves. A RAO curve for the deck displacement with regular waves is constructed here as follows: let a series of monochromatic wave trains, with the same wave height but each with a different wave frequency pass the structure individually; normalize the obtained amplitude of the response displacement at deck level by half the input wave height; plot this ratio for each wave frequency input of interest. The correct determination of the deck displacement is vital in the offshore structural design and assessment; the present work will concentrate mainly on this overall response parameter. For brevity, the RAO curve for the deck displacement is often called simply 'RAO curve' in the following text. This type of curve is a very general indication of structural response behavior. From an analysis point of view it includes three major transformation stages: wave surface elevation → water particle kinematics → hydrodynamic loads → overall structure response. Nonlinearity at any transformation stage will cause the resulting curve to be dependent upon the input level. In other words, unlike a structural resonance function in the usual linear sense (invariant with the input level at a frequency), RAO curves for a system which is nonlinear (either hydrodynamically or

structurally) for varying inputs are no longer identical. This is an indicator of system nonlinearity.

The RAO curves of Model I for three different wave heights are superimposed in figure 6.5.

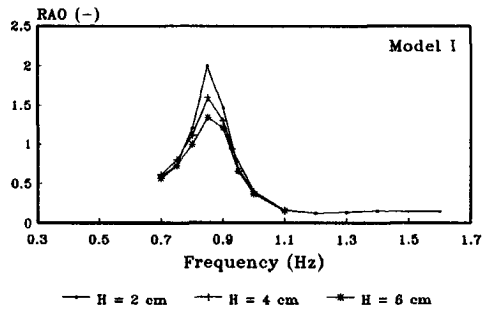

Figure 6.5 Measured RAOs for Deck Displacement with Different Wave Heights (Model I, Regular Waves)

This figure shows that higher waves result in lower RAO values. The system thus shows a definite nonlinearity. The deviation is especially obvious in the resonant area; this leads to a hypothesis that the variation is mainly caused by the different hydrodynamic damping level for different wave heights with this model. It is known that the hydrodynamic damping is generated by the structural response (a fixed structure has, obviously, no hydrodynamic damping.) This implies a need to use relative velocity in the computational model.

The RAO curves of Model II for various wave heights are compared in figure 6.6.

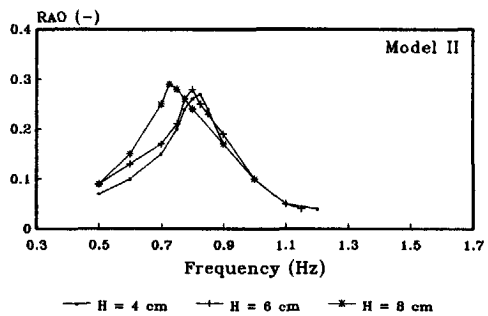

Figure 6.6 Measured RAOs for Deck Displacement with Different Wave Heights (Model II, Regular Waves)

Again, the RAO magnitude shows a definite dependency on the input wave heights. The trend is, however, just opposite to that with Model I - the RAOs now increase with increasing wave height and the RAO peaks shift to the left with increasing wave heights. This dependency is probably caused by other types of nonlinearities. There are at least two contributing effects in this case: (1) the structure's stiffness decreases with increasing loading level and (2) the drag term (which increases quadratically with increasing wave height) plays a more dominant role in the hydrodynamic interaction.

The RAO curves for three different wave heights have been calculated using the complete computational model for each structure tested. Comparisons with the corresponding measured data show a reasonable agreement. Only a representative part of such comparisons (with a 6 cm wave height) is included here; each of figures 6.7 through 6.9 is for a different model. The detailed analyses and results have been reported by Liu (1989).

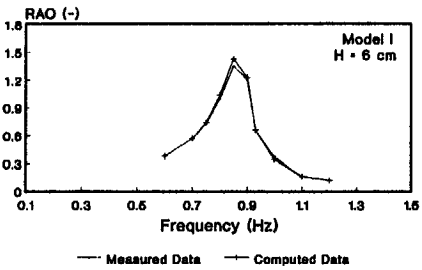

Figure 6.7 Measured and Computed RAOs (Model I, Regular Waves)

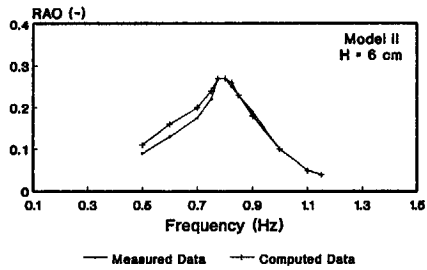

Figure 6.8 Measured and Computed RAOs (Model II, Regular Waves)

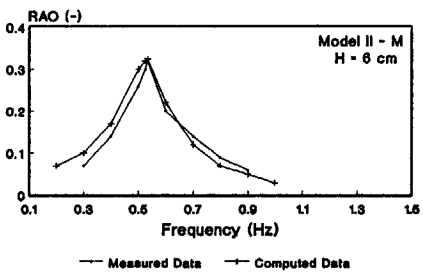

Figure 6.9 Measured and Computed RAOs (Model II-M, Regular Waves)

These results demonstrate that the behavior of Model I is best represented by the computational model. The discrepancy between the computed results and measured results with the last two models is expectable: their behavior is more nonlinear - both structurally and hydrodynamically - and thus more complicated. But still, the simulated results are quite acceptable.

6.4 COMPUTATIONAL EFFORT

The computational effort needed to simulate the dynamic behavior of a model generally depends upon the following factors:

- Model size and complexity
- Incident wave frequency components
- Nonlinearity

When only the steady state response with regular wave simulations is of interest, the overall damping level of the structure also influences the total computing time. Obviously, for different input wave frequencies and different structures, the simulation durations are quite different. It is, therefore, difficult to give a general evaluation of the computation efforts. Nevertheless, experience with computations for this study can give some indication of the computing time involved. A more detailed evaluation of the computation efficiency is given in Appendix VII. With the present regular wave simulation, for an excitation period near the structural fundamental natural period (around 1.2 s), using a time step of 0.03 s (40 time steps per cycle), the DECstation 3100 Computer needs about 39 s of CPU time to simulate a clock time duration of 40 s; this gives a rough indication of the computational efficiency. The ratio between the simulation time and the physical time is an efficiency of about 1:1.

6.5 FURTHER COMPUTATIONAL RESULTS

Certain simulations are carried out further to 'zoom in' on some particular modeling features.

6.5.1 **Absolute versus Relative Velocities**

The absolute velocity approach is found to over-estimate the resulting peak response by up to 50% near resonance. The need to use the relative velocity model is also demonstrated by comparing the relative positions of RAO curves for different wave heights. With Model I, unlike measured results given in figure 6.10 (extracted from figure 6.5 by cutting off the higher frequencies in order to concentrate on the resonant area), the RAO curves computed for different wave heights using absolute velocities shown in figure 6.11 are almost identical.

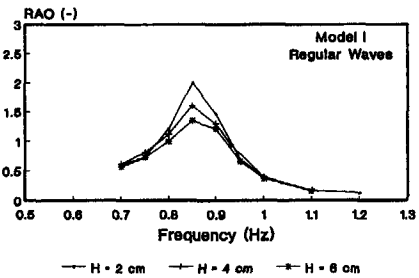

Figure 6.10 Measured RAOs for Various Wave Heights (Model I, Regular waves)

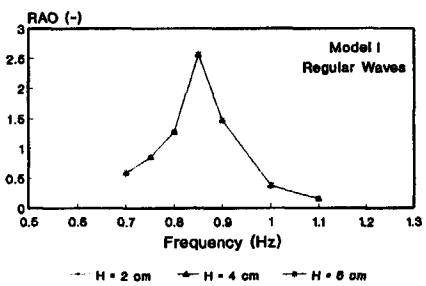

Figure 6.11 Use of Absolute Velocity Model for Various Wave Heights

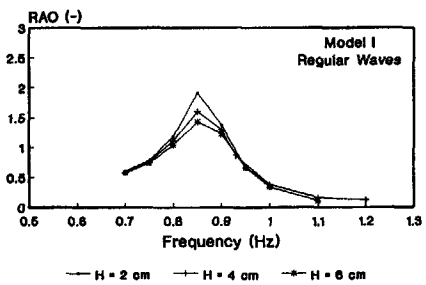

Figure 6.12 Use of Relative Velocity Model for Various Wave Heights

In contrast to this, the relative velocity model properly simulates the variations of the RAO curves near the resonance - see figure 6.12. This indicates that the drag term combined with relative velocity behaves somewhat like a hydrodynamic damper in a large inertia situation; a higher wave causes a lower peak at the RAO curve. When dealing with a fixed cylinder in the inertia dominant range, it is commonly assumed that the drag term plays only a minor role and that therefore the choice of C_d is not important. This is, however, not true with a flexible structure because the drag coefficient and relative velocities now will determine the hydrodynamic damping level in the simulation. Therefore, a correct choice of C_d is essential for the success of such simulations of flexible structures even in the inertia dominant situations ($0.7 < KC < 2.1$ as with Model I).

Neglecting the effect of structural velocity will eliminate the hydrodynamic damping. When using an absolute velocity model, this damping is often compensated by adding an 'artificial' equivalent damping to the structural damping. However, the choice of this damping is somewhat subjective. Further, it should be noted that this damping is dependent upon the input wave and structural response level. Generally speaking, a higher wave will cause a higher level of hydrodynamic damping. Use of relative velocities avoids the associated guesswork at the cost of a greater computational effort.

6.5.2 **Results of Linearized Model**

The simulation using a linearized model is carried out by choosing the following *NOSDA* options: absolute velocity, Borgman-type drag term linearization and exclusion of the free surface effect. It should be noted that using Borgman linearization with regular waves is not a common practice; this is done here only for comparison purpose. In fact, a regular wave can be considered as a special case of irregular waves. The results show that the linearization overestimates the response by about 61% with Model I (inertia type) and about 70% with Model II (drag type) near resonance.

Note that various nonlinear effects - neglected in the linearized approach - can have compensating influences. For example, there are two factors increasing the response: 1. using absolute velocity rules out the hydrodynamic damping; and 2. the Borgman Linearization applied to monochromatic waves overestimates the drag force peak by about 12.8% - see Liu (1989). On the other hand, leaving out the free surface effect underestimates the total hydrodynamic exciting force to some extent.

6.5.3 **Free Surface Effects**

Five types of common mathematical treatments of the free surface effect are available in the *NOSDA* software, namely, (1) standard Airy profile (integrated up to the still water level, *SWL*), (2) functional extrapolation profile (exponentially extended to the actual water surface), (3) vertical uniform profile (the kinematics being kept equal to those at the *SWL* up to the wave crest), (4) linear extrapolation profile (linearly extended to the instantaneous water surface) and (5) Wheeler stretching profile (the kinematics at the instantaneous free surface are considered identical to those originally calculated for the *SWL*) - see Appendix IV for more details. With the present (low) waves, the difference in the results computed using different free surface treatments is found to be negligible.

6.5.4 **Hydrodynamic Cancellation**

With the present model setup and incident wave direction, a simplified theoretical analysis given by Liu (1989) shows that when a wave length is twice as long as the distance between the bow leg and the aft leg plane, the total hydrodynamic force on the three model legs is minimum and equal to one third of what it would be if the forces on all legs were in phase; this results in a cancellation frequency of roughly 1.15 Hz. On the other hand, with both the measured and computed RAO curves as shown in figure 6.13, a slight 'dent' is found in the neighborhood of 1.2 Hz. This dent is more obvious in tabulated data; this confirms the theoretical prediction.

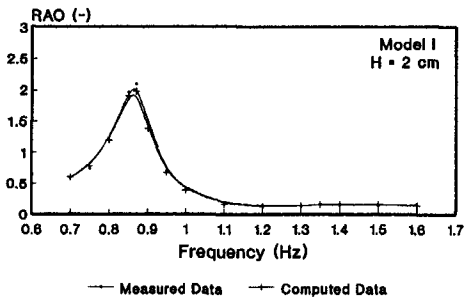

Figure 6.13 Measured and Computed RAOs (Model I, Regular Waves)

Theoretical (numerical) studies also show that when the incident wave direction coincides with the line connecting two legs (30 degrees for the present case), the true cancellation (sum of the wave forces on three legs remains zero during the entire wave period) can be predicted at certain input wave lengths (1.5 times the leg spacing, for example) using the linearized drag term and excluding the structure response and the free surface effect; when the quadratic drag term is used there is only 'quasi' cancellation in which the sum of the force is minimum but not zero - see Spaargaren (1989).

6.5.5 **Airy versus Stokes 2nd Order Wave Theories**

According to the analytic criterion of wave theory validity given by Dean (1968), all three models work in the hydrodynamic area where Stokes' 2nd Order Theory is the most suitable for the wave description; the Airy Theory is still applicable based upon Chakrabarti's experimental results, however. For validation purposes, the Stokes' 2nd Order Theory is used with Model II for a somewhat higher wave tested in the lab and the results are compared with measurements and those obtained using the Airy Theory. It is found that with the present waves, use of these two wave theories makes negligible difference in terms of the resulting structural response.

6.5.6 **Results of Different Connection Modeling**

Two sets of computational models for Model II have been presented in figure 6.1: one simplifying the deck-leg connection as a heavy damper combined with a soft spring (set 1), and another as a hard spring with a light damper (set 2). The RAO curves computed using these two models are compared in figure 6.14. The results generated by these different computational models are almost identical till very low frequencies. It seems that more than one schematization can simulate the dynamic behavior of a physical model if only the overall dynamic response is examined.
This result also confirms the hypothesis that localized (large) damping can function like a stiff spring (or even rigid connection) in a dynamic situation. Actually, the phenomenon that static stiffnesses can be much lower than those derived from vibration tests has also been discovered in field measurements at several locations and with different jack-up platforms. This has already been discussed in Section 6.2.2.3.

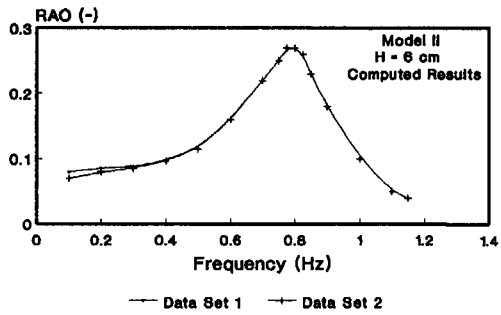

Figure 6.14 Comparison of Different Connecting Modeling

6.5.7 *P-δ* Effect

A RAO curve for Model I simulated without the *P-δ* effect is compared with the corresponding results including this effect in figure 6.15.

This figure shows that the effect of including *P-δ* is two-fold:

a. Firstly, it decreased the system stiffness and hence decreases the natural frequency of the system. It can be seen from the figure that the peak of the RAO curve shifts to the left when the *P-δ* effect is included.

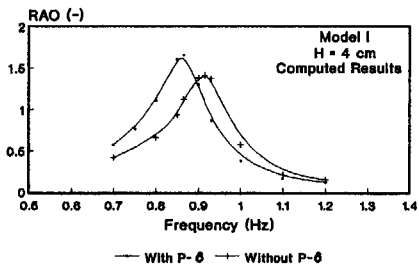

Figure 6.15 Influence of P-δ Effect

b. Secondly, an increase of peak structural response accompanies the reduction in stiffness. Note that in spite of the structural linearity of Model I, this peak value increment is not proportional to the reduction of the global stiffness, since a RAO curve includes more than the structural dynamic amplification. For example, the transformation from the wave surface elevation to the water particle kinematics is

frequency dependent; in the higher frequencies (say, $f > 0.5$ Hz for the present case, approximately), with waves of the same height, the wave velocities decrease linearly and the wave accelerations decrease quadratically with decreasing wave frequencies. The Morison Equation transformation strengthens this trend further. On the other hand, the cancellation effect of total hydrodynamic force would, in the investigated frequency range, raise the peak.

6.6 SUMMARY

The regular wave test results have been presented and analyzed in this chapter. Simulations have been carried out using the computational models established with the *NOSDA* software. The work in this chapter can be summarized as follows:

1. The physical models tested in regular waves show a definite nonlinearity. With Model I higher waves cause lower RAO values as a result of hydrodynamic damping generated by relative motion. In contrast to this, the trend of RAO variations with Models II and II-M is to increase with increasing input level; this dependency is attributable mainly to two factors: (1) the structure's stiffness decreases with increasing loading level and (2) the drag excitation increases quadratically with increasing wave heights.
2. The results from the *NOSDA* simulations which include the P-δ effect and hydrodynamic nonlinearities are generally in agreement with the measured data. This justifies the computational models used.
3. The computational intensity for use of *NOSDA* is acceptable; the ratio between the computer time and the physical time is about 1:1 with regular wave simulations using a DECstation 3100 computer.
4. Relative velocity, instead of absolute water particle velocity, is required for simulating the behavior of a compliant structure. This allows the straightforward modeling of hydrodynamic damping. Near resonance this (extra) damping level is important even though the contribution of the structural velocity to the computation of the hydrodynamic force might otherwise be of minor importance. Drag, when combined with significant structural response, then remains important, even at low *KC* Number conditions.
5. Using Airy Wave Theory or Stokes' 2nd Order Wave Theory makes negligible difference for the (low wave) cases investigated.

6. Discrepancies between the stiffness obtained from static tests and that derived from dynamic vibration tests have been observed both in the field (by others) and in the present lab models. Connection damping and stiffness at the deck-leg connection can - within certain limits - be 'traded off'. Numerical investigation using *NOSDA* shows that identical dynamic lateral deflection at deck level can be obtained over a wide range of frequencies from models which differ only in the damping and stiffness values at the deck-leg connection. Such models have quite different static properties. Since the degree of the stiffening phenomenon is structure and sea-state dependent, this trade-off of damping and stiffness will need considerable additional study.
7. A unique dynamic model of a jack-up rig cannot be determined by calibration with lateral deck deflection alone. This must be augmented by precise knowledge of deck-leg connection and spudcan behavior. An alternative for an existing platform is to calibrate the model against recorded internal loadings in the top and bottom connections as well.
8. Inclusion of the P-δ effect is essential for the success of jack-up simulations. This effect can be well simulated using a group of special P-δ elements (negative springs).

Chapter 7
Irregular wave test analysis and computer simulations

7.1 INTRODUCTION

The analysis of the data obtained from the static tests and regular wave tests in the previous chapters has shown that the model structures are rather nonlinear. The nonlinearities originate from two sources: (1) Structural - mainly caused by imperfect deck to leg connection; and (2) Hydrodynamic - including wave kinematics, free surface effects and relative motion between waves and structure acting with quadratic drag. With the relatively low waves used in the regular wave tests, the nonlinearities caused by free surface effects and wave kinematics have proven to be of minor importance (Chapter 6); this statement is expected to be valid for the irregular wave tests as well, since their hydrodynamic characteristics are quite similar to those of the regular wave tests - see Appendix III for details. As such, the models tested can be categorized into two types according to their nonlinear properties:

a. Relative motion type: Model I belongs to this category. With this model, the structural displacement and water particle motion are of the same order of magnitude and relative motion is, therefore, obviously of importance, while its structural and hydrodynamic behavior is otherwise predominantly linear.

b. Drag and nonlinear structure type: Model II and II-M fall into this category; their deck-leg connections have a complicated nonlinear behavior and their hydrodynamic forces includes an important contribution from drag (due to slenderness of their legs), while relative motion only plays a minor role (the structural response is roughly one order of magnitude lower than the water particle displacement).

The random data from these two types of model tests will be analyzed using the *RANDA* software supported by a careful error analysis. The data analysis will be carried out in two different domains or stages:

- Probability Domain

  This involves computing the *statistical distributions* of measured data at different, separate transfer steps (wave elevation - wave kinematics - hydrodynamic loads - structural response, for example). Existence of nonlinearities will cause distortions in the statistical distributions from one step to another. For example, quadratic drag will convert a Gaussian distribution (wave kinematics) to a Pierson-Holmes type of distribution (Wave loads) - see Pierson and Holmes (1965) and Burrows (1979). Consequently, the ratio of the Most Probable Maximum (MPM) force to the root mean square (rms) force from the short-term statistics will be significantly increased; assuming 1000 peaks which corresponds approximately to a three-hour storm, in a pure inertia condition, this ratio is about 3.7 (Gaussian Distribution), while with a pure drag case, this ratio is increased to 8.6 (an extreme case of Pierson-Holmes Distribution). Other forms of nonlinearities will complicate this problem further. Knowledge of this distortion effect and thus the resulting response distribution after each transfer step is important for both extreme and fatigue analysis of a jack-up. Besides, variations of the statistical distributions at different steps can be used to detect nonlinearities. The probability domain analysis involves one time series at a time and does not (directly) relate any one time series to another.

  The probability analysis results provide information about how the energy is distributed among the motion levels. For example, two loading histories can contain the same energy spectrum: one consists of a series of cycles with medium force while another has a portion of low force and a portion of high force. These two loading series will have obviously different probability distributions and different impact on the structural behavior, however.

- Frequency Domain

  This involves the following computations: the *autospectrum* of an individual measured time series, the *gain factor* (the modulus of the frequency response function, which is of primary interest for the jackup analysis) and *phase factor* (the phase angle of the frequency response function) between a pair of measured time series, the associated *coherence function* and so forth. With a nonlinear system the gain factor as well as other inter-step parameters will generally not be constant; instead, they will be dependent upon the input energy level. Nonlinearities can also be exposed (to some extent) or in other words isolated by comparing the coherence functions between various transform steps. (The coherence is always unity for a perfectly linear transformation.)

The spectral analysis results shed light on the energy distributions and their transfer relationship as a function of frequency.

The estimates of statistical quantities either in the probability domains or the frequency domain are inevitably accompanied by errors. There exist two kinds of errors: (1) *bias error* which is a systematic error occurring with the same magnitude in the same direction when measurements are repeated under identical circumstances and (2) *random error* which is that portion of error that is not systematic and can occur in either direction with different magnitudes from one measurement to another. The statistical errors (both bias and random errors) should be estimated carefully; an irresponsible processing of random data can cause so big an error in the results that any interpretation becomes totally meaningless.

The analysis of the measured data in the probability domain and the frequency domain are discussed separately in Sections 7.3 and 7.4 and the detailed mathematical formulations for the associated error analysis are given in Appendix IX.
In light of the insight gained from the data analysis, the dynamic behavior of the models in the irregular waves are simulated with *NOSDA* using the schematizations established in Chapter 6; the results are presented in Section 7.5.
Limited by space, only a few representative results are included in this chapter. More detailed presentations and interpretations are to be found in a separate report by Liu (1991).

7.2 DATA COLLECTION AND PREPROCESSING

This section discusses the gathering and preliminary processing of the model test results using irregular waves. These data provide the input to the statistical analyses later in this chapter.

7.2.1 **Data Recording**

Twelve channels were used to record the measured signals using an analog instrumentation recorder (*IR*): 6 channels were used for the bottom reaction forces (x and z components for each leg), 4 channels for the x and y components of the deck displacement at locations A and C (see figure 3.1), 1 channel for the x direction deck acceleration at location D, and 1 channel for the wave elevation.

Besides the *IR* recording, a *UV* recorder was used to record ten channels (six of them were the same as the *IR* recording). The *UV* recording was mainly used for the on-site visual control and for providing a first group of data for static, free vibration and regular wave test processing as indicated in the previous chapters. The present chapter will focus on the processing of the irregular wave data recorded on the instrumentation recorder.

7.2.2 **Data Digitalization**

Before the analog data were digitized, they were low-pass filtered at 5 Hz using 12 hardware filters in order to suppress the measurement noise.

The analog signals were digitized using a Data Acquisition System (*DAS*). The sample frequency of the *DAS* was set to be 20 Hz. The choice of 20 Hz sample frequency was made based upon the consideration that the same digitized data could also be used for the time domain analysis where a finer grid would be required. For the present processing in both the probability domain and the frequency domain the sampling frequency actually used will be 10 Hz. This means a 2nd-order decimation will be applied to reduce the amount of data to one half after the data are digitized and converted to the proper physical units.

The *DAS* system used has 14 bits (with sign); the full scale of input between -10 V and + 10 V was equally divided into 32766 intervals, corresponding to 32766 equally spaced levels.

The relative time delay phase shift due to filtering and digitalization has been checked and proven to be negligible (the total shift from the first channel to the last channel is less than 200 μs.)

7.2.3 **Data Preprocessing**

The measured time series are preprocessed by using a high-pass (numerical) filter. All waves longer than half of an individual record segment (defined in Section 7.4) are filtered out. Attention in the present study is focused on the vicinity of resonance; low frequency secondary waves are expected to be of minor importance for the response of

the structures tested. All the series have already been analogously filtered at 5 Hz low pass. This choice of upper cutoff frequency leaves possible 3rd harmonics (generally lower than 3 Hz) intact.

The filtering is carried out in the frequency domain; this corresponds to multiplying the Fourier Transform of the data record by the frequency response function of the desired filter and then taking the inverse transform. The software used to do the FFT does not require the number of the input data be an exact power of 2. The author's experience, however, shows that the quality of filtering increases significantly when this number is a power of 2. Therefore, the time history of each run is divided into two sections: one contains 16384 (= 2^{14}) data points (= 819.2 s) and the other contains 4096 (=2^{12}) data points (= 204.8 s). After filtering, the two sections are merged together again.

The digitized data so far obtained do not represent physical units. A unit conversion procedure is applied for each individual channel of each individual run to make the data physically meaningful.

After the conversion, a 2nd-order decimation is employed to all time series to reduce the amount of the data to half; the 20480 data points of each channel resulting from the conversion is cut down to 10240 points (= 1024 s). The decimated series (10 Hz sampling frequency) will be used as the input data for the statistical and frequency analyses in the following sections.

7.3 PROBABILITY ANALYSIS RESULTS

The traditional approach to this problem emphasizes the comparison between theoretical distributions and actual distributions derived from each measured time series: testing the normality of the instantaneous values, comparing the distribution of the measured peak values with the Rice distribution, verifying whether the distribution of the extreme values is of Poison type, and so forth. Many researchers have dedicated considerable effort to this type of analysis; much valuable information is already available - see Anon. (1983) and Battjes and van Heteren (1983), for example. A preliminary check following this traditional line has been performed using the observed data. Both the direct frequency histogram comparison and the Kolmogorov-Smirnov (or *K-S*) test (the most generally accepted test for continuous data - see, for example, Press *et al.* (1986)) involving even the very first 'primitive' group of data - instantaneous wave surface elevation - showed

deviations from the expected theoretical Gaussian Distribution. Further processing along this line was not expected to lead to any new or conclusive results. Since the main objective of the present work is to investigate the influence of the nonlinearities involved, statistical analysis here will focus instead on the distortions in the statistical distributions from one step to another caused by the existence of nonlinearities.

Since most of the possible skewness has been excluded by high-pass filtering, the crests and troughs are not distinguished in this analysis. It should be noted that skewness (or asymmetry) could result from both the (true) physical process (such as structural plasticity, dry friction, secondary waves, free surface effect, etc.) and the (false) instrumentation shift. Apparent instrumentation shift was observed in the time series record. Since it is difficult to differentiate this shift from the realistic physical asymmetry, the whole skewness is indiscriminately excluded from the time record by the high-pass filtering. Consequently, this could eliminate some effects - especially on the response statistical distributions caused by nonlinearities.

The distortion in the probability distributions (with the exception of the mean shift which is ruled out by the high-pass filtering and data normalization) caused by various nonlinearities is demonstrated by comparing the curves of the chance of exceedance for two different quantities (the wave elevation versus side sway or the side sway versus bottom reaction, for example).

Higher order harmonics in a response introduced by nonlinearities are the primary cause of its statistical distribution being different from that of its input. Quadratic drag introduces higher order wave force components. In the present tests, the natural frequency of the structure is close to the wave peak frequency (see tables 3.1 and 3.3); the first order effect is dominant in the response while higher order terms are suppressed (filtered out) to some extent in the response. Therefore, the response often tends to be more Gaussian-like than the hydrodynamic force excitation. The distortions of probability distributions found between the wave surface and structure-related quantities (such as the deck displacement and bottom reactions) are a net effect of physical nonlinearities counteracted by dynamic amplification filtering.
An implication of this phenomenon is that a linear looking overall system can contain significant internal nonlinearities. This is also discussed by Massie, Liu and Zeelenburg (1991) from another angle.

The choice of interval between two succeeding histogram steps or levels is a compromise between bias suppression and random error suppression. A large interval is desirable to reduce the random error, while a small interval is needed to suppress the bias error. This interval is selected here to minimize total error of estimates. With the parameters chosen, the normalized bias error associated with (cumulative) probability distribution estimates is restricted to less than 1% and normalized random errors are limited to less than 5% with all models. This lends confidence to the results obtained from the present frequency analysis. The detailed mathematical formulations of the statistical error analysis for probability estimates are given in Appendix IX.2.

7.3.1 **Relative Motion Type**

When relative motion combined with quadratic drag is the only important nonlinearity involved (Model I), neither the comparisons of chance of exceedance between the water related quantity and structure-related quantities (wave elevation versus deck displacement and wave elevation versus bottom reaction forces), nor those among the inter-structural quantities (deck displacement versus bottom forces, vertical force versus horizontal force) show noticeable difference - see figures 7.1 and 7.2.

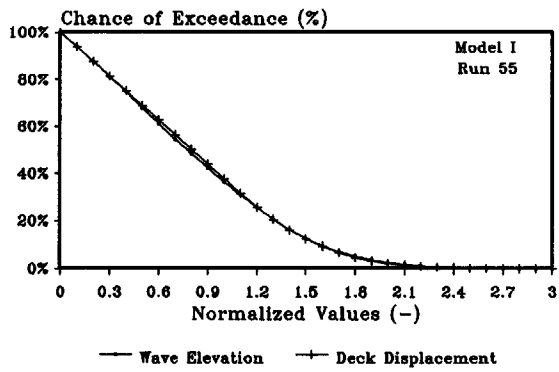

Figure 7.1 Chance of Exceedance: Wave Elevation and Horizontal Force

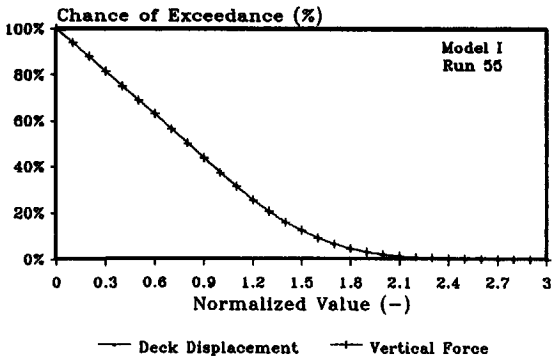

Figure 7.2 Chance of Exceedance: Deck Displacement and Vertical Force

These comparisons indicate that relative motion does not have a significant impact on the response probability distribution.

7.3.2 **Drag and Nonlinear Structure Type**

When drag and structural nonlinearity are important, the comparisons between the chance of exceedance of the wave elevation and those of the response show a clear deviation. A typical example of this is given in figure 7.3. This figure shows that when compared with the chance of exceedance of the wave surface elevation, the deck displacement response chance of exceedance drops more rapidly at the lower range, then slows down gradually and at a certain point becomes higher. (This means that there are more extreme response data than corresponding excitation data.) If the whole physical process (the structure standing in waves) were seen as a filter, the function of this filter would be to stretch an input (wave elevation distribution) to a more extreme response (structural displacement or bottom forces distribution). The transfer within the structure itself (side sway to bottom force, for example) also distorts the distribution; the degree of these distortion was found to be less profound than that from the water surface elevation to any structural response quantity, however. It seems that the stretching effect is primarily caused by the hydrodynamic drag while the structural nonlinearity (complicated deck-leg connections) plays a less significant role.

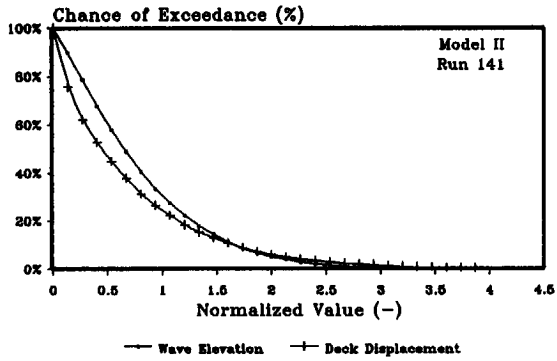

Figure 7.3 Chance of Exceedance: Wave Elevation and Deck Displacement

The influence of the P-δ effect on the probability distribution is examined by comparing the curves of chance of exceedance of inter-structural quantities calculated for Model II-M. Although this model has an exaggerated P-δ effect (the ratio of the equivalent deck weight to the Euler critical load is 36.8% with this model), the distributions of the measured deck displacement and reaction force are still quite similar - see figure 7.4; the influence of the P-δ effect on the response probability distribution is marginal. This indicates that the influence of the P-δ effect on the overall dynamic behavior of the model is basically linear and the nonlinear contribution of this effect caused by the varying axial forces along the legs is negligible.

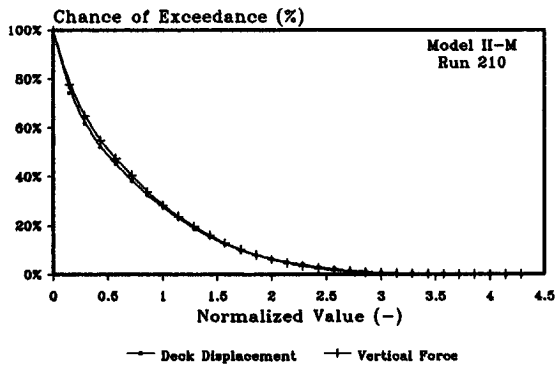

Figure 7.4 Chance of Exceedance: Deck Displacement and Vertical Force

7.4 SPECTRAL ANALYSIS RESULTS

It should be pointed out first that the spectral method theory was originally developed for analyzing a constant-parameter linear system. With the system under investigation the constant-parameter assumption is valid while the linearity assumption is apparently violated. However, the application of this approach to determine system cross characteristics (coherence function, frequency response function and thus gain factor and phase factor, for example) will produce the best linear approximation (in the least square sense) of those characteristics *associated with the specific input and output conditions*. For different inputs, the frequency response functions so determined are generally different.

It is also worthwhile to note that recent developments in spectral analysis techniques make it possible to identify a nonlinear system in more detail provided the nonlinearities are well formulated in principle. The basis of the more sophisticated spectral approaches is to decompose a nonlinear system into linear, bilinear and trilinear parts. In turn, the bilinear part is modeled as a zero-memory squarer followed or preceded by a linear operation with finite-memory and the trilinear part as a zero-memory cuber followed or preceded by a linear operation with finite-memory. For example, the hydrodynamic wave forces on a fixed small diameter cylinder are first split into inertia and drag parts; the inertia part is treated by a linear operation and drag part is replaced by the sum of a linear operation plus a cubic operation and this sum is again put through a linear finite-memory operation - see Bendat (1990) for more details. The application of these new techniques involves much more computational work and demands precise knowledge and realistic mathematic formulations of the nonlinear physical processes that are far from well known in the present case. The attention in this work, therefore, is aimed at qualitative identification of nonlinearities and their influence on the dynamic behavior of the structure by employing the more mature 'linear' spectral technique.

The time series have been preprocessed as described as in Section 7.2. Additional preparations of the data are necessary for the frequency analysis. These preparations include three steps: segmenting, overlapping and windowing. All of them are carried out to improve the accuracy of the resulting estimates. This is only briefly recapitulated here; a more extensive discussion about these three preparations is given in Appendix VIII.

In order to obtain smooth spectral estimates, each time record is divided into segments. The choice of the number of data segments in the spectral analysis is critical to the overall error of the results especially when the spectra concerned are narrow-banded. Random error increases and bias error decreases with a decreasing number of segments in a fixed total record length. The number of segments is chosen here to minimize the total error - see Appendix IX, especially Section IX.3, for more details. The number of segments actually used is 20 for model I and 40 for Models II and II-M. The frequency resolution bandwidth resulting from this segmentation guarantees that there are at least ten grid points within the energy-rich range of frequencies, while the degree of smoothing is nearly optimal as well.

The Hanning window is employed to taper the time series. 50% overlapping is used to improve the accuracy of estimates as well as to compensate for the information loss due to windowing. Accordingly, the equivalent number of segments after overlapping is increased to 32 and 64 for Model I and Model II(-M) - see Press, *et al.* (1986).

The computation principles used in *RANDA* generally follow the line given by Bendat and Piersol (1971 and 1986) and will not be extensively discussed here.

The computations involve estimates of autospectra and joint record spectral functions. The term '*joint record spectral functions*' refers to the coherence function, the frequency response function and thus the gain factor as well as the phase factor; these all link one time series to another.

Interpretation of the results obtained in the following frequency analysis focuses on exposing nonlinear influences. These show up most prominently in joint record functions. Note that bias error suppression with joint record function estimates reduces only that portion caused externally due to either the computation procedure or instrumentation. The bias error caused by nonlinearities is inherent in the system being investigated and, in fact, is the phenomenon being sought; this bias gives an indication of the influences of various nonlinearities - see also Liu, *et al.* (1991).

Besides the normalized bias and random errors, a 95% confidence interval is also computed for each spectral estimate to give a vivid illustration of the scope of likely true values. The details about the error analysis and confidence intervals for spectral estimates are given in Sections 3 and 4 of Appendix IX, respectively.

A general tendency common with all models and all runs is that the response spectra are systematically narrower than those of their excitation. This signal filtering effect can be physically explained by the structural dynamic amplification. Note this phenomenon is not universally true; when the dynamic amplification causes a twin-peaked response spectrum, the spectral width parameter (ϵ_m) defined by spectral moments (m_i) can well be wider than that of input spectrum. Additionally, the waves generated in these tests were relatively narrow-banded; this was especially true with the Model I tests. It should be emphasized that it is the narrowness of the spectra that makes the present frequency analysis extra difficult; bias suppression requires such a high bandwidth resolution that one has very little room left for random error suppression; an optimum balance is vital for success. Fortunately, spectra measured in a real sea are generally wider; error suppression is expected to be less critical with prototypes.

7.4.1 **Relative Motion Type**

The coherence between the waves and the deck displacement as well as waves and the bottom reaction force with Model I is rather high (up to 0.98) in the vicinity of the peak frequency of the input waves - see figure 7.5. The notation system is chosen as follows: the horizontal-axis is the frequency, f ; the solid curve is the value of interest (the coherence function in this case), encompassed by the 95% confidence interval (shown in the figure as the two fine dashed curves); and the coarse dashed curve down at the bottom of the figure is the normalized random error as a percentage. In the figure (-) denotes that the quantity is dimensionless and ϵ_r is the normalized random error. Note that the results are plotted only in the range where the spectral values are significant. The generally high coherence values in figure 7.5 show that the influence of nonlinearity (here primarily relative motion) on the structure dynamic behavior is generally small. On the other hand, the coherence has a dip in the neighborhood of resonance near f = 0.87 Hz. This indicates that relative motion has a more profound influence near resonance. A logical explanation for this is that the nonlinearity caused by relative motion manifests itself as damping which is most apparent only near resonance. Since in the present case the input energy level at true resonance is relatively low, the impact of this relative motion damping on the overall dynamic behavior is expected to be less significant. Figure 7.5 also shows that the 95% confidence interval is narrow. The normalized random error for the coherence estimate is less than 5% in the energy-rich range of frequencies; this value is also representative for other joint record estimates between the wave elevation and structure-related quantities for Model I.

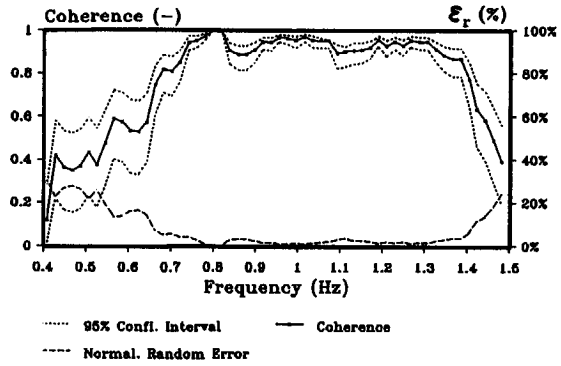

Figure 7.5 Coherence Between Wave Elevation and Deck Displacement

The coherence between inter-structural quantities is even higher; an example is given in figure 7.6. This perfect coherence should be expected since the structure is reasonably linear (The deck to leg connection of Model I was glued). This figure also shows that the normalized random errors associated with this estimate is rather low (typically within 1%); this error range is also representative for other joint record estimates of inter-structural quantities. Although the record segmentation with this model is relatively coarse (to suppress bias error), the final random errors of the joint record estimates are still low; this comes from the high coherence.

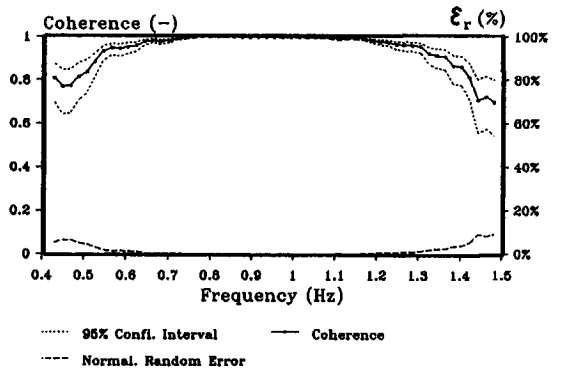

Figure 7.6 Coherence between Deck Displacement and Horizontal Force

RAO for deck displacement with irregular waves is defined as the gain factor between the wave elevation and the deck displacement. (A gain factor is the modulus of the frequency response function which is determined here as the cross-spectrum between the input and output divided by the input spectrum.) Superimposing the RAOs for three most representative wave heights (Run 58 with the lowest significant wave height H_s = 2.93 cm, Run 56 with the highest H_s = 4.44 cm and Run 59 with the middle value H_s = 3.49 cm) yields figure 7.7. It shows that irregular waves with different significant heights result in different RAOs - especially near resonance. This deviation is not as obvious as with regular waves shown in figure 6.5 which is repeated here for better comparison.

This disparity can be explained by the fact that a sinusoidal wave with a frequency coincident with the resonant frequency will generate a larger structure response than irregular waves. The relatively lower irregular wave structural response compared to the wave elevation causes a more modest relative motion effect as well. Even so, the general tendency that a higher wave causes a higher level of hydrodynamic damping (thus a lower RAO) remains valid with irregular waves; it is less apparent, however.

Just as with the regular wave tests in figure 6.5, a slight 'dent' can also be observed in the neighborhood of 1.2 Hz with the irregular wave tests of figure 7.7 - this dent is clearer in tabulated data. This effect is caused by hydrodynamic cancellation.

The nonlinearity caused by relative motion seems not to have a significant impact on the average magnitude of the RAOs in irregular waves compared with that in regular waves. Since a different input level will cause a different RAO curve, a comparison between results with regular versus irregular waves should be done on a comparable wave height basis. However, the definition of an irregular wave comparable with a regular wave is inevitably subjective. There are two simple approaches in use: (1) Assume that the significant wave height of irregular waves equals the wave height of a regular wave; (2) The energy contained in the irregular waves is the same as that contained in the regular waves, (in other words, their standard deviations are identical). The first approach provides an irregular wave height that is visually about 'equal' to that of the regular

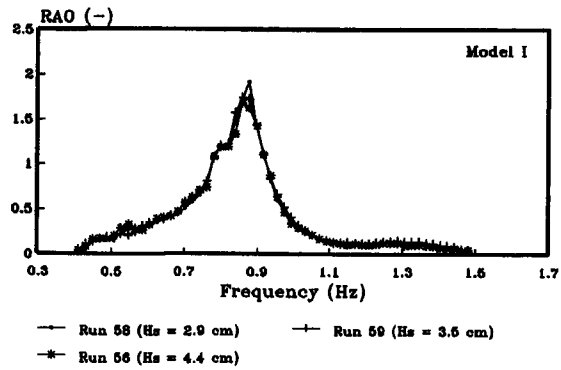

Figure 7.7 RAOs for Different Wave Heights (Model I, Irregular Waves)

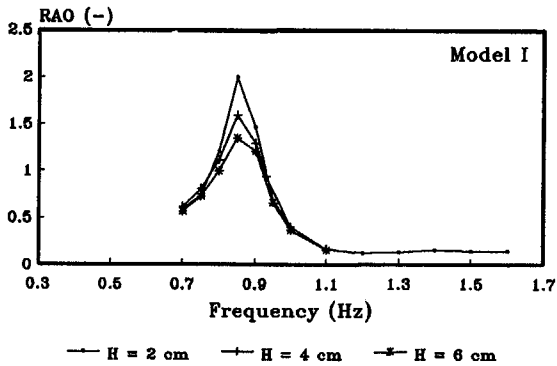

Figure 6.5 RAOs for Different Wave Heights (Model I, Regular Waves)

wave; the regular wave will contain about $\sqrt{2}$ times as much energy as its irregular counterpart. The second definition guarantees the conservation of energy, while it underestimates the contribution from larger waves. It seems to the author that the most reasonable definition should be somewhere in between these. For example, the representative wave height could be defined by averaging the results from each of these definitions as $H_r = \frac{1}{2}(H_s + 2\sqrt{2}\sigma_\eta) \approx (2 + \sqrt{2})\sigma_\eta \approx 0.85\, H_s$ - where σ_η is the standard deviation of the wave surface. An example of the RAO comparison using this approach is given in figure 7.8. Here, with the significant wave height of the irregular waves of

2.93 cm, then the corresponding comparable wave height should be around 2.5 cm, the 'closest' regular waves recorded are those with height of 2 cm. This figure demonstrates that the RAOs computed from irregular and regular waves can be quite similar.

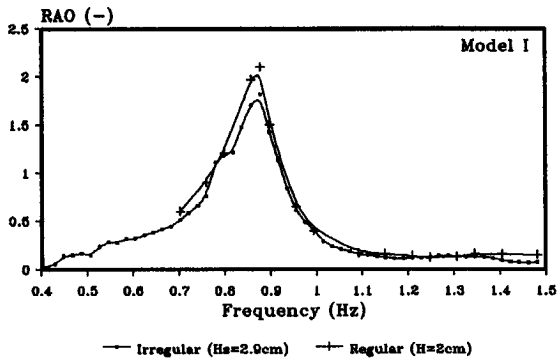

Figure 7.8 Comparison of RAOs: Regular and Irregular Waves (Model I)

7.4.2 **Drag and Nonlinear Structure Type**

Models II and II-M are hydrodynamically more drag dominated and have a somewhat nonlinear deck to leg connection. The wave spectra and the RAOs with these models are noticeably wider than those with Model I. The response spectra are therefore wider, too. Consequently, bias suppression is less critical. The bandwidth resolution used for these models is twice as wide as that used with Model I; this means that a greater number of equivalent record segments (64 compared with 32 with Model I) are available for estimate smoothing.

The RAOs for various wave heights are compared in figure 7.9. The RAO magnitude shows a definite dependency on these heights. The general trend is that the RAOs increase with increasing input level and the RAO peaks shift to the left with increasing wave heights; this is qualitatively in agreement with results obtained from the regular wave tests - see figure 6.6 (repeated here). Such dependency is caused by nonlinearities. There are at least two factors contributing to this dependency in this case: (1) the structure's stiffness decreases with increasing loading level and (2) the drag term increases quadratically with increasing wave heights.

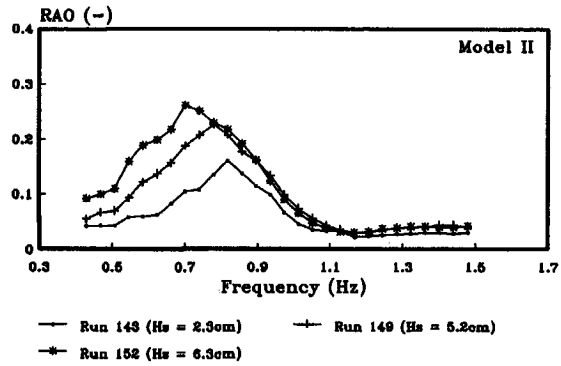

Figure 7.9 RAOs for Different Wave Heights (Model II, Irregular Waves)

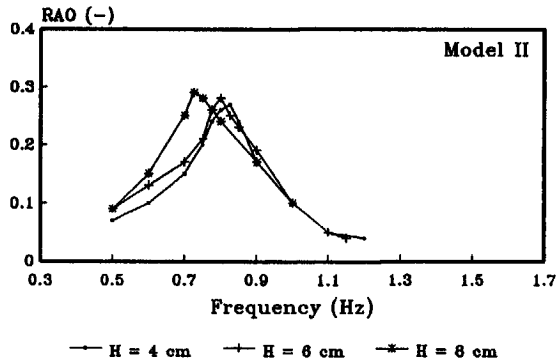

Figure 6.6 RAOs for Different Wave Heights (Model II, Regular Waves)

Once more, cancellation is observed near 1.2 Hz in figure 7.9 (The regular wave tests did not reach or pass this frequency with these models).

Furthermore, the RAOs also seem dependent of the input energy distribution as a function of frequency. This is shown in figure 7.10. The significant wave height of Run 141 (H_s = 3.22 cm) is approximately equal to that of Run 145 (H_s = 3.39 cm), while Run 145 has a higher peak frequency (f_p = 0.82 Hz) than Run 141 (f_p = 0.74 Hz). It can be seen from this figure that Run 145 yields a higher RAO peak.

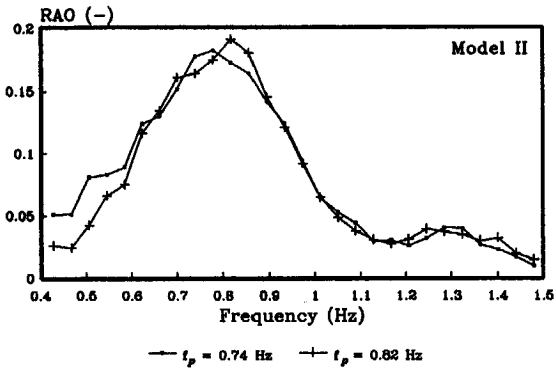

Figure 7.10 RAOs for Different Peak Frequencies

The magnitude of the RAOs computed from irregular waves are found to be lower than those computed from regular waves. For example, the significant wave height of Run 149 is 5.20 cm, and its comparable wave height is about 4.4 cm. The closest wave height in the regular wave tests is 4 cm; superimposing the two associated RAO curves yields figure 7.11.

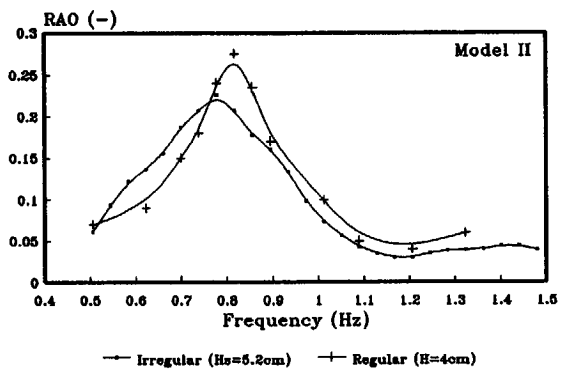

Figure 7.11 Comparison of RAOs: Regular and Irregular Waves (Model II)

The possible reasons for this RAO reduction in irregular waves are:

a. Inherent bias of the spectral analysis technique. The response will be partly decomposed from the peak frequency to higher frequencies. Assume $x = \sin 2\pi ft$ and $y = |\sin 2\pi ft| \sin 2\pi ft$, (in fact, this is a simplified pure drag case), then the gain factor computed from the time domain is obviously 1, while the gain factor computed using the frequency analysis technique is only about 0.85 at f. As such, the reduction in RAOs implies the importance of the hydrodynamic drag term.

b. A sinusoidal wave with a frequency identical to the natural frequency of the structure will excite more response than comparable irregular waves. This is caused by the fact that the wave components with different frequencies in the irregular waves tend to cancel each other and the structural dynamic amplification unequally enhances the response along the frequency axis (only that portion of the response due to the irregular wave components with frequencies near the structural natural frequency is so strongly amplified as the regular wave counterpart). With the present models, the structural stiffness decreases with increasing displacement. The decrease in the stiffness will be fed back and show up as a higher RAO value.

The coherence functions between the water-related quantity and structure-related quantities are found to be lower than those with Model I and less than 0.9. As an example, the coherence function between the water surface elevation and the deck displacement as well as the coherence function between the water surface elevation and bottom horizontal reaction force are plotted in figure 7.12. On the other hand, the coherence functions between structure-related quantities remain close to unity - see figure 7.13. All these indicate that the water related nonlinearities and wave-structure interaction have a major impact on the coherence. Hydrodynamics is the dominant nonlinearity, while the structural nonlinearity (mainly due to the imperfection of the deck-leg connection) apparently plays a less significant role.

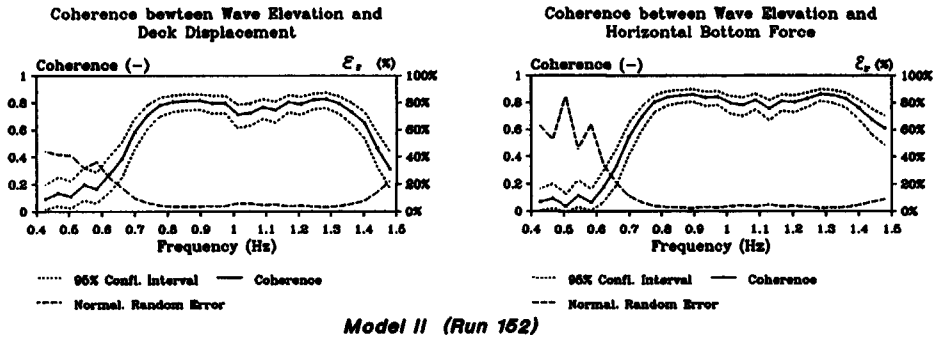

Figure 7.12 Coherence between Water-Related Quantity and Structure-Related Quantities

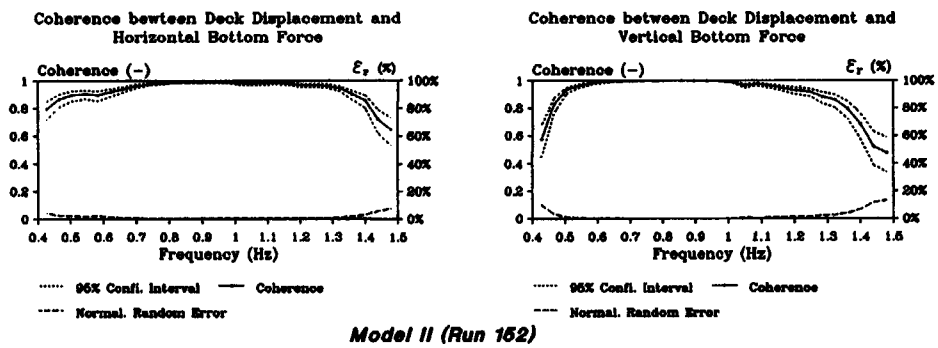

Figure 7.13 Coherence between Inter-Structural Quantities

It can also be seen from figures 7.12 and 7.13 that the random errors are rather low (restricted to less than 5% in the energetic area) associated with the joint record estimates between the wave elevation and structure-related quantities and even lower (less than 1%) between inter-structure quantities. These error analysis results indicate the reliability of the joint record estimates.

7.5 MEASURED VERSUS SIMULATED RESULTS

The analyses in the previous sections are factual; they focused on gaining insight into the dynamic behavior of the models by examining the recorded data from the tests. The present section deals with the *NOSDA* simulations of the model behavior using the schematizations established in Chapter 6.

The autospectra and probability distribution of the input wave surface elevation and the corresponding responses have been obtained earlier in this chapter. The quality of the *NOSDA* irregular wave simulation will be checked by comparing the spectra and probability distribution of the response time series simulated using the measured wave spectra as the input with those of the measured response time series.

The irregular wave surface profile is reproduced using wave superposition (also known as Random Phase Theory). The phase information lost in the spectrum representation is compensated by supplying a group of randomly generated 'artificial' phases from a uniform distribution in the range $(0, 2\pi)$. The amplitude of each wavelet follows (deterministically) from the wave spectrum. It should be noted that the wave surface (and thus the kinematics) reproduced using deterministic amplitude (also called constrained wave simulation) does not strictly satisfy the condition of a Gaussian process unless the number of wave components approaches infinity. A alternative scheme is to generate Rayleigh random amplitudes combined with uniform random phases - see Tucker, *et al.* (1984). An important limitation of the constrained model is that it may incorrectly reproduce wave group statistics - or the 'groupiness' of the waves which can have a profound effect on ships, moored structures, etc. However, the models tested in the present study are relatively stiff and thus not sensitive to such low frequency wave excitation, therefore. The deviation from the Gaussian distribution caused by the constrained wave reproduction scheme is expected to be unimportant for the present model simulation. In fact, the wave surface measured in the present tests is not strictly Gaussian, either. An additional advantage for using the constrained wave reproduction model is that it guarantees a stricter conservation of the total input wave energy.
The spectrum and probability distribution of the wave surface so reproduced are checked with those of the wave surface measured (the target spectrum and probability distribution). The comparison is satisfactory.

The wave kinematics are predicted using linear wave theory (summing the contributions from all wave components). The validity of such a linear wave model for kinematic prediction in unidirectional irregular waves has been confirmed in the MaTS investigation (the Netherlands program for Marine Technological Research) - see Anon. (1983).

Note that the wave surface and the corresponding wave kinematics so simulated will repeat themselves after a time segment, $T_s = 1/B_e$ (where B_e is the frequency resolution used in discretizing the wave spectrum). This repetition is avoided by regenerating random phases after each T_s.

Just as with the regular wave simulations, the free surface effect on the wave kinematics is included using the Wheeler stretching approach.

Given the (resultant) velocity and acceleration, the hydrodynamic load is computed using the modified Morison Equation. The extension of the Morison Equation to irregular waves has been validated in a project jointly performed by SIPM (Shell International Petroleum Maatschappij) and MaTS - see Vugts and Bouquet (1985).

As discussed in Chapter 5 and Section 7.4.2, irregular waves will excite less response than a comparable sinusoidal wave with a frequency identical to the natural frequency of the structure. With Model I, the RAO value - which gives an indication about the ratio between the model leg motion to the water particle motion - is up to 2.0 with regular wave tests (near resonance), while the typical value of the ratio between the root mean square deck displacement and rms wave elevation is around 1.0 with irregular wave tests. Therefore, the influence of the structural motion on the hydrodynamic coefficients are expected to be less significant with the irregular wave tests than with the regular wave tests. In light of this, the C_d and C_m coefficients for the irregular wave simulations are chosen to be 0.7 and 2.0, respectively; these are closer to those given by Chakrabarti (1986) for a fixed cylinder (C_d = 0.5, C_m = 2.3), compared with 0.8 and 1.8 with the regular wave simulations. With Model I simulations, 25 harmonics (0.5 to 1 Hz with a resolution of 0.02 Hz) are used to reproduce the irregular wave profile and kinematics. The spectrum and chance of exceedance of the simulated deck displacement are compared with those of the measured deck displacement in figures 7.14 and 7.15.

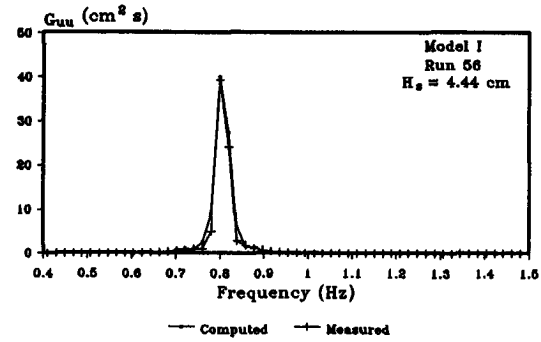

Figure 7.14 Measured and Computed Response Spectra (Model I, Deck Displacement)

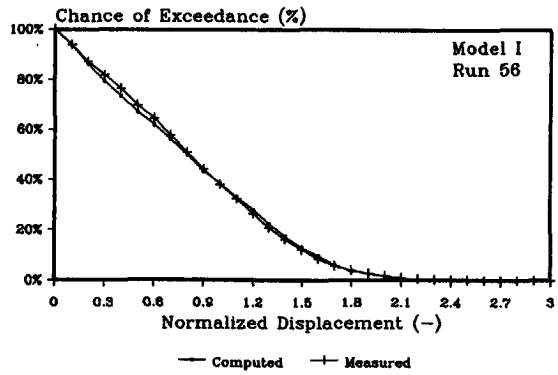

Figure 7.15 Chance of Exceedance: Measured and Computed Deck Displacement for Model I

The results from other models (II and II-M) are presented here before conclusions are drawn. These models are of the drag and structurally nonlinear type; the relative motion plays only a minor role. The hydrodynamic coefficients for these models are extracted from Chakrabarti's results (1986). With these models, 27 sinusoidal waves (0.45 to 1.5 Hz with an interval of 0.04 Hz) are used for irregular wave representation. A comparison of the computed and simulated deck response is given in figure 7.16 and 7.17 in terms of the spectrum and chance of exceedance.

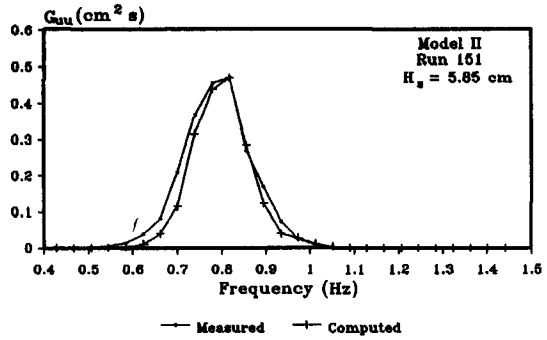

Figure 7.16 Measured and Computed Response Spectra (Model II, Deck Displacement)

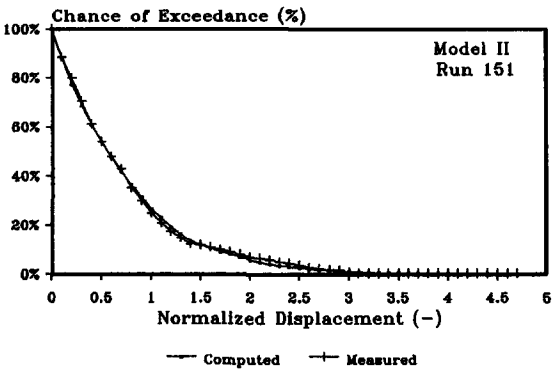

Figure 7.17 Chance of Exceedance: Measured and Computed Deck Displacement for Model II

The conclusion for all of these models is that the probability and spectral properties of the response from the NOSDA simulation match well with those from the physical models with statistically equivalent input. This is true for the relative motion type as well as the drag plus nonlinear structure type models; this validates the *NOSDA* simulation in irregular waves.

The *NOSDA* simulation with irregular waves is obviously more time consuming than with regular waves. Since more waves (instead of one single wave) are superposed to calculate the instantaneous wave surface and wave kinematics, more computing time is needed in the hydrodynamic part. More specifically, in the present study, the time step

is chosen to be 0.05 s and the wave peak frequency is around 0.8 Hz. Therefore, there are about 25 data points per primary cycle. Using the same structural models as used with regular wave simulations and 25 to 27 waves representing spectra, a simulation of 1034 s clock time uses around 8000 s of CPU time on the DECstation 3100 . The ratio of the simulation time to the physical time is about 8:1, which is roughly 8 times as costly as compared with the corresponding regular wave simulation.

7.6 SUMMARY

The experimental data from three principle jack-up models under irregular waves have been processed and analyzed in a responsible way. The data were examined both in the probability domain and frequency domain using *RANDA*. The results increase the insight about the behavior of such rigs at a random sea. Furthermore, the model behavior was well simulated using *NOSDA*. More specifically:

7.6.1 **Data Analysis**

Probability Domain

1. Relative motion does not noticeably distort the response probability distribution. An additional influence of structural motion manifests itself in the spectral analysis, however; see item 1 in the frequency domain results below.
2. The deck-leg connection nonlinearity plays only a minor role in distorting the statistical distributions of response.
3. Existence of drag apparently stretches the response distribution as compared with that of the water elevation - the response distribution contains larger extremes than does the water surface elevation.

Frequency Domain

1. Relative motion when combined with (even minor) quadratic drag manifests itself as damping. The general trend in RAO caused by relative motion is that the RAO peak decreases with increasing wave height - this is in agreement with the observation from the regular wave tests. When relative motion is the main contributing factor of nonlinearities, the average magnitude of RAOs computed from irregular waves and that computed from regular waves are of the same order.

2. Existence of drag causes a definite input energy level dependency of the RAOs; higher waves result in higher RAOs both in regular and irregular waves. In this case, RAOs computed from irregular waves are generally lower than those computed from comparable regular waves.
3. The magnitude of RAOs are also (weakly) dependent upon the relative locations of wave peak frequencies and structure resonance frequencies.
4. Limited hydrodynamic cancellation is observed around 1.2 Hz for all three models in irregular waves; this confirms the results from the regular wave tests and theoretical prediction.
5. The inter-structural coherence of the measurements is noticeably greater than that between waves and structural response. This indicates that nonlinearities are primarily of a hydrodynamic nature.

Data Analysis Aspects

1. In the probability domain analysis, the choice of interval between two succeeding histogram steps or levels is a compromise between bias suppression and random error suppression. A large interval is desirable to reduce the random error, while a small interval is needed to suppress the bias error. This interval is determined here to minimize total error of estimates. The normalized bias error associated with the distribution estimate is less than 1%, and the normalized random error is restricted to less than 5% with all models.
2. The choice of the number of data segments in the spectral analysis is critical to the overall error of the results. Random error increases and bias error decreases with a decreasing number of segments. The number of segments is chosen here to minimize the total error. The normalized random error associated with estimates of spectral quantities relating hydrodynamic to structural response is usually less than 5% and that for inter-structural estimates is less than 1% over the energy-rich range of frequency for all models.
3. If the wave spectra and RAO are narrow, extra care is needed in the spectral analysis.
4. An important experience gained through the present random data processing is that a careful error analysis is essential in this type of study. Computer software for analyses such as these will **always** produce results. Blind analysis of random data can lead to equally random results.

7.6.2 Computer Simulations

1. The comparison between the simulated and measured response is satisfactory; this confirms the applicability of *NOSDA* to a stochastic sea.
2. The computational effort for the *NOSDA* simulation in irregular waves is acceptable with the present models. Using a DECstation 3100 computer, the ratio of the simulation time to the physical time is about 8:1.

Chapter 8
Conclusions

The work included in this dissertation is aimed at investigating the influence of nonlinearities on elevated jack-up rigs. The nonlinearities studied here originates from hydrodynamic interaction and structural behavior. Both experimental and computational approaches have been used. Testing on three principle jack-up models (I, II and II-M) has been carried out in a wave tank. Two software packages, *RANDA* and *NOSDA*, have been developed parallel to the laboratory studies. The *RANDA* software was used for processing the random data from the irregular wave tests. *NOSDA* was developed as a software package for stochastic, nonlinear, dynamic analysis of general, moving, slender-element offshore structures. As a specific application, *NOSDA* was used to simulate the dynamic behavior of the models tested in the lab. More specific conclusions from this investigation are drawn in the following sections.

8.1 MODEL TESTING AND EXPERIMENTAL DATA PROCESSING

The models tested involved both hydrodynamic and structural nonlinearities, but the different models have different types of nonlinearities. Model I includes a significant relative motion, Model II has a high drag contribution plus a complicated deck-leg connection; with an extra mass on the deck, Model II-M demonstrates the influences of the P-δ effect further. This segregation of nonlinearities with different models helps isolate and thus better expose the influences of an individual nonlinearity on the behavior of the structures.

The experimental data have been carefully processed and analyzed. The measured data from the irregular wave tests were examined both in the probability domain and frequency domain using the *RANDA* software. This with the error analysis lends confidence to the conclusions concerning the model behavior when subjected to irregular waves. The irregular wave test results, especially when compared with those from the regular wave tests, increase the insight about the behavior of such rigs in a random sea.

The following more specific conclusions can be drawn from the present experimental study (the most relevant sections in the previous text are indicated at the end of each item):

- Discrepancies between the stiffness obtained from static tests and that inferred from dynamic vibration tests have been observed both in the field (by others) and in the present lab models. The apparent dynamic stiffness of a model was found to be up to 4 times its static stiffness. This dynamic stiffness enhancement of the present models is caused by the large local damping at the deck-leg connection, which effectively makes the connection rigid. (See section 4.2.2.)
- When structure motion combined with quadratic drag is the main nonlinearity, higher waves cause lower Response-Amplitude-Operator (RAO) values as a result of hydrodynamic damping generated by relative motion - this is true for both regular and irregular wave situations. In this case, the average magnitude of RAOs computed from irregular waves and that computed from regular waves are of the same order. This type of nonlinearity, however, does not noticeably deform the response probability distribution in irregular waves. (See sections 6.3, 7.3.1 and 7.4.1.)
- When drag and structural nonlinearities are important, the trend of RAO variations in the investigated cases is to increase with increasing input level in both the regular and irregular waves; this dependency is attributable to two factors: (1) the structure's stiffness decreases with increasing loading level because of structural nonlinearities and (2) the drag excitation increases quadratically with increasing wave heights. Another consequence of the drag plus structural nonlinearities is that RAOs in irregular waves are generally lower than in comparable regular waves. Additionally, existence of drag apparently stretches the response distribution - the response distribution contains larger extremes than does the water surface elevation. (See sections 6.3, 7.3.2 and 7.4.2.)
- An extra parenthetic observation is that a linear-looking overall response (a sinusoidal output resulting from a sinusoidal input, for example) does not necessarily mean that the system is linear; a linear-looking overall system can contain significant internal nonlinearities. (See section 7.3.)

8.2 COMPUTER SIMULATIONS

NOSDA is a multiple degree of freedom, nonlinear, dynamic, time domain analysis program for offshore structures. It allows the accurate representation of the nonlinear phenomena involved in jack-up behavior. Application of this software to simulate the dynamic behavior of the models tested in both regular and irregular waves resulted in a satisfactory comparison with the measurements. This validates the computational schematizations and confirms the applicability of *NOSDA*.

The computational effort for *NOSDA* simulations of the models tested is acceptable for research purposes. The ratio between the computer time and the physical time is about 1:1 with regular wave simulations and 8:1 with irregular wave simulations using a DECstation 3100 computer. Such an approach is expected to be still inefficient for routine prototype design practice, however. Even so, the availability of a more precise, verified, dependable and commonly accepted computational model will make it possible to properly and conveniently evaluate less exact but more efficient routine design procedures. The overall purpose of this total project is to develop, document and verify this computational model. Further research can focus on reduction of the number of degrees of freedom and thus computational intensity.

Some other salient results found in the computer simulations are recapitulated as follows:

- Structure compliance should be included in the hydrodynamic force determination. Relative velocity, instead of absolute water particle velocity, is required for simulating the behavior of a jack-up structure. This allows the straightforward modeling of hydrodynamic damping. Near resonance this (extra) damping level is important even though the contribution of the structural velocity to the computation of the hydrodynamic force might otherwise be of minor importance. Drag, when acting on a flexible structure, then remains important even under low *KC* Number conditions. (See section 6.5.1.)
- Linear wave theory is sufficient for predicting the wave kinematics with the low wave cases investigated; using linear wave theory or Stokes' 2nd Order Wave Theory makes negligible difference, here. (See sections 5.2 and 6.5.5.)
- Numerical investigation using *NOSDA* shows that identical overall dynamic responses over a wide range of frequencies can be obtained from models which differ only in the damping and stiffness values at the deck-leg connection. Such models have quite different static properties, however. (See sections 6.2.2.3 and 6.5.6.)
- Effects of weight eccentricity (P-δ) cannot responsibly be neglected. This effect can be well simulated in the NOSDA software. (See sections 6.2.2.4 and 6.5.7.)

Notation and symbols

The most common symbols used in this dissertation are listed in this section. International standards of notation have been used where available except for occasional uses where a direct conflict of meaning would result. Certain symbols have more than one meaning, however. This is only allowed when the local context of a symbol used is sufficient to define its meaning explicitly.

The numbers in the right hand of this table indicate the sections where the corresponding symbol first appears in this dissertation.

ROMAN LETTERS

A	cross section area	V.2.2
$\hat{A}_i$	average response amplitude at cycle i	II.1
B	displacement-strain relation matrix or kinematic matrix	V.1
B_e	resolution bandwidth	7.5
B_g	generalized kinematic matrix	IV.4
$b[\tilde{\phi}]$	bias error of the estimate $\tilde{\phi}$	IX.1
C	structural damping matrix	V.1
C_d	drag coefficient	6.2.1.2
C_m	inertia coefficient	6.2.1.2
D	outer diameter of leg	6.2.1.2
D_g	generalized constitutive relation	IV.4
D_e	constitutive relation	V.1
d	water depth	3.1
E	elastic modulus	3.1
$E[\tilde{\phi}]$	expected value of estimate $\tilde{\phi}$	IX.1
EI	leg bending stiffness	3.1
F	structural load vector	V.1
F_{Ax}	x component force at leg A	3.1
F_{Ay}	y component force at leg A	3.1

F_{Az}	z component force at leg A	3.1
F_{Bx}	x component force at leg B	3.1
F_{By}	y component force at leg B	3.1
F_{Bz}	z component force at leg B	3.1
F_{Cx}	x component force at leg C	3.1
F_{Cy}	y component force at leg C	3.1
F_{Cz}	z component force at leg C	3.1
F_{max}	maximum hydrodynamic wave force on a cylinder	IV.1
F_{min}	minimum hydrodynamic wave force on a cylinder	IV.1
f	cyclical frequency	3.2
f_n	primary natural frequency of structure	3.1
f_p	peak wave frequency	3.2
f^+	local wave load causing maximum total load	IV.1
f^-	local wave load causing minimum total load	IV.1
G_{xx}	autospectral density function (one-sided)	3.3
G_{xy}	cross-spectral density function (one-sided)	IX.3
g	acceleration due to gravity	3.1
H	wave height	3.2
H_r	comparable wave height	7.4.1
H_s	significant wave height	3.2
H_{xy}	frequency response function	IX.3
$\lvert H_{xy} \rvert$	gain factor	IX.3
I	moment of inertia	3.1
K	structural stiffness matrix	V.1
KC	Keulegan-Carpenter parameter	6.3
K_d	structural lateral stiffness from dynamic tests	4.2.2
K_i	incremental stiffness	I
K_{lb}	leg theoretical pure bending stiffness	II.2
K_{mb}	model theoretical pure bending stiffness	II.2
K_s	structural stiffness obtained from static tests	4.1
K_t	theoretical structural stiffness	4.2.2
k	spring coefficient	V.2.2
	wave number	IV.1
L	leg length	II.2

L_d	leg spacing	V.3.1
l	element length	IV.4
$\boldsymbol{M}$	structural mass (or inertia) matrix	V.1
M_{eq}	structural equivalent mass	II.2
m_i	ith moment of spectrum	7.4
$\boldsymbol{N}$	interpolation function matrix	V.1
N_r	number of data points in total record	VIII.1
N_s	number of data points in record segment	VIII.3
n	decrement coefficient	II.3
n_d	number of segments	VIII.1
n_e	equivalent number of segments	VIII.2
P	vertical force	IV.4
$P(x)$	(cumulative) probability distribution function	IX.2
P_e	Euler critical load	II.2
$p(x)$	probability density function	IX.2
Re	Reynolds number	6.2.1.2
r	viscous damping coefficient	4.2.3
r_c	critical damping coefficient	4.2.3
r'	viscous damping coefficient per unit length	V.1
$s.d.[\tilde{\phi}]$	standard deviation of $\tilde{\phi}$	IX.3
T	wave period	6.2.1.2
T_m	free vibration response period	II.1
T_n	structural natural frequency	4.2.1
T_r	total record length	VIII.1
T_s	segment length	7.5
t	time	V.1
	thickness	V.2.1
u	water particle horizontal velocity	IV.1
$\boldsymbol{u}$	nodal displacement vector	V.1
u_A	x direction deck displacement at location A	3.1
u_C	x direction deck displacement at location C	3.1
u_c	displacement field	V.1
$\ddot{u}_D$	x direction deck acceleration at location D	3.1
$\hat{u}$	amplitude of water particle horizontal velocity	6.2.1.2

$Var[\tilde{\phi}]$	variance of the estimate $\tilde{\phi}$	IX.1
v_A	y direction deck displacement at location A	3.1
v_C	y direction deck displacement at location C	3.1
$\ddot{v}_D$	y direction deck acceleration at location D	3.1
W	window width	IX.2
W_{eq}	structural equivalent weight for the P-δ effect	II.2
w_i	window function	VIII.3
X	structural displacement vector	V.1
x	coordinate direction	3.1
y	coordinate direction	3.1
z	vertical coordinate direction	3.1

GREEK LETTERS

α	coefficient	VII
	level of significance	IX.4
γ	integration parameter	VI.1
γ^2_{xy}	coherence function	IX.3
Δ	increment	I
δ	horizontal eccentricity	1.3
	log decrement	II.3
ε	normalized root mean square error	IX.1
$\boldsymbol{\varepsilon}$	strain vector	V.1
ε_b	normalized bias error	IX.1
$\boldsymbol{\varepsilon}_g$	generalized strain vector	V.1
ε_m	spectral width parameter	7.4
ε_r	normalized random error	3.3
ζ	coefficient	IV.4
η_A	instantaneous wave surface elevation at location A	3.1
θ	rotational angle	V.2.2
θ_{xy}	phase factor	IX.3
λ	wave length	III.1

ν	fluid viscosity	6.2.1.2
	degrees of freedom for statistical distribution	VIII.1
ν_e	equivalent degrees of freedom for statistical distribution	VIII.2
ξ	structural damping ratio	4.2.3
π	3.1415926536	II.2
ρ	leg mass density	V.2.1
ρ_w	water density	V.2.1
ρ'	leg mass density per unit length	V.1
σ	standard deviation	IX.1
$\boldsymbol{\sigma}$	stress vector	V.1
$\boldsymbol{\sigma}_g$	generalized stress vector	V.1
τ_1	time delay	IX.3
ϕ	arbitrary statistical parameter	IX.1
$\bar{\phi}$	an estimate of the quantity ϕ	IX.1
ω_n	circular natural frequency	II.3

ACRONYMS

DAS	data acquisition system	7.2.2
DEM	discrete element method	6.2.2
DOF	degree of freedom	6.2.2
FFT	fast Fourier transform	7.2.3
IR	instrumentation recorder	3.2
MPM	most probable maximum	7.1
RAO	response-amplitude-operator	3.3
rms	root mean square	7.1
SWL	still waver level	5.2
UV	ultraviolet light	3.2

References

(Anon.) 1981-1983. Dynamics of Jack-up Platforms - A Joint Industry Project, Part Reports 1-4 and Final Report, Det Norske Veritas, Oslo, Norway.

(Anon.) 1983. Wave Kinematics in Irregular Waves, MaTS Program Report, M1628 /MaTS VM-I-4, Delft Hydraulics Laboratory, April.

(Anon.) 1989. Practice for the Site-Specific Assessment of Jack-Up Units, Shell International Petroleum Maatschappij, The Hague, May.

(Anon.) 1990. Guideline for Site Specific Assessment of Mobile Jack-Up Units, the Working Group of the Joint Industry Sponsored Project "Jack-Up Site Assessment Procedures and Establishment of an International Technical Guideline", June.

(Anon.) 1991. Jack-Up Site Assessment Guided onto Common Ground, Offshore Engineer, January.

Battjes, J.A. and van Heteren,J., 1983. Measurements of Wind Wave Kinematics, Report WWKZ-G007, Rijkswaterstaat, The Netherlands.

Bea, R.G. and Lai, N.W., 1978. Hydrodynamic Loadings on Offshore Platforms, Paper 3064, Offshore Technology Conference, Houston, Texas, May.

Bearman, P.W., 1988. Wave Loading Experiments on Circular Cylinders at Large Scale, BOSS '88, Trondheim, Norway.

Bendat, J.S. and Piersol, A.G., 1971. *Random Data: Analysis and Measurement Procedures*, Willey-Intersience, New York.

Bendat, J.S. and Piersol, A.G., 1986. *Random Data: Analysis and Measurement Procedures (2nd Edition)*, Willey-Intersience, New York.

Bendat, J.S., 1990. *Nonlinear System Analysis & Identification from Random Data*, Willey-Intersience, New York.

Blaauwendraad, J. and Kok, A.W.M., 1987. Numerical Techniques for Engineering Analysis and Design, NUMETA 87 Conference, Swansea, U.K.

Blaauwendraad, J., 1989. TILLY, Introduction Manual, Research Report, Faculty of Civil Engineering, Delft University of Technology. (in Dutch).

Borgman, L.E., Allender, J., Krogstad, H., Barstow, S. and Audunson, T., 1989. Conditional Simulation of Ocean Wave Kinematics and Comparisons with Storm Field Measurements, NATO Advanced Research Workshop, Molde, Norway, May.

Brekke, J.N., Murff, J.D., Campbell, R.B and Lamb, W.C., 1989. Calibration of Jackup Leg Foundation Model Using Full-Scale Structural Measurements, Paper 6127, Offshore Technology Conference, Houston, Texas, May.

Brekke, J.N., Campbell, R.B., Lamb, W.C. and Murff, J.D., 1990. Calibration of Jackup Structural Analysis Procedure Using Field Measurements from A North Sea Jackup, Paper 6465, Offshore Technology Conference, Houston, Texas, May.

Burrows, R., 1979. Probabilistic Description of the Response of Offshore Structures to Random Wave Loading, *Mechanics of Wave-Induced Forces on Cylinders*, Pitman, San Francisco.

Carlsen, C.A., Kjeoy, H. and Eriksson, K., 1986. Structural Behavior of Harsh Environment Jack-ups, *The Jack-up Drilling Platform - Design and Operation*, Collins, London.

Carter, G.C., Knapp, C.H. and Nuttall, A.H., 1973. Estimation of the Magnitude-Squared Coherence via Overlapped Fast Fourier Transfer Processing, IEEE Transactions on Audio and Electroacoustics, Vol. AU-21, P337, Institute of Electral and Electronics Engineering, August

Chakrabarti, S.K., 1971. Dynamics of single point mooring in Deep Water (Discussion), *Journal of Waterway, Port and Coastal Division*, Vol. 97, American Society of Civil Engineers, August.

Chakrabarti, S.K., 1980. Laboratory Generated Waves and Wave Theories, *Journal of Waterway, Port and Ocean Division*, Vol. 106, American Society of Civil Engineers, August.

Chakrabarti, S.K., 1982. Wave Force Coefficients for Rough Vertical Cylinders, *Journal of Waterway, Port, Coastal and Ocean Division*, American Society of Civil Engineers, November.

Chakrabarti, S.K., 1986. *Hydrodynamics of Offshore Structures*, Springer Verlag, Computational Mechanics Publications, Southampton, Boston.

Chiba, S., Onuki, T. and Sao, K., 1986. Static and Dynamic Measurement of Bottom Fixity, *The Jack-up Drilling Platform - Design and Operation*, Collins, London.

Dean, R.G., 1968. Relative Validity of Water Wave Theories, Proc. on Civil Engineering in Ocean, American Society of Civil Engineers, San Francisco.

Dean, R.G. and LeMehaute, B., 1970. Experimental Validity of Water Wave Theories Structural Engineering Conference, American Society of Civil Engineers, Portland, Oregon.

Forristall, G.Z., 1981. Kinematics of Directionally Spread Waves, the Conference on Directional Wave Spectra Applications, American Society of Civil Engineers, Berkeley, California, September.

Gründlehner, G.J., 1989. Simple Analytical Jack-Up Leg - Hull Connection Model, Report P 8525-1428, Faculty of Mechanical Engineering and Marine Technology, Workgroup Offshore Technology, Delft University of Technology, March.

Gründlehner, G.J., 1989. A Simple Model for Jack-Up Leg - Hull Deformation Behavior, Report PF 8525-1470, Faculty of Mechanical Engineering and Marine Technology, Workgroup Offshore Technology, Delft University of Technology, August.

Gudmestad, O.T., 1990. A New approach for Estimating Irregular Deep Water Wave Kinematics, *Applied Ocean Research*, Vol. 12, No. 1.

Holtrop, E.F., 1989. Model Testing of Spudcan Behavior Under Decreasing Vertical Load, Report 313, Geotechnical Lab, Faculty of Civil Engineering, Workgroup Offshore Technology, Delft University of Technology, July.

Jenkins, G.M and Watts, D.M., 1968. *Spectral Analysis and its Applications*, Holden-Day, San Francisco.

Journée, J.M.J., Massie, W.W., Boon, B. and Onnink, R., 1988. Model Experiments on Jack-Up Platform Hydrodynamics, Report no. 809: Ship Hydromechanics Lab, Faculty of Mechanical Engineering and Marine Technology, Workgroup Offshore Technology, Delft University of Technology, November.

Klaver, J.P., 1990. The effect of Footing Length on Footing Bearing Capacity, Geotechnical Lab, Faculty of Civil Engineering, Workgroup Offshore Technology, Delft University of Technology, April.

Lagers, G.H.G, 1990. Morison Coefficients of Jack-up legs, MSC ref SP 8603-1505, Marine Structure Consultants (MSC) bv, February.

Leijten, S.F., Efthymiou M., 1989. A Philosophy for the Integrity Assessment of Jack-Up Units, Paper 19236, Society of Petroleum Engineers.

Liu, P. and Massie, W.W., 1988. NOSDA - Nonlinear Dynamic Analysis Program for Offshore Structures, Research Report, Faculty of Civil Engineering, Workgroup Offshore Technology, Delft University of Technology, December.

Liu, P., 1989. Elevated Jack-Up Platform Analysis Methods, Research Report, Faculty of Civil Engineering, Workgroup Offshore Technology, Delft University of Technology, May.

Liu, P., 1989. Nonlinear Dynamic Simulation of Jack-Up Platform Models, Research Report, Faculty of Civil Engineering, Workgroup Offshore Technology, Delft University of Technology, November.

Liu, P., Massie, W.W., Wolters, J.G. and Blaauwendraad, J., 1990. Nonlinear Simulation of Jack-Up Platform Models, Paper 6470, Offshore Technology Conference, Houston, Texas, May.

Liu, P., 1991. Dynamic Response of Jack-Up Models to Irregular Waves, Research Report, Faculty of Civil Engineering, Workgroup Offshore Technology, Delft University of Technology, January.

Liu, P., Massie, W.W., Wolters, J.G. and Blaauwendraad, J., 1991. Response of Jack-Up Platform Models to Irregular Waves, Paper 6591, Offshore Technology Conference, Houston, Texas, May.

Massie, W.W., Liu, P. and Boon, B., 1989. Elevated Jack-Up Platform Durability - A Problem Survey, Workgroup Offshore Technology, Delft University of Technology, October.

Massie, W.W and Liu, P., 1990. The Jack-Up Durability Problem, Paper 20911, EUROPEC 90 Conference, Society of Petroleum Engineers, The Hague, October.

Massie, W.W, Liu, P. and Zeelendberg, L., 1991. Jack-Up Leg Hydrodynamic Interaction Schematization, Paper 6592, Offshore Technology Conference, Houston, Texas, May.

Michels, O.E.A., 1990. Stress Analysis in Jack-Up Leg to Hull Connections, Faculty of Civil Engineering, Workgroup Offshore Technology, Delft University of Technology, May.

Pierson, W.J. and Holmes, P., 1965. Irregular Wave Forces on a Pile, *Journal of Waterway & Harbor Division*, Vol. 91, American Society of Civil Engineers.

Press, W.H., Flannery, B.P., Teukolsky, S.A., and Vetterling, W.T., 1986. *Numerical recipes (the Arts of Scientific Computing)*, Cambridge University Press, Printed in the USA.

Rienecker, M.N. and Fenton, J.D., 1981. A Fourier Approximation Method for Steady Water Waves, *Journal of Fluid Mechanics*, Vol. 104.

Rodenbush, G. and Forristall, G.Z., 1986. An Empirical Model for Random Directional Wave Kinematics Near the Free Surface, Paper 5097, Offshore Technology Conference, Houston, Texas, May.

Sliggers, P.G.F., 1991. SIMP Practice for Site Specific Structural Fitness for Purpose Assessment of Jack-Up Rigs, Paper 21979, IADC, Society of Petroleum Engineers.

Sobey,, R.J., 1989. Wave Theory Predictions of Crest Kinematics, NATO Advanced Research Workshop, Molde, Norway, May.

Spaargaren, P.J., 1988. Hydrodynamic Force Cancellation, Faculty of Civil Engineering, Workgroup Offshore Technology, Delft University of Technology, April.

Spaargaren, P.J., 1989. Spudcan Modeling for Jack-Up Dynamics, Faculty of Civil Engineering, Workgroup Offshore Technology, Delft University of Technology, September.

Spaarman, R., 1989. Verwerking, Analyse en Evaluatie van Hydrodynamische Model-experimenten met een Jack-up, Faculty of Mechanical Engineering and Marine Technology, Workgroup Offshore Technology, Delft University of Technology, March.

Steele, K.M., Finn, L.D., and Lambrakos, K.F., 1988. Compliant Tower Response Prediction Procedures, Paper 5783, Offshore Technology Conference, Houston, Texas, May.

Stuit, H.G., 1989. Spud-can Limit Loads in Sand under Decreasing Vertical Loads, Geotechnical Lab, Faculty of Civil Engineering, Workgroup Offshore Technology, Delft University of Technology, May.

Tucker, M.J., Challenor, P.G. and Carter, D.J.T., 1984. Numerical Simulation of a Random Sea, a Common Error and its Effect upon Wave Group Statistics, *Applied Ocean Research*, Vol. 6, No. 2.

Vugts, J.H. and Bouquet, A.G., 1985. A Nonlinear Frequency Domain Description of Wave Forces on an Element of Vertical Pile in Random Sea, *Behaviour of Offshore Structures*, Elsevier Science Publishers, Amsterdam.

Wheeler, J.D., 1970. Method for Calculating Forces Produced by Irregular Waves, *Journal of Petroleum Technology*, March.

Yuen, H.C. and Lake, B.M., 1982. Nonlinear Dynamics of Deep-Water Gravity Waves, *Advances in Applied Mechanics*, Vol. 22.

Zeelenberg, B. L., 1990. Schematization of Hydrodynamic Interaction of Jack-Up Legs, Faculty of Civil Engineering, Workgroup Offshore Technology, Delft University of Technology, June.

Zeelenberg, B. L., 1990. Morison Coefficients for Jack-Up Legs, Faculty of Civil Engineering, Workgroup Offshore Technology, Delft University of Technology, July.

Zhang, J., Randall, R.E. and Spell, C.A., 1991. On Wave Kinematics Approximate Methods, Paper 6522, Offshore Technology Conference, Houston, Texas, May.

Summary

The present work was carried out as a part of a project with objective to increase the detailed knowledge of the behavior of jack-up platform components as well as the prediction of the overall structure's elevated behavior and (remaining) lifetime.
The need for such a study is demonstrated by the relatively high rate of structural failure for jack-up rigs as compared to fixed platforms and the considerable discrepancy existing among various industry assessment methods and criteria for elevated jack-up platforms.

The work presented in this dissertation concentrates on the investigation of the influence of hydrodynamic and structural nonlinearities on the dynamic behavior of elevated jack-up rigs. The work involves the following three aspects:

- Software Development
  Two software packages have been developed during the prosecution of the investigation: (1) *NOSDA* simulation software for the *N*onlinear *O*ffshore *S*tructure *D*ynamic *A*nalysis; (2) *RANDA* software for *RAN*dom *D*ata *A*nalysis.
- Physical Model Tests
  The experimental studies of three principle jack-up models were carried out in a wave tank of the Hydromechanics Laboratory of the Faculty of the Mechanical Engineering and Marine Technology, TU Delft. The model testing program included exposing the models to regular and irregular uni-directional, long crested waves as well as static and free vibration tests.
- Experimental Result Analysis and Computer Simulations
  The processing of the measured data from the irregular wave tests was carried out using *RANDA* software and supported by a careful error analysis. The model behavior in regular and irregular waves was simulated using *NOSDA* software.

The experimental results and associate computer simulations demonstrate that:

- Hydrodynamic forces include an important quadratic drag element. Relative motions from structural compliance are such that they cannot be neglected in the hydrodynamic computation.
- The stiffness obtained from static tests can be significantly lower than that inferred from dynamic vibration tests; this discrepancy has been observed both in the field (by others) and in the present lab models. This apparent stiffness enhancement in the present testing is caused by the large local damping at the deck-leg connection.

- Inclusion of the P-δ effect in the structural schematization is essential for the jack-up simulations. This effect can be well modeled with the *NOSDA* software.

Nonlinearities are important even with the present simplified model testing and different nonlinearities have different (sometimes compensating) influences on the structure's dynamic behavior. Therefore, the scientifically responsible type of computer model for jack-up analysis must be capable of reproducing a wide range of nonlinear, dynamic phenomena. Use of a nonlinear, dynamic, stochastic computer model based upon a discrete element schematization and working in the time domain has proven to be a success for simulating the dynamic behavior of the models tested. While the computational effort of such an approach is acceptable for the present models, further improvements in the computational efficiency are needed for its application to routine prototype design practice. In spite of this, the availability of a more precise, verified and dependable computational model is essential as a tool with which to concisely check the performance of more approximate, efficient routine design procedures.

SAMENVATTING

Het werk voor dit proefschrift is uitgevoerd als een deel van een jack-up project. Het doel van dit project is het vergroten van de gedetailleerde kennis van het gedrag van afzonderlijke componenten van hefeilanden alsook het voorspellen van het gedrag en de (rest)levensduur van de gehele constructie in geheven toestand.
Het relatief grote aantal gevallen van schade aan hefeilanden in vergelijking met dat aan vaste platforms, en de discrepantie tussen de resultaten van de gebruikelijke beoordelingsmethoden en criteria tonen de noodzaak van deze studie aan.

Het werk is geconcentreerd op het onderzoek van niet-lineariteiten in het domein van de hydrodynamica en het gedrag van de constructie van hefeilanden.
Het werk omvat de volgende drie aspecten:

- Het ontwikkelingen van rekenprogrammatuur
  Twee software-paketten zijn ontwikkeld tijdens de uitvoering van het onderzoek: (1) simulatie programma *NOSDA* voor de *N*iet-lineaire *O*ffshore *S*tructurele *D*ynamische *A*nalyse; (2) programma *RANDA* voor *RAN*dom *D*ata *A*nalyse.
- Het testen van fysische modellen
  In het laboratorium van de Faculteit der Werktuigbouwkunde en Maritieme Techniek van de TU Delft zijn drie hefeiland-modellen in de golftank getest. Het testprogramma bevatte zowel onderzoek van de modellen in regelmatige en in onregelmatige uni-directioneële, langkammige golven, als statische en vrijetrillingstesten van de modellen.
- De analyse en computersimulaties van experimentele resultaten
  De verwerking van de gemeten data van proeven in onregelmatige golven werd ondersteund met een zorgvuldige foutenanalyse met behulp van het programma *RANDA*. Modelgedrag in regelmatige en onregelmatige golven is gesimuleerd met het programma *NOSDA*.

De experimentele resultaten en bijbehorende computersimulaties tonen aan:

- Hydrodynamische krachten bevatten een belangrijk kwadratisch drag element. Bewegingen van de constructie mogen niet verwaarloosd worden in de hydrodynamische berekeningen.

- De stijfheid verkregen uit statische testen kan significant lager zijn dan de stijfheid afgeleid uit dynamische vibratie proeven; dit verschil is opgemerkt zowel in de praktijk (door anderen) als in de gebruikte laboratorium modellen. De hogere stijfheid gevonden in de hier uitgevoerde dynamische proeven wordt veroorzaakt door de grote lokale demping in de dek-poot-verbinding.
- Het opnemen van het P-δ effect in het model is essentieel voor de hefeiland-simulatie. Het effect kan goed gemodelleerd worden met het programma *NOSDA*.

Zelfs in de vereenvoudigde modellen, die gebruikt zijn, spelen niet-lineariteiten in gedrag een belangrijke rol. Verschillende niet-lineariteiten hebben verschillende - soms tegengestelde - effecten op het dynamische gedrag van de constructie. Computermodellen moeten daarom in staat zijn om een breed scala van niet-lineaire dynamische verschijnselen te reproduceren. Het gebruik van een niet-lineair, dynamisch, stochastisch en in het tijdsdomein werkend computermodel, gebaseerd op een schematisatie van discrete elementen, is succesvol gebleken voor de simulatie van het dynamische gedrag van de geteste modellen. De benodigde rekentijd voor een dergelijke benadering is aanvaardbaar voor de gebruikte modellen, maar de snelheid van het programma moet worden vergroot om toepassing in de routine-ontwerppraktijk aantrekkelijk to maken. Niettemin is nu reeds een nauwkeurig, geverifieerd en betrouwbaar computermodel een essentieel hulpmiddel om te beoordelen wat meer benaderende, efficiënte routine ontwerpprocedures waard zijn.

Acknowledgement

Help from many people has made the present work possible. The research included in this dissertation was carried out in the Workgroup Offshore Technology of the Delft University of Technology, under the supervision of Prof. J. G. Wolters and Prof. J. Blaauwendraad. The direct guidance came from Mr. W. W. Massie. These three persons are from the Faculty of Civil Engineering. Their sustained help and encouragement are the source of the inspiration and driving force for this work.

The author is grateful to other members of his steering committee: Prof. B. Boon, Prof. M. van Holst, Prof. J.A. Pinkster (from the Faculty of Mechanical Engineering and Marine Technology), Mr. G.H.G. Lagers from Marine Structure Consultants, Mr. P.G.F. Sliggers from Shell International Petroleum Maatschappij and Mr. W.J. van Tiggelhoven from Neddrill. Their valuable support and constructive suggestions have not only greatly improved the quality of the present work, but also enriched the author's knowledge on structural dynamics, hydrodynamics, offshore engineering and, in particular, insight into the jack-up durability problem.

The stimulation from Prof. Du Qing-hua and especially Prof. Zheng Zhao-chang, the author's supervisors at Tsinghua University in Beijing, is gratefully acknowledged.

The author is also indebted to the colleagues in the Hydromechanics Laboratory of the Faculty of Mechanical Engineering and Marine Technology where the three jack-up models were tested and the colleagues in the Fluid Mechanics Laboratory of the Faculty of Civil Engineering where the analog data were digitized.

The author wishes to thank the Dutch Technology Foundation (STW) for their financial support for this study.

Last but not least, the author's gratitude goes to all colleagues in the Department of Hydraulics within the Faculty of Civil Engineering, TU Delft and many other friends in this country. It is their hospitality and warmth that create the pleasant environment in which I happily finished this work.

Appendix I Static test results

The static tests were carried out for each model by exerting static, horizontal loads at the deck level and recording the corresponding displacements. The results are plotted in figures I.1 through I.3. Note that the static test with Model I was carried out before its deck-leg connections were modified.

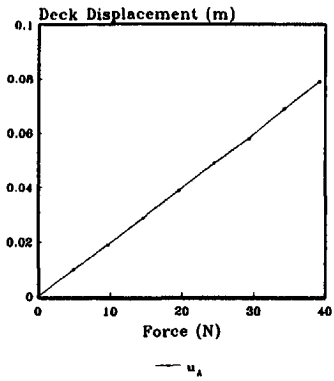

Figure I.1 Measured Overall Static Constitutive Relation (Model I)

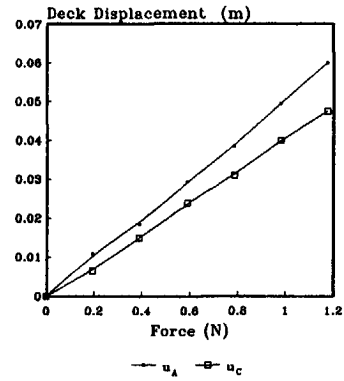

Figure I.2 Measured Overall Static Constitutive Relation (Model II)

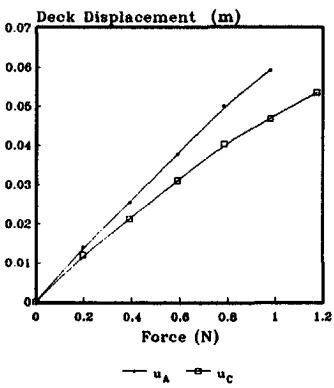

Figure I.3 Measured Overall Static Constitutive Relation (Model II-M)

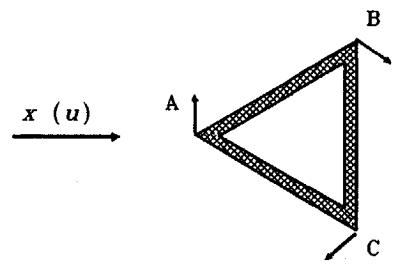

Figure I.4 Deck Displacement Caused by Rotation

In these figures u_A is the displacement in the x direction recorded at location A and u_C at location C - see figure I.4.

In the plots it can be seen that with Models II and II-M u_A deviates from u_C (With Model I only u_A was measured.) Since the deck frame is stiff enough to be considered as a rigid body, the differences between u_A and u_C are caused by the deck rotations due to load asymmetries, leg stiffness differences and/or connection stiffness differences. u_A is used to calculate the global stiffness so that the effect of rotation is avoided - see figure I.4.

The incremental global lateral stiffness is computed by:

$$K_i = \frac{\Delta F}{\Delta u_A} \tag{I.1}$$

The results for all three models are given in table I.1:

Table I.1 Global Horizontal Stiffness at Deck Level

Model I			Model II			Model II-M		
F (N)	u_A (m)	K_i (N/m)	F (N)	u_A (m)	K_i (N/m)	F (N)	u_A (m)	K_i (N/m)
0.0	0.000		0.000	0.000		0.000	0.0000	
4.9	0.010	490.00	0.195	0.0108	18.06	0.195	0.0140	13.93
9.8	0.019	544,40	0.390	0.0185	25.32	0.390	0.0255	16.96
14.7	0.029	490.00	0.590	0.0293	18.52	0.590	0.0378	16.26
19.6	0.039	490.00	0.785	0.0385	21.20	0.785	0.0500	15.98
24.5	0.049	490.00	0.980	0.0495	17.73	0.980	0.0593	20.97
29.4	0.058	544.00	1.175	0.0600	18.57			
Average		508.00	Average		19.90	Average		16.82

It can be seen that the incremental stiffnesses fluctuate at different load levels. It is hard to find a consistent relation that follows the changes. Possible explanations for the fluctuations are: (1) equipment errors and (2) structural nonlinearities such as the nonlinear connections at both upper and lower ends, etc.

At the beginning of the loading paths, the incremental stiffnesses for all three models are systematically lower; this might be caused by (1) free play in the connections of both ends and/or (2) structural dry friction which keeps the structures away from their true equilibrium positions.

The only difference between Model II and Model II-M is the deck mass and therefore P-δ effect. The P-δ effect reduces overall structural stiffness; this is confirmed by the lower average stiffness for Model II-M in the above table.

The average global horizontal stiffness of the model is considered to be its representative 'static' stiffness.

Appendix II Free vibration test results

II.1 NATURAL PERIOD

When testing Model I standing in air, an unexpected significant decrease of response period, T_m, with succeeding vibration cycles (in fact with decreasing response levels) was found - see figure II.1 and the table derived from it.

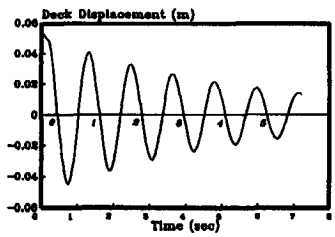

Cycle	T_m (sec)
0-1	1.26
1-2	1.22
2-3	1.14
3-4	1.09
4-5	1.06
Average	1.16

Figure II.1 Free Vibration Response Record

There are at least three factors which can influence the response period:

1. *P-δ* Effect
   A lateral displacement results in an additional second order moment. This leads to a relatively smaller horizontal restoring force of the structure (smaller virtual stiffness) and in turn yields a longer response period.
2. Damping
   The natural period, T_n, is expressed as:

$$T_n = T_m \sqrt{1 - \xi^2} \qquad \text{(II.1)}$$

   where T_m is the free vibration response period and ξ the damping ratio. This influence is of minor importance, however. Even when ξ is as high as 20%, the difference is within 2% - $\sqrt{(1 - \xi^2)}$ = 0.98; the free vibration response period can be used directly as the natural period.
3. Deck-leg and bottom-leg connections

Comparing these three possible causes, it is most likely that the scatter of the response period data stemmed from the bad leg-deck connections. A sketch of these connections is given in figure II.2.

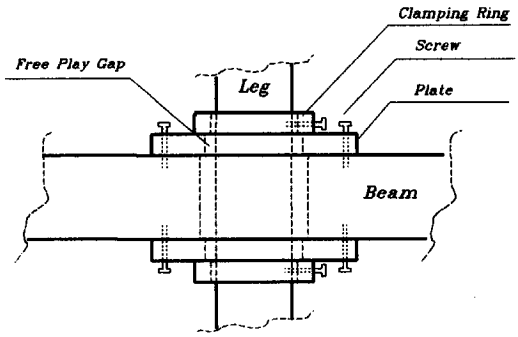

Figure II.2 Deck-leg Connection Detail

It is designed to be a perfectly clamped joint with infinite stiffness. The deck members are connected by two parallel plates. Two parallel clamping rings screwed to the leg outside the plates provide fixity. A more realistic process of connection deformation with increasing load might be:

1. The connection remains undeformed in the horizontal direction due to the Coulomb friction between the clamping rings and plates until the loading exceeds the critical static friction; meanwhile the clamping rings impose a pair of vertical (normal) forces on the upper and lower plates respectively due to the bending moment. Since the plates are relatively weak in terms of bending stiffness, a significant deformation can occur now and throughout the following loading phases; this can yield a much more flexible connection than the originally intended rigid clamping.
2. The rings start to slide (relative to the plates) so that the leg undergoes a free play till the leg touches the edges of the deck connecting plate holes.
3. The connection deformation follows the elastic rule.
4. It enters a plastic phase when the local leg and/or plate yielding stress is exceeded.

Note that since the contact area is relatively small, local plasticity is expected to be reached easily. The constitutive curve of the whole process described above is summarized in figure II.3.

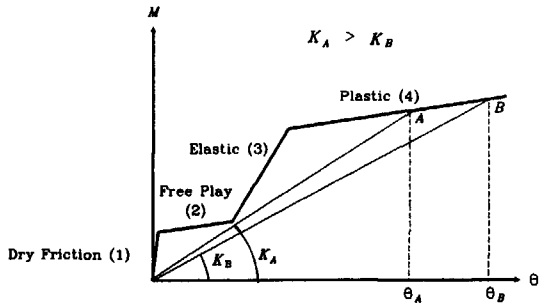

Figure II.3 Possible Deck-leg Connection Constitutive Relation

It can be seen that beyond a certain loading level, a larger displacement corresponds to a lower resulting overall stiffness and thus a higher response period; this is qualitatively in agreement with the measurements in figure II.1.

Later, the deck-leg connections of Model I were glued to improve their mechanical behavior. Since the clamping rings, the plates and the leg itself of model I are all made of PVC, the gluing was effective. The response period data with the glued connections are tabulated below:

Table II.1 Response Periods of Model I after Gluing

Cycle	T_m (sec)
0-1	1.04
1-2	1.03
2-3	1.015
3-4	1.00

It shows that the response periods after the gluing are much more consistent. The structural nonlinearities of the deck-leg connection has been largely eliminated.

Strictly speaking, the definition of natural period is not valid for a nonlinear system and many 'mature' techniques developed for a linear system are not applicable to a nonlinear system. However, the output of commonly encountered slightly nonlinear systems can be seen to be composed of a 'fundamental' linear part plus a nonlinear modification. The techniques normally used for linear systems can be transplanted to approximately treat a nonlinear system in a piece-wise (incremental) form or in an average sense. Using this analogy between linear and sightly nonlinear systems, the response period in

free vibration will be called the natural period and the virtual stiffness of the structure will be called simply the structural stiffness.

Models II and II-M have the same basic deck-leg connections as Model I. A worse situation could be expected now since their legs and deck are of smaller sizes. It is obvious from figure II.4 that a more severe free play can result from the same clearance with Model II-(M).

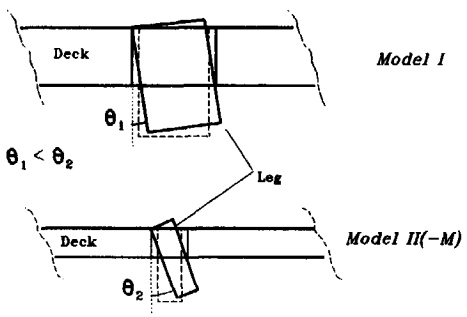

Figure II.4 Different Influences of Clearance

In order to avoid extra structural uncertainty the deck-leg connections of Model II-(M) should have been improved, too. However, the combination of materials now used (PVC clamping rings, copper legs and aluminum plates) made gluing unattractive. Therefore, during a free vibration run, different natural periods were obtained for different response cycles - in fact for different response amplitudes - just as was the case initially with Model I. These natural periods within one run were averaged to yield the 'representative' period.

When the free vibration tests with Models II and II-M were carried out, it was found that the decay was so fast that it was difficult to record the response traces. As a remedy - although not scientifically responsible - a sort of 'hand help' was used to obtain readable oscillatory response traces. These results are less accurate but are still used further (with care!).

Natural periods associated with different deck displacement amplitude, $\hat{A}$, for each of the models obtained from the free vibration tests in air are listed in table II.2.

Table II.2 Model Natural Periods

Model I		Model II		Model II-M	
$\hat{A}$ (cm)	T_n (sec)	$\hat{A}$ (cm)	T_n (sec)	$\hat{A}$ (cm)	T_n (sec)
3.7	1.04	2.15	1.38	4.1	2.44
2.7	1.03	1.55	1.09	0.8	1.83
2.0	1.015			0.4	1.52
1.5	1.00				
Average	1.02	Average	1.25	Average	1.93

This table shows that while the results with Model I are rather consistent, those with Models II and II-M are quite scattered. A general trend is that the natural periods decrease with decreasing amplitudes; this nonlinear phenomenon can be explained, as discussed above, mainly by the imperfect connections. Model II-M has longer periods; this is due to greater deck mass and the extra P-δ effect.

The natural period data for Models II and II-M should be used with caution.

II.2 MODEL STIFFNESS

There are three approaches to obtain model stiffnesses:

1. Theoretical Approach

   If the legs are completely clamped into the deck at the upper end and perfectly hinged to the bottom at the lower end, then each of the legs can be schematized as a cantilevered beam. The theoretical pure bending stiffness can be expressed for 3 legs then as:

$$K_{mb} = 3\, K_{lb}$$
$$= 3\, \frac{3EI}{L^3} \qquad \text{(II.2)}$$

where:

K_{mb} = model theoretical pure bending stiffness
K_{lb} = leg theoretical pure bending stiffness
L = leg length
EI = bending stiffness

When there is an (equivalent) deck weight, the resulting P-δ effect can be expressed to be a reduction of the pure bending stiffness approximately by:

$$K_t = K_{mb}\left(1 - \frac{W_{eq}}{P_e}\right) \qquad \text{(II.3)}$$

where:

K_t = theoretical model stiffness with the P-δ effect
W_{eq} = equivalent deck weight
P_e = Euler critical load = $3\pi^2EI/(2L)^2$ (from the slender compressional column theory)

Assuming ideal connections (clamped deck-deck connection and hinged leg-bottom connection), an analytical derivation shows that in addition to the deck weight 11/16 of the leg weight should be lumped to the deck level for the P-δ contribution - see Liu (1989). Using this result and data in table 3.1, the theoretical stiffnesses for each of the models are given in table II.3.

Table II.3 Theoretical Model Stiffnesses

Model No.	K_{mb} (N/m)	W_{eq} (N)	P_e (N)	P-δ reduction (%)	K_t (N/m)
I	1719	276.69	3152.70	8.8%	1568.1
II	104	40.02	192.90	20.7%	82.4
II-M	104	70.92	192.90	36.8%	65.8

2. Static Load Tests

The static stiffness, K_s , for each of the models has been obtained in table I.1.

3. Derivation from Free Vibration Response

By simplifying each of the jack-up models to a single degree of freedom system, the system global 'dynamic' stiffness, K_d , can be inferred from the natural period obtained in the free vibration tests:

$$K_d = M_{eq}\left(\frac{2\pi}{T_n}\right)^2 \qquad \text{(II.4)}$$

where:

M_{eq} = equivalent mass

T_n = average natural period (from table II.2)

The details for calculating equivalent mass are given by Liu (1989). It has been demonstrated that 17/35 of the leg mass should be counted in the model equivalent masses for horizontal response, assuming that the legs move in accordance with their static deflection curve. The equivalent masses in air for each of the models are tabulated in table II.4.

Table II.4 Model Equivalent Masses (in air)

Model No.	M_{eq} (kg)
I	26.81
II	3.50
II-M	6.65

The stiffnesses of the models obtained from these three approaches are compared in table II.5.

Table II.5 Stiffness Comparison

Model No.	K_t (N/m)	K_s (N/m)	K_d (N/m)	
	Theoretical	As Built	As Built	Glued
I	1568.1	508.0	786.57	1017.0
II	82.4	19.9	88.4	--
II-M	65.8	16.8	70.5	--

The inconsistency is apparent. The results in section II.1 have already shown that the models were different from their original design and therefore, the theoretical design values of the model stiffness, K_t, were not trustworthy. It should also be noted that the K_d results for Models II and II-M are no better than the natural period data upon which they are based. Nevertheless, there seem to be two tendencies worth pointing out:

1. K_d is systematically larger than K_s; this is evident with models II and II-M. This deviation indicates that the models were stiffer dynamically than statically.
   This phenomenon may possibly be explained by:
   a. Material Properties
      Metal materials tend to have a higher yield stress under a dynamic load than under a static load; this leads to a higher equivalent, resultant 'dynamic' stiffness - see figure II.5.
   b. Connection Imperfections - Locally Concentrated Damping
      As will be shown in the next section, (especially with Model II and Model II-M) a large amount of damping is (locally) concentrated in the deck-leg connections; relative movement between the deck and legs generates remarkable resistance. This resistance increases with increasing relative velocities between the deck and legs. Hence, the effect of the high damping in the connection is analogous to a fixation against dynamic loading. When the damping is high enough, the connection will behave dynamically as if it were clamped. As such, the localized high damping at the connections has a significant influence not only on the overall structural damping behavior, but also on the natural period and thus the inferred dynamic stiffness, K_d. However, this fixing mechanism only exists when the structure is experiencing a dynamic movement. If a loading is static, the structure exhibits appreciably lower stiffness.

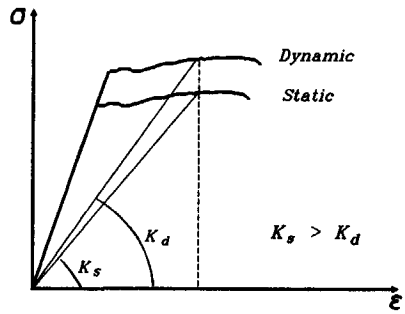

Figure II.5 Influence of Loading Rate on Yield Stress

2. With Models II and II-M the average dynamic stiffness values, K_d , seem quite in agreement with the theoretical ones, K_t . This, however, does not indicate the agreement of these models with their original designs. From the discussion in point b, above, it is clear that the calculated dynamic stiffness, K_d , generally does not represent the real structural (static) stiffness. In fact, this gives an extra supporting evidence for the assumption that the behavior of the deck-leg connection is closer to a rigid clamping under dynamic loading.

II.3 STRUCTURAL DAMPING

The models tested involve the following structural damping mechanisms:

1. Viscous Damping
   This type of damping is often found at lubricated contact surfaces; the submerged bottom hinge connection is an example of this although its contribution to the total structural damping is of minor importance.
2. Dry Friction
   This type of friction is likely to occur in the imperfect deck-leg connections where a free play gap exists in its pure form; it results in a hysteresis damping with a rectangular hysteresis loop.
3. Internal Material Damping
   Deformations of the materials of the structure itself result in energy loss via heating. Material damping is of minor influence for the structural behavior; compared with the case of Model I (whose legs are fabricated from PVC), this type

of damping is even less important with Models II and II-M (whose legs are fabricated from copper). The material damping is commonly considered to be not more than 1% of the critical damping.

4. Plastic Deformations

   Considerable plastic deformation can take place when the yield load of a member is exceeded. Generally the initial portion of the unloading curve is again elastic and not coincident with the loading curve just experienced; it results in a hysteresis curve which looks much like a parallelogram. The energy lost in the deformation will manifest itself as a type of hysteretic damping. Such plastic deformations are likely to occur in the deck-leg connections, since the contacts between the deck and legs are very local.

Viscous damping is the only linear damping mechanism; the rest involve a nonlinearity indicated by their dependency upon the response amplitude. Because of the convenience of linear viscous damping in analysis, much effort has been invested (in the literature) in the conversion of other damping mechanisms to 'equivalent' viscous forms.

With viscous damping, the relation between the log decrement, δ, and the decrement coefficient, n , is:

$$\begin{aligned} \delta &= \ln\left(A_i / A_{i+1}\right) \\ &= nT_n \end{aligned} \tag{II.5}$$

And further the overall structural damping is expressed as:

$$r = 2nM_{eq} \tag{II.6}$$

where:

r = structural equivalent viscous damping coefficient

M_{eq} = structural equivalent mass (from table 4.4)

The damping ratio between the viscous damping coefficient and critical damping coefficient, r_c (= 2 ω_n M_{eq} , where ω_n = $2\pi f_n$ is the circular natural frequency), is:

$$\xi = \frac{r}{r_c} = \frac{n}{\omega_n} = \frac{\delta}{2\pi} \tag{II.7}$$

The damping data for each of the models (in air) are given in table II.6 where $\hat{A}_i$ is the average deck response amplitude associated with cycle i. Note that the global damping values listed in this table have been calculated as if they were of the equivalent linear viscous form within one cycle. Just as for the natural period data processed in the previous section, the reliability of the damping data for Models II and II-M is questionable; the values should be used with caution. The data for model I are relatively dependable.

Table II.6 Damping Data

Model	$\hat{A}_i$ (cm)	$\hat{A}_i / \hat{A}_{i+1}$ (-)	δ (-)	T_n (sec)	n (1/s)	r (kg/s)	ξ (%)
I	2.55	1.37	0.32	1.03	0.31	16.14	5.0
	2.15	1.30	0.26	1.02	0.26	13.78	4.2
	1.25	1.27	0.24	1.00	0.24	12.82	3.8
	1.00	1.22	0.20	1.02	0.20	10.46	3.2
	Average	1.29	0.26	1.02	0.25	13.37	4.1
II	1.65	3.26	1.18	1.38	0.86	5.99	18.8
	1.10	3.78	1.33	1.09	1.22	8.54	21.2
	Average	3.52	1.26	1.25	1.04	7.27	20.0
II-M	1.6	5.00	1.61	2.44	0.69	9.15	25.6
	0.9	5.72	1.74	1.83	0.95	12.67	27.8
	0.35	3.00	1.10	1.52	0.72	9.61	17.5
	Average	3.72	1.48	1.93	0.79	10.48	23.6

The following phenomena can be observed from this table:

1. The damping ratios are surprisingly large especially for Model II and Model II-M. These values are much larger than the internal structural damping normally found. The only possible source of these high damping percentages is the imperfect deck-leg connection or also partly the leg-bottom connection (although the lower connection is designed to be a perfect hinge).

2. The damping values of the Models II and II-M show strong nonlinearity just as with the global stiffnesses; they are heavily dependent upon the structural response level. This dependence relation is, however, rather scattered. In contrast to this, the damping values of Model I are much lower and more consistent; it shows only a relatively slight decrease with decreasing response amplitude levels. This consistency is expected to result from the improved deck-leg connection.
3. The average damping coefficient of Model II-M seems slightly higher than that of Model II, although these two models are identical except for the deck weight. This deviation can possibly be attributed to extra (dry friction) damping resulting from that extra deck weight which was placed on top of the clamping rings - this increased the contact forces between the clamping rings and the deck connecting plates at the upper end as well as the contact forces in the leg bottom hinges.

Appendix III Hydrodynamic analysis theory selection

III.1 WAVE THEORY

The wave states tested are given in tables 3.2 and 3.3 for regular wave tests and irregular wave tests, respectively. The same parameters are plotted in figures III.1 through III.3 in the form of wave steepness (H/T^2) and wave depth to wave length ratio (d/T^2) to show their relationship to the region of validity for various wave theories as suggested by Dean & LeMehaute (1968 and 1970). For irregular waves, H and T are replaced by H_s and T_p to give an indicative vision on the scope where the representative waves work. Chakrabarti's experimental study results are superimposed on the figures as dots with legends - see Chakrabarti (1980) and (1986).

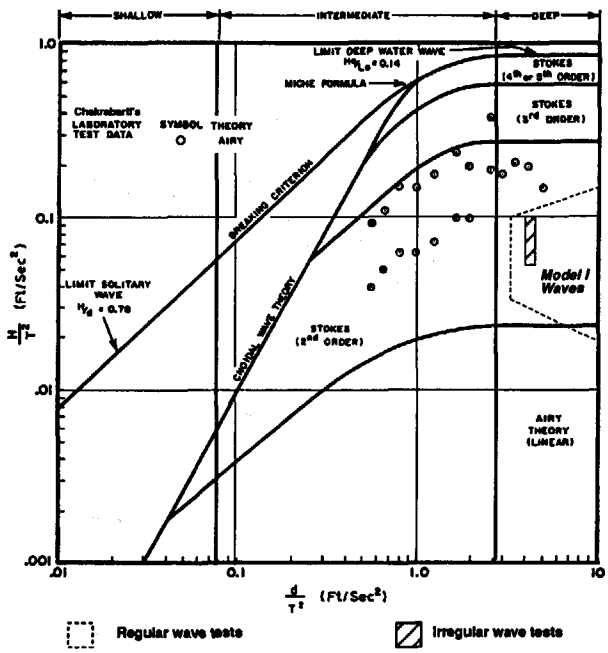

Figure III.1 Model I Waves

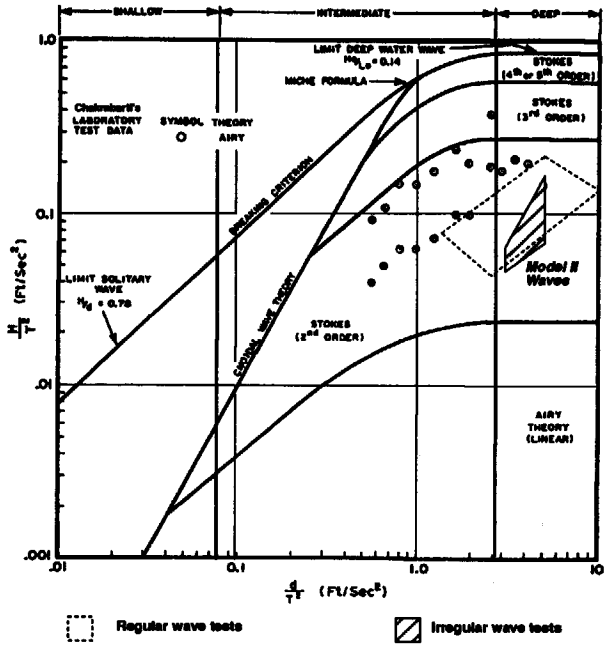

Figure III.2 Model II Waves

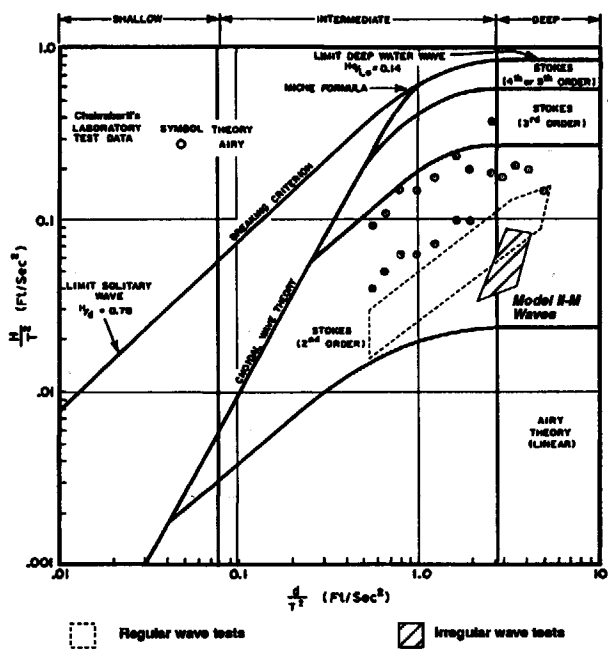

Figure III.3 Model II-M Waves

These figures show that:

a. The models were generally tested in intermediate to deep water waves.

b. According to the analytical criterion of validity, the waves for all three models are best described by the 2nd Order Stokes Theory. Based upon Chakrabarti's experimental results, however, the Airy Theory is still applicable.

c. The 'working areas' in the irregular wave tests are near those in the regular wave tests.

Airy Linear Wave Theory is chosen to describe the flow kinematics for all of the wave states used; the 2nd Order Stokes Wave Theory is also employed with some steeper regular wave conditions for comparison.
Since the models were tested in intermediate to deep water, the complete form of linear wave theory is used.
Note that the wave kinematics predicted using the chosen wave theory is only valid in the fluid field. Since the Linear Wave Theory was developed on the basis of simplified free surface boundary condition, it does not provide accurate kinematics in the crest-trough region. The treatment of the kinematics near the free surface is discussed in Appendix 4.

III.2 WAVE FORCES

Wave force types can be plotted against the relative wave height H/D and the diffraction number $\pi D/\lambda$ (where D is the leg diameter and λ the wave length) to give a rough indication about the relative importance of drag versus inertia and drag versus diffraction. For irregular waves, H and λ are replaced by H_s and λ_p (where λ_p is the wave length computed using the peak frequency, f_p). A reasonable assumption of the C_d and C_m pairs of values are 1.0 and 2.0 for Model I and 1.5 and 1.5 for Models II and II-M. Using these data the relative importance of drag to inertia is summarized in figures III.4 through III.6 for each of the three models tested.

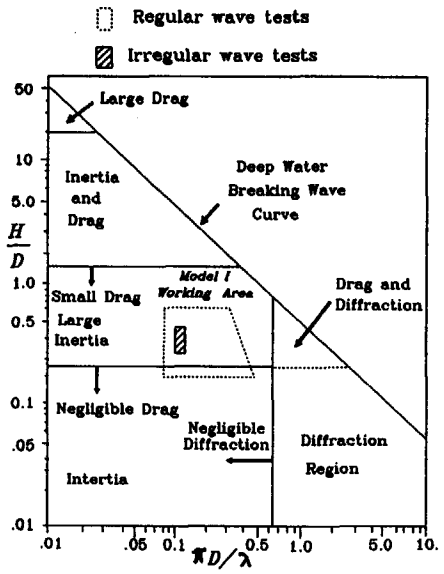

Figure III.4 Relative Importance Drag vs Inertia, Model I

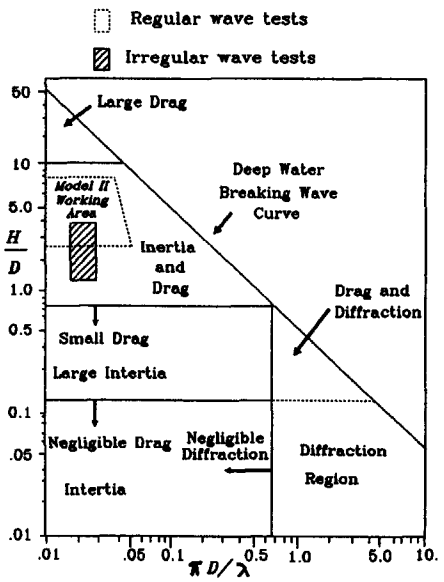

Figure III.5 Relative Importance Drag vs Inertia, Model II

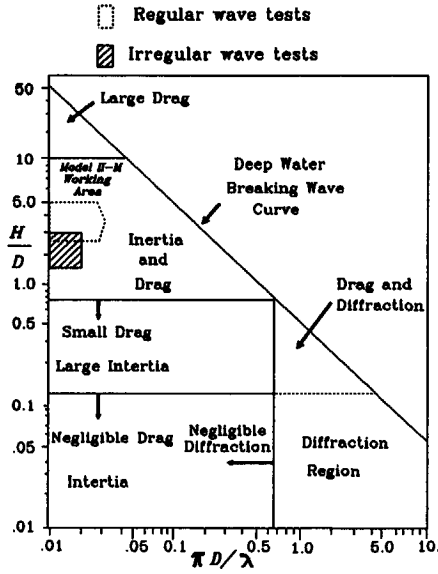

Figure III.6 Relative Importance Drag vs Inertia, Model II-M

These figures show that:

a. With Model I, the hydrodynamic force is essentially inertia dominated in both regular and irregular wave tests.

b. Models II and II-M work in the area where drag force plays a significant role. The drag/inertia ratio with Model II is slightly higher than that with Model II-M.

c. The diffraction effect can be ignored with all three models and thus the Morison Equation is valid for the hydrodynamic force description.

Appendix IV Treatment of nonlinearities and P-δ effect

The nonlinearities with the present physical models originate from structures themselves, the hydrodynamics (free surface, drag term) and the wave-structure interaction (relative motion). Connection nonlinearity cannot adequately be treated here; the model tests were designed to investigate other phenomena; this has been discussed to some extent in Appendix II.1, however. All of the other nonlinearities together with the P-δ effect are discussed in this appendix.

IV.1 FREE SURFACE

Although there exist some numerical schemes based upon the finite-amplitude wave theory which are capable of predicting quite accurate kinematics for certain wave fields - see Rienecker & Fenton (1981), Yuen & Lake (1982) and Sobey (1989), these are not presented as explicit solutions and far too sophisticated to apply in practice. In problems where the waves are not extremely high or where great accuracy is not required, it is more reasonable to use an approximate explicit solution, such as Cnoidal Theory for shallow water or Stokes Theory for deeper water. For practical problem, it is especially desirable to modify the linear wave theory to improve the wave kinematics prediction primarily in the crest-trough region where the correct kinematics information is most essential for the offshore structure analysis and discrepancies between different wave theories are also most obvious.

The linear Airy Wave Theory describes the water motion only up to the (constant elevation) still water level (*SWL*). However, when the wave height is large relative to the water depth, the effect of the changing free surface elevation on the total wave loads (base shear and especially the overturning moments) becomes significant.

Four common approaches for computing the water motion kinematics up to the instantaneous actual wave surface are briefly described as follows:

a. Exponential Extrapolation
   The velocity profile continues exponentially to the actual water surface. For shallow water and high waves this 'primitive' approach is believed to yield very conservative results - the predicted velocities and accelerations near the wave crest will be too large - see Chakrabarti (1986).

b. Vertical Uniform Extrapolation

The kinematics are kept equal to those at the *SWL* up to the wave crest when the actual wave surface is above the *SWL*. Otherwise, standard Airy Theory is used up to the actual water level, just as in method a, above - see Steele *et al.* (1988). This approach is formulated as:

$$u(x,z,t) = u(x,d,t) \qquad for\ d \le z \le d + \eta \tag{IV.1}$$

where:

d = water depth

η = instantaneous wave surface elevation measured from the SWL

This method should be applied with caution as it can lead to overestimation of loads in random waves; this is particularly true for the overturning moment calculation.

c. Linear Extrapolation

Like the vertical extrapolation profile, the linear extrapolation approach modifies the direct exponential extrapolation profile approach only in the region under the instantaneous crest and above the *SWL*, by replacing it with the linear Taylor expansion above the *SWL* - see Forristall (1981):

$$u(x,z,t) = u(x,d,t) + (z - d)\frac{\partial u}{\partial z}(x,d,t) \qquad for\ d \le z \le d + \eta \tag{IV.2}$$

d. Stretching

The kinematics at the instantaneous free surface are considered identical to those originally calculated for the still water level. Wheeler (1970) first introduced a modification in such a fashion by mapping the vertical coordinate z onto a computational vertical coordinate z_s :

$$z_s = z\left(\frac{d}{d + \eta}\right) \tag{IV.3}$$

It follows that:

$$u = \frac{\pi H}{T}\,\frac{\cosh kz_s}{\sinh kd}\cos\psi \tag{IV.4}$$

in which:

u = water particle horizontal velocity
H = wave height
T = wave period
k = wave number
ψ = time dependent phase

A slightly different alternative has been suggested by Chakrabarti (1971):

$$u = \frac{\pi H}{T} \frac{\cosh kz}{\sinh k(d + \eta)} \cos \psi \qquad \text{(IV.5)}$$

With this formulation the effective water depth is changed to $d + \eta$. The remaining kinematics between that free surface and the sea floor follows from traditional linear theory as if it were being applied in the actual (instantaneous) water depth.

These two stretching approaches produce the same kinematics at the free surface, while the Wheeler stretching results in slightly larger values at any other point downwards.

All four wave kinematics modification options as well as standard Airy Theory can be used in *NOSDA*. Note that besides the modification models mentioned above, a great deal of other work has been done in attempt to improve the prediction of the kinematics near the free surface. Among these, Forristall (1981) demonstrates that the Wheeler stretching and the linear extrapolation provides a lower and upper bound respectively for horizontal velocities in the crests of waves. A combination of these two approaches leads to the Delta stretching profile - see Rodenbusch and Forristall (1986). Other schemes proposed for the free surface treatment include Gudmestad model (1990), Gamma extrapolation model - see Borgman *et al.* (1989), and so on. By comparing the kinematics predicted using various free surface treatment approaches with the measured results, Zhang, *et al.* (1991) indicated that there is not a crest-trough kinematic model universally superior for all wave fields; the accuracy of the prediction of each approximate method depends on the wave conditions. The present test setup was not designed to evaluate these crest-trough kinematic models (the wave kinematics were not recorded.) The waves tested were relatively low. The choice of the crest-trough kinematic model is, therefore, not expected to be vital for the structural response simulation. The Wheeler stretching profile is adopted here as the reference case for the model simulations.

Unlike the basic linear wave theory, above, nonlinear wave theories compute water particle kinematics up to the actual free surface. It should be emphasized that a higher order nonlinear wave does not necessarily furnish a better prediction for the wave kinematics, although it generally reproduces a better wave surface profile. Irresponsible use of higher wave theories such as Stokes' Second through Fifth Order Theories for the prediction of wave kinematics often leads conservative results - see Sobey (1989). Data obtained from a structure in the Gulf of Mexico has verified this trend - see Bea and Lai (1978).

It should be noted that inclusion of a free surface effect will, even with a pure sinusoidal input wave, cause a skewness in the total hydrodynamic force on a leg. A simple illustration with horizontal forces on a rigid vertical cylinder is given in figure IV.1. The two total wave force extremes are always 180 degrees out of phase and occur at symmetric points in the sinusoidal water surface profile.

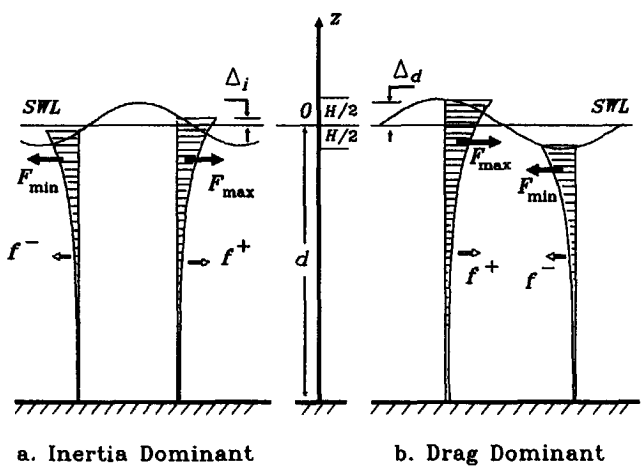

Figure IV.1 Hydrodynamic Force Skewness

In an inertia force dominated case, the extreme wave loads occur in the vicinity of the zero-crossing of the wave profile - within some small distance – from the *SWL*. The extreme total wave forces on the cylinder are calculated using the following integrals which extend from the sea bed to the actual water surface at the moment that the total loading is extreme:

$$F_{max} = \int_{-d}^{\Delta_i} f^+ \, dz$$

$$F_{min} = \int_{-d}^{-\Delta_i} f^- \, dz \qquad \text{(IV.6)}$$

Where f^+ and f^- are the values of the local wave load at the moment that an extreme total load occurs and Δ_i is measured relative to the *SWL*.

Since Δ_i is small, the magnitudes of the maximum and minimum loads are almost the same, and they act almost co-linearly in opposed directions, so that $|F_{max}| \approx |F_{min}|$ and $\Delta F_i = F_{max} - |F_{min}|$ is small.

In contrast to this, for a drag dominated case, the maximum load occurs in the neighborhood of the wave crest and the minimum in the neighborhood of the wave trough. The extreme total wave forces on the cylinder are calculated now by:

$$F_{max} = \int_{-d}^{\Delta_d} f^+ \, dz$$

$$F_{min} = \int_{-d}^{-\Delta_d} f^- \, dz \qquad \text{(IV.7)}$$

where Δ_d is again measured relative to the still water level.

Obviously, Δ_d is nearly equal to $H/2$ and much greater than Δ_i, so that $\Delta F_d = F_{max} - |F_{min}|$ will be larger than above. Also, the resultant lines of action of F_{max} and F_{min} are certainly not co-linear.

The wave climate situation will be between these two extreme cases for the models tested here.

Apparently, hydrodynamic force skewness can be expected to cause skewness in the response to this force as well.

When the vertical cylinder is non-rigid and relative instead of absolute velocities are used in the Morison Equation, the above discussion will become much more complex. The general, qualitative results ($| F_{max} | > | F_{min} |$ and response skewness) will remain valid, however.

IV.2 RELATIVE MOTION

The Morison Equation was originally intended for use with a fixed vertical cylinder in wave. The extrapolated application of this equation to a structure moving in waves leads to several differently revised forms. A commonly accepted approach is to base the hydrodynamic computation on the relative velocity and acceleration:

$$f_w = C_m A_I (\dot{u} - \ddot{x}) + A_I \ddot{x} + C_d A_D |u - \dot{x}| (u - \dot{x}) \qquad \text{(IV.8a)}$$

or

$$f_w = C_m A_I \dot{u} + C_d A_D |u - \dot{x}| (u - \dot{x}) - (C_m - 1) A_I \ddot{x} \qquad \text{(IV.8b)}$$

where:

f_w = wave force per unit length of the vertical cylinder
u = horizontal component of water particle velocity
$\dot{u}$ = horizontal component of water particle acceleration
$\dot{x}$ = cylinder velocity
$\ddot{x}$ = cylinder acceleration
A_D = $\frac{1}{2} D\rho_w$
A_I = $\frac{1}{4} \pi D^2 \rho_w$
D = cylinder outer diameter
ρ_w = ambient water density

In the computer simulation, the third term on the right hand of equation (IV.8b) is moved to the left side of the equation of motion becoming the hydrodynamic force due to the so called 'water added mass'; this is accounted in the computational model by adding this portion of 'mass' to the 'dry' structural mass. For practical 'bookkeeping' reasons, this is done only up to a constant elevation, the *SWL*. This approach introduces an error in the splash zone, where the hydrodynamic mass of a given cylinder element is continually changing. However, this error can be neglected with confidence - see Massie, Liu and Boon (1989).

It is clear from equation (IV.8) that inclusion of relative motion has major consequences for the numerical modeling. Indeed, the entire computation of the external hydrodynamic interaction now becomes dependent upon the (unknown!) velocity of the structure. The proper structure motion will be that for which the computed response agrees with the assumed response used in the computation of the hydrodynamic force.

In *NOSDA* this proper value - in terms of velocity - is determined by iteration. These iterations are carried out several times for each simulation time step, and thus it more than doubles the computational effort.

Hydrodynamic damping influences are automatically included using the relative velocity model of the modified Morison Equation. The difficult task of estimating a somewhat artificial equivalent damping value for a linearized system is avoided.

IV.3 QUADRATIC DRAG TERM

Quadratic drag introduces several complications from an analysis point of view. It introduces a number of higher frequency harmonics in the wave force. A Fourier Series development yields a series in which all even-numbered harmonics are zero. It also shows that the third harmonic has an amplitude which is still 1/5 of that of the first harmonic.

Unlike a frequency domain analysis, the treatment of drag in a time domain *NOSDA* simulation is simple and straightforward. It requires no extra modeling or significant computational effort.

IV.4 *P-δ* EFFECT

The *P-δ* effect is the consequence from secondary moments generated as the deck load becomes eccentric to the vertical leg reaction forces during horizontal displacements. It is modeled by including an extra set of special springs as defined in this section.

Examination of one leg segment subject to an initial, vertical compression load, P - see figure IV.2 - with the nodal displacements u_1 and u_2 shows that the vertical load becomes eccentric and therefore generates an overturning moment. This moment is balanced by a horizontal force pair (F_1 , F_2).

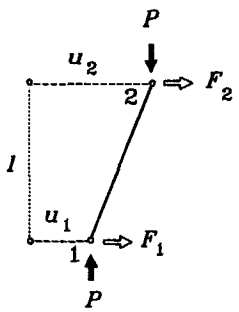

Figure IV.2 Determination of P-δ Spring Coefficient

The equilibrium equations are readily obtained:

$$\begin{Bmatrix} F_1 \\ F_2 \end{Bmatrix} = -\frac{P}{l}\begin{bmatrix} 1 & -1 \\ -1 & 1 \end{bmatrix}\begin{Bmatrix} u_1 \\ u_2 \end{Bmatrix} = \begin{Bmatrix} -1 \\ 1 \end{Bmatrix}(-P/l)\begin{bmatrix} -1 & 1 \end{bmatrix}\begin{Bmatrix} u_1 \\ u_2 \end{Bmatrix} \tag{IV.9}$$

Comparing this to the equilibrium equation for an extension spring (see Appendix V.2.2) shows that it is identical except for a sign. As such, the P-δ effect within the segment can be modeled by a spring with a negative generalized rigidity matrix, $D_g = -P/l$, and a kinematic matrix, $B_g = [\,-1 \;\; 1\,]$.

The applicability of the P-δ modeling can be demonstrated by a simple example. Assume a cantilevered beam subjected to a compression load, P, and discretized into two segments - as in figure IV.3.

The equilibrium equation is expressed as follows:

$$\frac{EI}{l^3}\begin{bmatrix} 1 & -2 & 1 \\ -2 & 6 & -4 \\ 1 & -4 & 3 \end{bmatrix}\begin{Bmatrix} u_1 \\ u_2 \\ u_3 \end{Bmatrix} - \frac{P}{l}\begin{bmatrix} 1 & -1 & 0 \\ -1 & 2 & -1 \\ 0 & -1 & 1 \end{bmatrix}\begin{Bmatrix} u_1 \\ u_2 \\ u_3 \end{Bmatrix} = \begin{Bmatrix} 0 \\ 0 \\ 0 \end{Bmatrix} \tag{IV.10}$$

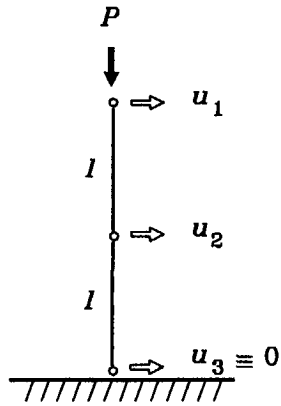

Figure IV.3 Applicability of P-δ Elements

Using the substitution:

$$P = \zeta \frac{EI}{l^2} \tag{IV.11}$$

where:

ζ = coefficient
EI = bending stiffness
l = segment length

yields:

$$\frac{EI}{l^3} \begin{bmatrix} 1-\zeta & -2+\zeta & 1 \\ -2+\zeta & 6-2\zeta & -4+\zeta \\ 1 & -4+\zeta & 3-\zeta \end{bmatrix} \begin{Bmatrix} u_1 \\ u_2 \\ u_3 \end{Bmatrix} = \begin{Bmatrix} 0 \\ 0 \\ 0 \end{Bmatrix} \tag{IV.12}$$

Setting $u_3 = 0$ then yields a second order algebraic eigen value equation:

$$(1 - \zeta)(6 - 2\zeta) - (\zeta - 2)^2 = 0 \tag{IV.13}$$

This equation has two roots:

$$\zeta = \begin{matrix} 0.586 \\ 3.414 \end{matrix} \tag{IV.14}$$

The smaller root leads to the first order critical loading:

$$P = 0.586 \frac{EI}{l^2} \tag{IV.15}$$

Compared with the corresponding result from Euler theory:

$$P = \frac{\pi^2 EI}{16 l^2} \tag{IV.16}$$

or:

$$P = 0.617 \frac{EI}{l^2} \tag{IV.17}$$

It shows that with two segments the predicted result is already only 5% in error relative to the theoretical value. With an increasing number of segments, the result predicted in this fashion will approach and finally converge to the theoretical value.

In the actual modeling, the contribution of leg weight to the P-δ effect is included by summing all the node weights above the investigated segment. As a result of this, the coefficients of the P-δ elements decrease (become more negative) downwards along a leg.

Appendix V Structural modeling

V.1 DISCRETE ELEMENT METHOD

A model structure subjected to time-dependent hydrodynamic loads can be discretized both spatially and temporally to perform a numerical structural dynamic analysis.

A multiple-degree-of-freedom Discrete Element Method (*DEM*) is used here to discretize the structure in space. The *DEM* schematizes the physical object as if it were composed of a finite number of discrete, undeformable elements interconnected by massless, deformable springs and dampers. Lumped masses (or, more generally inertias) are located to correspond with the degrees of freedom of the model. This schematization is generally accepted for the overall dynamic analysis of large complex structures such as jack-up platforms. It has been proven that for a linear system any order of desired numerical accuracy can be obtained; the approach yields converging results as the element size is decreased. For an arbitrary nonlinear system, this convergency is not automatically assured, but its use for such systems has often been successful in practice.

The discrete element method of spatial discretization provides great freedom in modeling. However, as a price of this versatility, the approach demands a sufficient knowledge of structural mechanics combined with user creativity.

After spatial discretization one obtains a structural motion equation having the following form:

$$M \frac{d^2X}{dt^2} + C \frac{dX}{dt} + K X = F\left(t, X, \frac{dX}{dt}\right) \qquad \text{(V.1)}$$

where:

X	=	structural displacement vector
t	=	time
M	=	structural mass (or inertia) matrix
C	=	structural damping matrix
K	=	structural stiffness matrix
F	=	structural load vector

Note that when the system is linear, F is only a function of time, t. The above equation need not be linear. This can be accommodated either by stipulating that M, C and K need not be constant or by including higher order response-related terms in F.

For a jack-up model, the structural load vector, F, is determined from the hydrodynamic analysis. Now, the problem remains of how to determine the M, K and C matrix values. Basically, the *DEM* is a stiffness method which treats the nodal displacements as the fundamental unknowns.
The *DEM* can be seen as a small and specialized 'handicraft shop' next to a big and general 'supermarket', the Finite Element Method (*FEM*) - see Blaauwendraad and Kok (1987). In the standard Finite Element Method, the analysis procedure is as follows. The structural displacement field is expressed as a function of the nodal displacements:

$$u_c(x,t) = N(x)\, u(t) \tag{V.2}$$

where:

u_c	=	displacement field
N	=	interpolation function matrix
u	=	nodal displacement vector

thus, the strain vector can be written as:

$$\varepsilon = B u \tag{V.3}$$

where:

ε	=	strain vector
B	=	displacement - strain relation matrix or kinematic matrix

The constitutive relation, D_ε, links the strain vector, ε, and stress vector, σ:

$$\sigma = D_\varepsilon\, \varepsilon \tag{V.4}$$

For example, with the above relations, using the principle of virtual work, the mathematical formulations for M, K, and C for one leg element in the investigated case result from the following three integrals:

$$M = \int_0^l N^T \rho' N \, dz$$

$$K = \int_0^l B^T D_e B \, dz \qquad \text{(V.5)}$$

$$C = \int_0^l N^T r' N \, dz$$

where:

l = element length
ρ' = mass density per unit length
r' = viscous damping coefficient per unit length

The Discrete Element Method chooses a different approach. The main difference is that generalized strain strains, ε_g, and generalized stresses, σ_g, are applied instead of ε and σ, such that integration over the area of an element is no longer needed. Consider a element with m degrees of freedom (*DOF*s) and generalized displacement vector, u_g. If this element contains i rigid-body *DOF*s, then there are $n = m - i$ *DOF*s left to determine the deformations. These deformations are the generalized strains, ε_g, while the corresponding stresses are the generalized stresses, σ_g. The node displacements and the generalized strains are related via the generalized kinematic matrix, B_g. The generalized strains and generalized stresses are related via the generalized rigidity matrix, D_g, (the generalized constitutive relation). All of these relations can be expressed in formulas as:

$$\varepsilon_g = B_g u_g \qquad \text{(V.6)}$$

$$\sigma_g = D_g \varepsilon_g \qquad \text{(V.7)}$$

The element stiffness matrix can readily be derived:

$$K = B_g^T D_g B_g \qquad \text{(V.8)}$$

Similarly, a system damping matrix, C, can be computed by:

$$C = B_g^T C_g B_g \tag{VI.9}$$

Further explanations and derivations have been given by Blaauwendraad (1989).

V.2 STRUCTURAL MODEL BUILDING BLOCKS

The establishment of a structural computational model is equivalent to choosing a set of mass, stiffness and damping elements with proper characteristics, placing them in proper relative locations and determining proper linkage. The details of the building blocks - namely mass, stiffness and damping elements - are given in the following subsections.

V.2.1 **Mass Elements**

The distributed mass of the structures is lumped at the nodes.

The mass of each of the model jack-up leg elements is divided equally and attached at its two nodes. The mass contribution from one adjacent element of the cylindrical model legs is given by:

$$m = \frac{1}{8} \pi [D^2 - (D - 2t)^2] \rho l \tag{V.10}$$

where:

D	=	outer diameter of the leg
t	=	wall thickness of leg
ρ	=	leg material mass density
l	=	element length

When the node is not located at the ends of the leg (field node), this mass value is doubled in case of equal element length because the final value is the sum of the contributions from two adjacent elements, while only one element contributes to the concentrated mass if the node is located in the leg ends (edge node).

PVC plugs roughly 0.1 m long were mounted in the lower ends of the legs of Model I. This extra mass is taken into account, even though this has only a minor effect to the global dynamic behavior of the model.

The hydrodynamic or 'water added' mass for a submerged cylindrical element is:

$$m_w = \frac{1}{4}\pi (C_m - 1) l D^2 \rho_w \qquad \text{(V.11)}$$

where ρ_w is the ambient water density.

Similarly, this mass is also equally divided and added to the corresponding node masses. The effect of instantaneous elevation in the splash zone on the mass lumping is neglected; constant masses are used throughout. When an element penetrates the still water level - see figure V.1 - the water 'added mass' is lumped to the two nodes as follows:

$$m_l = \frac{2l - l_s}{2l} m' \qquad m_u = \frac{l_s}{2l} m' \qquad \text{(V.12)}$$

Where m' is the 'water added' mass of the submerged portion of the splash zone element.

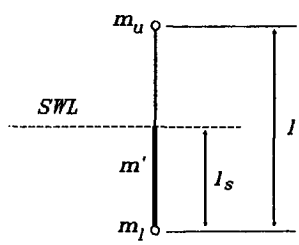

Figure V.1 'Water Added' Mass Lumping on a Splash Zone Element

The deck mass of each model comes from the frame, clamps and accelerometers. Besides, with Model I and Model II-M, extra masses were added to the deck to obtain the desired fundamental natural frequency or enhance the P-δ effect. The deck mass is lumped at the three corner nodes where the deck is connected to the legs. With Model II(-M) the frame mass was measured. With Model I, however, this mass was calculated from its dimensions and material densities, since the deck had already been connected to the legs before starting the experiments. As the accelerometer was

installed on the stern bar of the deck frame, its mass is lumped only to the two nodes at the ends of that bar.

V.2.2 **Stiffness Elements**

The stiffness of each structures tested is modeled by a group of springs. Three types of springs are used:

1. *Extension Springs*

   Figure V.2 shows a spring before and after axial deformation. The extension, Δu , is taken as the generalized strain and the normal force, N , as the generalized stress.

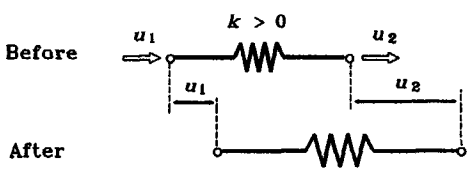

Figure V.2 Extension Spring with Deformation Change

$$\Delta u = u_2 - u_1 \quad \rightarrow\rightarrow\rightarrow \quad B_g = [-1 \quad 1]$$
$$N = k\,\Delta u \quad \rightarrow\rightarrow\rightarrow \quad D_g = k \qquad \text{(V.13)}$$

thus:

$$K = \begin{bmatrix} -1 \\ 1 \end{bmatrix} k \begin{bmatrix} -1 & 1 \end{bmatrix} = \begin{bmatrix} k & -k \\ -k & k \end{bmatrix} \qquad \text{(V.14)}$$

Note that since this spring element has only one generalized strain, Δu, the generalized rigidity matrix, D_g , is a scalar.

An application of this type of spring is to model a bar with stiffness, k, loaded in tension or compression:

$$k = \frac{EA}{l} \tag{V.15}$$

in which A is the cross section area, E the elastic modulus and l the length.

2. *Bending Spring*

This type of spring is mainly used to model the bending stiffness of a beam segment located in the middle of the leg (field segment). (The treatment of edge segments - located in the upper end of the leg - is given in section V.3.1.)

A beam section is replaced by a rigid bar which has two rotation springs at its ends. In fact, each rotation spring can also be considered to be composed of two parallel non-collinear extension springs.

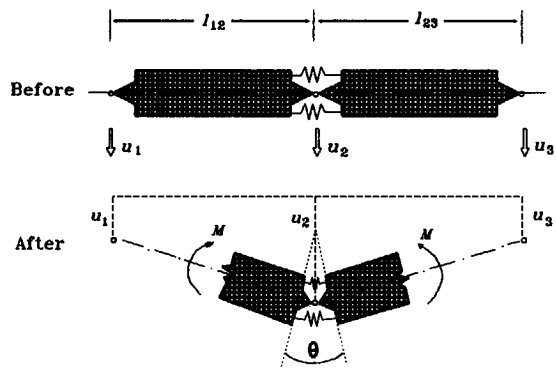

Figure V.3 Rotation Spring with Deformation Change

The generalized strain is now the angle, θ, and the corresponding generalized stress is the moment M. For relatively small rotations:

$$\theta = \frac{u_2 - u_1}{l_{12}} + \frac{u_2 - u_3}{l_{23}} \rightarrow\rightarrow B_g = \left[-\frac{1}{l_{12}} \quad \frac{1}{l_{12}} + \frac{1}{l_{23}} \quad -\frac{1}{l_{23}} \right]$$

$$M = \frac{EI}{\frac{1}{2} l_{12} + \frac{1}{2} l_{23}} \theta \rightarrow\rightarrow D_g = \frac{2EI}{l_{12} + l_{23}} \tag{V.16}$$

When l_{12} is identical to l_{23}, then the element length, l, in the generalized difference matrix, B_g, can be moved to the rigidity matrix, D_g, yielding:

$$B_g = [-1 \quad 2 \quad -1]$$
$$D_g = \frac{EI}{l^3} \tag{V.17}$$

and the stiffness matrix is:

$$K = \begin{bmatrix} -1 \\ 2 \\ -1 \end{bmatrix} \left[\frac{EI}{l^3} \right] [-1 \quad 2 \quad -1] = \frac{EI}{l^3} \begin{bmatrix} 1 & -2 & 1 \\ -2 & 4 & -2 \\ 1 & -2 & 1 \end{bmatrix} \tag{V.18}$$

3. *P-δ Spring*

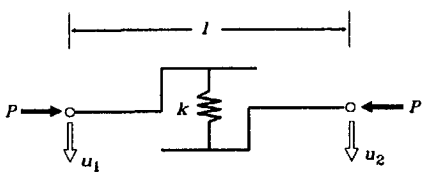

$$k = -\frac{P}{l}$$

Figure V.4 P-δ Spring with Deformation Change

This type of virtual spring is used to model the second order moment caused by the deck weight (*P-δ* effect). Such a spring provides a positive rather than a negative force as a result of a positive displacement. It is of the same form as the extension spring, except that its elastic coefficient, k, and therefore the generalized rigidity matrix, D_g (here this is also a scalar), are negative.

Hence, again one has:

$$\begin{aligned} \varepsilon_g &= u_2 - u_1 \quad \Rightarrow\Rightarrow\Rightarrow \quad B_g = [-1 \quad 1] \\ \sigma_g &= k\,\varepsilon_g \quad \Rightarrow\Rightarrow\Rightarrow \quad D_g = k \end{aligned} \tag{V.19}$$

thus:

$$K = \begin{bmatrix} -1 \\ 1 \end{bmatrix} k \, [-1 \quad 1] = \begin{bmatrix} k & -k \\ -k & k \end{bmatrix} \tag{V.20}$$

with $k = -P/l$.

More details about the use of this type of spring and the derivation of k have already been given in Appendix IV.4.

V.2.3 **Damping Elements**

Two types of specific damping elements are used:

1. Extension damper
2. Bending damper

Procedures similar to those used in the previous section to generate the stiffness matrices for extension and rotational springs are also used for the generation of the damping matrix. Here, displacements are replaced by velocities and strains by strain rates.

V.3 THEORETICAL MODELING OF CONNECTIONS

The connections at both ends of a leg have been highly simplified in the design of the physical models, when compared to actual jack-up rigs. Even so, the preliminary processing of the experimental data has already shown that the mechanical behavior of these simplified connections was far more complicated than desired. Without losing the vision of the connection deviation from their design, the modeling approach of ideal connections is discussed in this section for the sake of theoretical completeness. In fact, the idealized approach can be the most responsible approximation when the necessary specific information on the connections is not available as in the present case.

V.3.1 **The Deck and Its Leg Connection**

The model deck consists mainly of a triangular frame of hollow, square bars. It is not difficult to show that with all models both the extension stiffness and the bending stiffness of the decks are at least one order of magnitude higher than those of the legs; it is reasonable to consider the decks to be rigid - see Liu (1989).

The deck is designed to be rigidly clamped to the legs. Under this ideal condition, the bending spring linking a leg to the deck (edge node) is twice as stiff as a field spring along the leg. The connections actually constructed are less rigid and more complicated than the intended design; softer bending springs are used in the computational schematizations for the models tested. Accompanying the bending springs, rotational dampers are used to represent the (large) connection local damping.

V.3.2 **Bottom Connection**

By design, the legs are perfectly hinged to the bottom plate. This is physically implemented using universal joints. Theoretically the joint hinges provide no rotational resistance (neither stiffness nor damping). In practice, it seems reasonable to model the hinge as a rotational damper with a small damping coefficient. The connection between the hinge and the bottom plate is modeled by two translational extension springs (one vertical and another horizontal) and two corresponding translational extension dampers. This is illustrated in figure V.5.

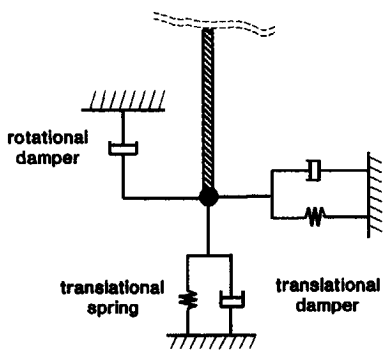

Figure V.5 Leg to Bottom Schematization

Appendix VI Numerical computational aspects

VI.1 NUMERICAL STABILITY AND LOCAL ITERATION ERROR CONTROL

A Discrete Element Method (*DEM*) spatial discretization yields a set of ordinary differential equations of motion. In *NOSDA* these equations are solved numerically using the Kok - γ direct integration method in the time domain - see Blaauwendraad and Kok (1987). In the actual computation, the integration parameter γ is chosen to be zero - see Liu and Massie (1988). The system then works using a constant displacement field and works identically to the Newmark - β method. This numerical method is unconditionally stable for a linear system. For the present nonlinear case, the stability is not automatically assured; its assumption is commonly considered to be reasonable, however. Luckily, divergence of an unstable simulation is usually quite obvious.

Since the relative motion form of the modified Morison Equation is used, the hydrodynamic load is dependent upon the (as yet unknown) structural velocity. The structural velocity is determined by iteration, starting with its value at the end of the previous time step as a first guess. This assumed value is revised iteratively until the local iterative error - the difference between the structural response assumed in the hydrodynamic force computations and that resulting from the dynamic analysis - is sufficiently small. A balance with other sources of errors (for example, truncation error inherent with the time integration technique - to be discussed in the following section) is needed when choosing the tolerance for iteration; this should not be set too low or too high; it should be compatible with other errors. In actual computation, the iteration error displacement tolerance is set to be 10^{-7} m with the regular wave simulation and 10^{-6} m with the irregular wave simulations. This is small enough compared to the magnitude of the model response at deck level (in order of 10^{-3} to 10^{-2} m).

VI.2 LOCAL TRUNCATION ERROR AND TIME STEP

Besides the above iteration error, the time discretization also inevitably introduces truncation error. Like all straight-line acceleration methods, the Newmark - β technique used here is of second order accuracy; acceleration is of the order $O(\Delta t^2)$, and therefore velocity is $O(\Delta t^3)$, and displacement is $O(\Delta t^4)$.

Truncation accuracy is improved by reducing the time step and computational efficiency is usually enhanced by a longer time step. However, a too long time step often results in a bad first guess for the starting point for the iteration as addressed in the previous section and thus too many iteration loops are needed within one step before the error tolerance is met. The proper time step choice is always a compromise between these requirements of speed versus accuracy.

Another factor which must be considered when choosing a time step for a simulation, is that the chosen interval must be short enough to generate the necessary information within each response period of interest. Two samples per cycle is the minimum amount of data needed to determine Fourier Series coefficients, for example. The number of time steps per fundamental motion period must, therefore, be at least twice the number of harmonics needed to encompass the desired motion information. A commonly accepted criterion is that there should be at least 20 time steps within one fundamental period. In the regular wave simulations as studied in Chapter 6, the shortest wave is about 0.6 s (f = 1.7 Hz), so that the time step should not be longer than 0.03 s with this wave. In fact, Hxtime step of 0.03 s is chosen for all regular wave simulations to assure a desirable accuracy. With this time step value the resulting order of numerical accuracy becomes: acceleration 10^{-3} m/s^2, velocity 10^{-5} m/s and displacement 10^{-7} m. This is about the same as the iteration error tolerance chosen above.

With irregular waves, the peak frequencies vary from 0.545 Hz to 0.945 Hz. Since the spectra used are generally narrow-banded, there are few waves with frequency higher than 1 Hz. It is, therefore, reasonable to use a longer time step. A time step of 0.05 s is chosen so that there are at least 20 data points within one fundamental cycle. This time step is chosen, in fact, also to match the sampling time interval used for the measured data digitalization; this is convenient for the data analysis as well. With this time step, the order of numerical accuracy becomes: acceleration 10^{-3} m/s^2, velocity 10^{-4} m/s and displacement 10^{-6} m; this is consistent with the error tolerance set for the iteration.

As a numerical check, various time steps have been used for the response computation of Model I with a regular wave of 4 cm high and frequency of 0.9 Hz (T = 1.1 s). The results are given in table VI.1 in which Δt is the time step, $\hat{u}_A$ the computed displacement amplitude at the deck.

This table shows that when the chosen time step is not sufficiently small, the iteration cannot converge to the desired error band within a given number (here 20) of iteration loops. It is also clear that with a time step which includes more than about 20 intervals (Δt = 0.05 s, for example) within one period (here 1.1 s), the computed result will be sufficiently close to the desired solution; refining time step only results in a minor change.

Table VI.1 Results of Various Time Steps

Δt (s)	$\hat{u}_A$ (cm)	$T/\Delta t$ (-)
0.1	Divergent	11
0.07	Divergent	16
0.05	2.527	22
0.04	2.532	28
0.03	2.531	36
0.02	2.527	55

Similar numerical testing has also been done with Model II. It is found that the range of convergent time steps for Model II is much larger than that for Model I. This is understandable; a given wave state generates much larger exciting forces and structure responses with Model I than with Model II, therefore the structural velocity plays a less important role in the simulation of Model II.

VI.3 TRANSIENT DECAY

When the excitation of a linear system is sinusoidal, a complete solution of the structural motion equations includes two parts: a homogeneous response, u_1 , and an externally excited response, u_2 . For a single degree of freedom system with a sinusoidal excitation, the displacement is expressed as:

$$u = u_1 + u_2 \qquad \text{(VI.1a)}$$

with:

$$u_1 = A_1 e^{-nt} \sin(\omega' t - \phi)$$

$$u_2 = A_2 \sin(\omega t - \psi) \qquad \text{(VI.1b)}$$

$$\omega' = \sqrt{\omega_n^2 - n^2}$$

Where:

- n = decrement coefficient
- ω = circular excitation frequency
- ω_n = circular natural frequency
- ϕ = free vibration phase
- ψ = forced vibration phase
- A_1 = initial free vibration amplitude
- A_2 = forced vibration amplitude

u_1 will die out during a certain period. Note that even with a zero initial condition (both initial displacement and velocity are zero), the transient motion still exists; this can be seen from equation (VI.1): $u = 0$ and $\dot{u} = 0$ at $t = 0$ do not yield $A_1 = 0$.

The test records from the models in waves are steady state responses. Accordingly, the simulated response should also be taken after u_1 dies out. The number of cycles needed for the amplitude of u_1 to decay to 1% of its initial (maximum) value, A_1^0 is given by:

$$j = \frac{1}{\delta} \ln \frac{A_1^0}{A_1^j} \qquad \text{(VI.2)}$$

$$= \frac{4.61}{\delta}$$

where δ is the log decrement and the superscript j indicates the cycle number.

Using the data in table 4.4 yields $j = 18$ for Model I and $j = 4$ for model II. This can also be numerically confirmed by free vibration simulation using the 'dry' computational models for these models. This is done by setting an initial displacement at the deck level of the computational model and then letting it go. The amplitude decays with time; this is shown in table VI.2.

It can be seen that the number of cycles needed for filtering out the transient response vary dramatically from one model to another. This indicates that the duration of the transient period depends heavily on the damping level.

By comparison, the damping percentage of a realistic jack-up (4 to 6% of the structural plus soil damping - see Carlsen *et al.* (1989)) is in the order of that of Model I (4.1%). Therefore, a transient period lasting about 20 cycles should be appropriate with a prototype jack-up.

Table VI.2 Transient Vibration Decay

Model	Cycle j	Time (s)	A_1^j (cm)	A_1^j / A_1^0 (%)
I	0	0	6.000	100
	10	10	0.446	7.4
	18	18	0.059	0.98
II	0	0	5.0	100
	2	2	0.446	8.9
	4	4	0.044	0.73

Appendix VII Computation efficiency

The computational effort needed to simulate the dynamic behavior of an offshore structure generally depends upon the following factors:

- Structure Size and Complexity
  A larger and more complex structure requires more degrees of freedom; the computational effort is directly proportional to: (number of the degrees of freedom)$^{\alpha}$ where α is an exponent with a value between 2 and 3.
- Incident Wave Frequency Components
  With a regular wave simulation, the choice of the integration time step is dependent upon the input wave period (not fewer than 20 time steps within one period). With an irregular wave simulation, besides the requirement that there are a sufficient number of data points within one primary cycle, another (often less critical) condition should also be satisfied: there must be at least two sample points per cycle for the shortest wave of interest. When the random wave surface is represented by superposition of a group of wave components (the Random Phase Theory), the choice of the spectral partition has a direct influence on the computation efficiency.
- Nonlinearity
  The nonlinearities can be material, geometric and hydrodynamic. Inclusion of a nonlinear effect normally means invoking some sort of iterative loop; this will increase computational effort considerably.

When only the steady state response with a regular wave simulation is of interest, the overall damping level of the structure also influences the total computing time. In this case, the transient response still needs to be computed although not counted in the bookkeeping. The total damping level (sum of structural and hydrodynamic damping) determines the cycles necessary for filtering out the transient response at the start. For example, to filter out the free vibration influence, about 18 natural periods are needed with Model I in air while only 4 natural periods are needed with Model II in air - see Appendix VI. Inclusion of hydrodynamic damping is expected to further shorten these transient stages. Applying a ramp function, which increases from zero to 1 over a duration, to the excitation force could accelerate the decay of the transient motion. This function is not used here since the computing demand for the simulation of the present models is modest - especially with Model II(-M) whose decay time span due to structural damping alone lasts only about 4 cycles.

The present modeling excluded physical nonlinearity of the structures; the global stiffness matrix and the damping matrix remain unchanged during one run. If physical structural nonlinearity is introduced (using elasto-plastic springs to model the deck-leg connection, for example), then the instantaneous response level must be checked continuously so that the global stiffness can be re-established when the deformation becomes plastic. This will significantly increase the computational effort.

Different types of hydrodynamic nonlinearities require different levels of computing effort. For example, the free surface effect and quadratic drag as well as higher order regular wave theories can be treated in a quite straightforward way. They have little effect on the computation time.

The wave-structure relative velocity used in the present modeling greatly increases computing effort, however. Since the time step is chosen to be small (at least 20 steps per primary wave), the tolerance criterion is normally satisfied after the first velocity-force iteration loop. Even then, the computation effort is still increased by a factor of about 2.

The P-δ effect is included using a group of special negative spring elements; this increases the number of stiffness elements without introducing extra degrees of freedom. Inclusion of the P-δ effect, therefore, does not significantly lengthen computing time.

Obviously, for different input wave frequencies and different structures, the simulation times are quite different. It is, therefore, difficult to give a general evaluation of the computational effort. Nevertheless, experience with computations for this study can give some indication of the computing time consumption.

The following description represents a 'standard' case for this evaluation. Each of the models investigated has roughly 40 degrees of freedom. The water kinematics are calculated using linear Airy Wave Theory. The influences of the free surface effect, relative velocity and P-δ effect are included. The structural nonlinearity resulting from the deck-leg connection imperfection is excluded.

With a regular wave simulation, for an excitation period near the structural fundamental natural period (around 1.2 s), using a time step of 0.03 s (40 time steps per cycle), the DECstation 3100 Computer needs about 39 s of CPU time to simulate a clock duration

of 40 s; this gives a rough indication of the computational efficiency. The ratio between the simulation time and the physical time is an efficiency of about 1:1 for regular wave simulations.

The structural response computation with irregular wave simulations is basically the same as with regular wave simulations. Since more waves (instead of one single wave) are superposed to calculate the instantaneous wave surface and wave kinematics, more computing time is obviously needed in the hydrodynamic part. More specifically, in the present study, the time step is chosen to be 0.05 s and wave peak frequency is around 0.8 Hz. Therefore, there are about 25 data points per primary cycle. Using the same structural models as used with regular wave simulations and 25 waves representing a spectrum, a simulation of 1034 s of clock time costs the DECstation 3100 around 8000 s of CPU time. The ratio of the simulation time to the physical time is about 8:1.

In view of the discussions above, a fully linearized system with a relatively larger time step is expected to achieve an higher efficiency. On the other hand, inclusion of all possible nonlinearities with the given number of degrees of freedom will downgrade the efficiency. The range of possible computational efficiencies is quite wide. Even so, *TILLY* - the structural analysis kernel of *NOSDA* - has been found by Blaauwendraad (1989) to be efficient when compared to other time domain nonlinear analysis systems. Of course, no time domain analysis can match the overall speed of a frequency domain analysis for a linearized system.

Appendix VIII Further data preparation: segmenting, windowing and overlapping

After data preprocessing (band-filtering, units conversion, etc.), additional preparations of the data are necessary for the frequency analysis. These preparations include three steps: segmenting, overlapping and windowing. All of them are carried out to improve the accuracy of the resulting estimates. They are described in the following sections.

VIII.1 SEGMENTING

If the total time series as a whole is directly used for the estimate of a quantity in the frequency domain, the associated statistical error is usually unacceptable. For example, the standard deviation of the estimate of a power density so obtained is always equal to the expectation value of the quantity being estimated. It should be emphasized that the accuracy cannot be improved by increasing the record length or refining the sampling frequency without applying one spectral smoothing technique or the other. Instead of increasing the accuracy of the estimate, the information gained by increasing the total record length goes to the refining of the frequency resolution of the estimate, and the information obtained by decreasing the sampling interval is absorbed by increasing the Nyquist frequency. In practice, the random error of an estimate is reduced by smoothing the estimate further in one of two ways: The first way is to smooth over an ensemble of estimates. This is done by computing individual estimates from n_d independent sample records, $x_i(t)$, $i = 1, 2, ..., n_d$, and then averaging the n_d estimates at each frequency of a spectral component. This smoothing procedure will reduce the variance by a factor of n_d . The second way is to smooth over frequency. This can be done by averaging together for l_d contiguous spectral components in the estimate from a single sample record. The first technique is computationally more efficient than the second technique by a modest factor, since it is logarithmically more efficient to take many shorter FFTs than one longer one. In the present study, the record length is quite long; the first technique is, therefore, a natural choice.

Each of the time series is divided into n_d independent segments. The choice of n_d is a compromise between the bias error suppression and random error suppression. In the present work the segment number n_d is chosen to be 20 for Model I and 40 for Models

II and II-M. The total number of data points, N_r, from the units conversion is 10240 (the total record length, T_r = 1024 s) for each record. This means that each segment consists of 512 data points (T_s = 51.2 s) with Model I and 256 data points (T_s = 25.6 s) with Models II and II-M - where T_s denotes the length of an individual segment. The variance of the estimate in this case, relative to using a whole record as a single segment, is reduced by a factor n_d.

Another useful quantity for error analysis is called the number of degrees of freedom (denoted by ν) which is equal to twice the number of the segments ($\nu = 2\, n_d$). This parameter is needed to determine sampling distributions of estimates of various spectral quantities (*CHI*-Square Distribution for autospectral estimates, *F* Distribution for frequency response function estimates, for example). The number of degrees of freedom often indicates the accuracy of the estimates. Usually, the higher the number of degrees of freedom is, the lower the random errors.

VIII.2 OVERLAPPING

Since the present study is an 'off-line' analysis, the total length of the record is fixed. It is, of course, desirable to achieve the ultimate accuracy (or the smallest variance) from these (fixed amount of) data. One technique for this is overlapping. More specifically, instead of directly using n_d independent segments, $x_i(t)$, $(i - 1)T_s \le t \le iT_s$, $i = 1, 2, .., n_d$, as the input for the spectral analysis, the data division $x_i(t)$ is taken covering the time intervals:

$$[q(i-1)]T_s \le t \le [q(i-1)+1]T_s \qquad (VIII.1)$$

$$i = 1, 2, ..., (n_d/q) \qquad q \le 1$$

It is usually optimal, or very nearly optimal, to overlap the segments by one half of their length (q = 0.5). This results in $2\, n_d$ - 1 segments (nearly doubles the original number of segment n_d). It should be noted that the variance reduction is not a full factor of $2\, n_d$ - 1, since the overlapped segments are not statistically independent. It can be shown that the variance is reduced instead by a factor of about (9/11)($2\, n_d$ - 1) - see Press *et al.* (1986). Accordingly, the equivalent number of the segments is 32 (n_e = (9/11)(2 · 20 - 1) - with Model I and 64 with Models II and II-M. The corresponding equivalent number of degrees of freedom, ν_e, is 64 for Model I and 128 for Models II and II-M.

VIII.3 WINDOWING

The simplest FFT with a square window introduces a significant amount of leakage into the neighboring bins. The reason for the leakage is that the square window function turns on and off so rapidly; its Fourier transform has substantial components at high frequency. To remedy this situation, one can weigh the input data x_i , i = 0, 1, ..., N_s - 1 (where N_s is the number of the points within an individual segment) by a window function, w_i , that changes more gradually from zero to a maximum and then back to zero as i ranges from 0 to N_s - 1.

There is a lot of perhaps unnecessary lore about the choice of a window function, and practically every function which rises from zero to a peak and then falls again has been named after someone - for example, Parzen window, Hanning window, Hamming window, Whelch window. Roughly speaking, their differences lie in subtle tradeoffs between making the central peak of the spectral leakage function as narrow as possible versus making the tails of the function fall off as rapidly as possible. The Hanning window (sometimes also called cosine squared window) is chosen for the present analysis. This window is given by:

$$w_i = \frac{1}{2}\left[1 - \cos\left(\frac{2\pi i}{N_s - 1}\right)\right] \qquad \text{(VIII.2)}$$

The windowing obviously results in a loss in the magnitude in the spectral density estimate. This loss is compensated by a factor:

$$\textit{correction factor} = \frac{N_s}{\sum_{i=0}^{N_s-1} w_i^2} \qquad \text{(VIII.3)}$$

for a Hanning window this correction factor is approximately $\sqrt{8/3}$.

The windowing used to suppress side-lobe leakage also increase the width of the main lobe of the spectral window; that is, it reduces the basic resolving power of the analysis. With the Hanning window, the increase in the half-power width of the main lobe is about 60% compared with the simple square window. This is generally an acceptable price to pay for the suppression of leakage to frequencies outside the region of the main lobe.

Appendix IX Statistical errors and confidence intervals

IX.1 DEFINITIONS OF ERRORS

First, some concepts will be defined as background for the error analysis formulas given later in this appendix. Let a tilde ($\tilde{}$) symbol over a quantity ϕ, namely $\tilde{\phi}$, denote an estimate of this quantity.

Conceptually, suppose $\tilde{\phi}$ can be estimated many times by repeating an experiment or some measurement program. Then, the expected value of $\tilde{\phi}$, denoted by $E[\ \tilde{\phi}\ ]$, is something one can estimate. For example, if an experiment is repeated N times to yield results, $\tilde{\phi}_i$, $i = 1, 2, ..., N$, then:

$$E[\ \tilde{\phi}\ ] = \frac{1}{N} \sum_{i=1}^{N} \tilde{\phi}_i \qquad \text{(IX.1)}$$

This expected value may or may not equal the true value ϕ. If it does, the estimate is said to be unbiased. Otherwise, it is said to be biased. The bias of the estimate, denoted by $b[\ \tilde{\phi}\ ]$, is equal to the expected value of the estimate minus the true value, that is:

$$b[\ \tilde{\phi}\ ] = E[\ \tilde{\phi}\ ] - \phi \qquad \text{(IX.2)}$$

The bias error is a systematic error that always occurs with the same magnitude in the same direction when measurements are repeated under identical circumstances.

The variance of the estimate, denoted, $Var[\ \tilde{\phi}\ ]$, is defined as the expected value of the squared differences from the mean value. It follows:

$$Var[\ \tilde{\phi}\ ] = E[(\ \tilde{\phi} - E[\ \tilde{\phi}\ ])^2\ ] \qquad \text{(IX.3)}$$

The variance describes the random error of the estimate, that is, that portion of the error that is not systematic and can occur in either direction with different magnitudes from one measurement to another.

An assessment of the total error is given by the mean square error, which is defined as the expected value of the squared differences from the true value, computed by:

$$\textit{mean square error}\ [\tilde{\phi}] = E[(\tilde{\phi} - \phi)^2] \tag{IX.4}$$

It is easy to verify that:

$$E[(\tilde{\phi} - \phi)^2] = Var[\tilde{\phi}] + b^2[\tilde{\phi}] \tag{IX.5}$$

The square root of $Var[\tilde{\phi}]$ yields the standard error or random error, as follows:

$$\textit{random error} = \sigma[\tilde{\phi}] = \sqrt{E[\tilde{\phi}^2] - E^2[\tilde{\phi}]} \tag{IX.6}$$

The root mean square (rms) error is defined as:

$$\textit{rms error} = \sqrt{E[(\tilde{\phi} - \phi)^2]} = \sqrt{\sigma^2[\tilde{\phi}] + b^2[\tilde{\phi}]} \tag{IX.7}$$

As a further convenience, it is often desirable to have the error in a (relative) percentage form. This is done by dividing the error by the quantity being estimated to obtain a normalized error. For $\phi \neq 0$, the normalized random, bias, and rms errors are given by:

$$\begin{aligned}
\textit{normalized random error} &= \varepsilon_r = \frac{\sqrt{E[\tilde{\phi}^2] - E^2[\tilde{\phi}]}}{\phi} \\
\textit{normalized bias error} &= \varepsilon_b = \frac{E[\tilde{\phi}]}{\phi} - 1 \\
\textit{normalized rms error} &= \varepsilon = \frac{\sqrt{\sigma^2[\tilde{\phi}] + b^2[\tilde{\phi}]}}{\phi}
\end{aligned} \tag{IX.8}$$

IX.2 STATISTICAL ERRORS OF PROBABILITY ESTIMATES

The bias and variance of the estimate of the density function, $\tilde{p}$, (the derivative of the distribution function) have been formulated by Bendat and Piersol (1986).

A first-order approximation for bias term is given by:

$$b[\tilde{p}(x)] \approx \frac{W^2}{24} p''(x) \tag{IX.9}$$

where $p''(x)$ is the second derivative of $p(x)$ with respect to x and W the window width between two succeeding histogram steps or levels. W is chosen to be 0.142 for all models.

The random error of probability density estimates may be approximated by:

$$\sigma[\tilde{p}(x)] = c\sqrt{\frac{p(x)}{N_r W}} \tag{IX.10}$$

where the constant c is dependent on the autocorrelation function of the data and the sampling rate and N_r the number of data points in the total record. For continuous bandwidth limited white noise, experimental studies indicate $c \approx 0.3$. In other cases c is more nearly equal to one - see Bendat and Piersol (1986). The exact value of the constant c is very difficult to obtain. A c value of 1 is used for approximation.

Combining the equations (IX.9) and (IX.10), the normalized root mean square error is approximated by:

$$\begin{aligned} \varepsilon[\tilde{p}(x)] &= \frac{\sqrt{b^2[\tilde{p}(x)] + \sigma^2[\tilde{p}(x)]}}{p(x)} \\ &\approx \sqrt{\frac{W^4}{576}\frac{p''^2(x)}{p^2(x)} + \frac{c^2}{N_r W p(x)}} \end{aligned} \tag{IX.11}$$

It is clear from the above equation that there are conflicting requirements on the width W in probability measurements. On the one hand, a large value of W is desirable to reduce the random error. On the other hand, a small value of W is needed to suppress the bias error. However, the total error will approach zero as the record length, T_r, approaches ∞ if W is restricted so that $W \to 0$ and $WT_r \to \infty$.

The distribution function is equal to the integral of the density function from $-\infty$ (in the present case from 0) to a specific value, x. If one sets:

$$\tilde{p}(x) = p(x)(1 + \varepsilon_b) \tag{IX.12}$$

then:

$$\int_0^x \tilde{p}(\xi)\,d\xi = \int_0^x p(\xi)(1 + e_b)\,d\xi \qquad \text{(IX.13)}$$

thus:

$$\tilde{P}(x) = P(x)\left[1 + \frac{1}{P(x)}\int_0^x e_b\, p(\xi)\, d\xi\right] \qquad \text{(IX.14)}$$

therefore:

$$e_b(P) = \frac{1}{P(x)}\int_0^x e_b(p)\, p(\xi)\, d\xi \qquad \text{(IX.15)}$$

Assuming that the value of the largest normalized bias error for the density function estimate is $\hat{e}_b\,(p)$ - which occurs mostly at the curve peak and thus is less than zero, it follows from equation (IX.15):

$$|e_b(P)| \le \frac{|\hat{e}_b(p)|}{P(x)}\int_0^x p(\xi)\, d\xi = |\hat{e}_b(p)| \qquad \text{(IX.16)}$$

The normalized bias errors for the probability distribution estimates are, therefore, always equal to or smaller than the largest normalized bias error for the probability density estimates (in the absolute value sense). In practice, values of $W \le 0.2\ \sigma_x$, will usually limit the normalized bias error of the density and thus distribution function to less than 1% - see Bendat & Piersol (1986). This is true because of the $p''(x)$ term in the bias portion of the error; probability density functions of common (approximately Gaussian) random data do not show abrupt or sharp peaks which lead to a large second derivative. In the present case, $W = 0.142\ \sigma_x$ ($\sigma_x = 1$ for normalized data used here) has been chosen; the bias of the distribution function is expected to be smaller than 1% and therefore can be neglected.

Now, attention is focused on the random error (the normalized random error is considered equal to the rms error). For situations where e_r is small, if one sets:

$$\tilde{p}(x) = p(x)(1 \pm e_r) \qquad \text{(IX.17)}$$

then:

$$\int_0^x \tilde{p}(\xi)\,d\xi = \int_0^x p(\xi)(1 \pm e_r)\,d\xi \qquad \text{(IX.18)}$$

thus:

$$\tilde{P}(x) = P(x)\left[1 \pm \frac{1}{P(x)} \int_0^x e_r\, p(\xi)\, d\xi\right] \qquad \text{(IX.19)}$$

therefore:

$$e_r(P) = \frac{1}{P} \int_0^x e_r(p)\, p(\xi)\, d\xi \qquad \text{(IX.20)}$$

from of equations (IX.10) and (IX.20) one has:

$$e_r(P) \approx \frac{c}{P\sqrt{N_r W}} \int_0^x \sqrt{p(\xi)}\, d\xi \qquad \text{(IX.21)}$$

The normalized random error of the distribution function formulated above can be approximated by replacing p by $\tilde{p}$ and P by $\tilde{P}$. The integral is computed numerically. N for all runs is 10240 (corresponding to 1024 s) and W is 0.142. This results in a reasonably large value of WT_r (= 145). The actual calculation using the present parameters chosen shows that the random error of the probability distribution estimate is less than 4% with Model I and less than 5% with Models II and II-M. The estimates so performed are therefore rather reliable.

IX.3 STATISTICAL ERRORS OF SPECTRAL ESTIMATES

The formulas used in the error analysis are concisely listed in this section. The detailed derivations are omitted, but can be found, for example, in the literatures by Bendat and Piersol (1971 and 1986) and Jenkins and Watts (1968).

Autospectrum Estimate

The first order approximation of the normalized bias error of an autospectrum estimate, $\tilde{G}_{xx}$, is given by

$$e_b[\tilde{G}_{xx}(f)] \approx \frac{B_e^2}{24} \frac{G''_{xx}(f)}{G_{xx}(f)} \qquad \text{(IX.22)}$$

where B_e is the resolution bandwidth given by:

$$B_e = \frac{1}{T_s} = \frac{n_d}{T_r} \qquad \text{(IX.23)}$$

thus equation (IX.22) can also be written as:

$$e_b(f) \approx \frac{n_d^2}{24T_r^2} \frac{G''_{xx}(f)}{G_{xx}(f)} \qquad \text{(IX.24)}$$

The normalized random error of the autospectral estimate is given by:

$$e_r(f) = \frac{1}{\sqrt{B_e T_r}} = \frac{1}{\sqrt{n_d}} \qquad \text{(IX.25)}$$

It is clear from the above equations that there are conflicting requirements on the resolution bandwidth, B_e, (and thus on the number of segments, n_d, since the total record length, T_r, is fixed). A small value of B_e (fewer segments) is needed to suppress the bias portion of the error while a large value of B_e (more segments) is desired to reduce the random portion of the error. This is similar to the situation discussed in Section IX.2 for the window width, W, in the probability distribution measurement. The problem here, however, is more critical since the autospectra in the present study are rather narrow-banded. A narrow-band spectrum generally displays a sharp peak; the sharp peak, in turn, reflects a large second derivative (near the peak). It should be noted that in the present case of large second derivatives the first order approximation of the normalized bias error expressed in equations (IX.22) and (IX.24), generally speaking, will exaggerate the degree of bias in estimates. The bias error increases as $G''(f)$ increases ($G(f)$ becomes more peaked) for a given B_e, or as B_e increases for a given $G''(f)$. Also, it should be noted that the bias error is always in the negative

direction; that is, spectral density peaks are underestimated and spectral density valleys are overestimated.

The bias term involves both the resolution bandwidth, B_e, and the second derivative of the spectrum being estimated. The true value of the latter parameter is unknown and it is unrealistic to attempt to determine it even from the estimated spectral density (which itself is already an *approximation*). In fact, the author has used different approaches (such as Fourier series, polynomial approximation, sampling function, and so forth) to smooth the estimated curve, and then to determine the second derivative. The results from different approaches differed by more than a factor of ten. This scatter is expectable in view of the fact that every differentiation costs one order of accuracy. However, an empirical 'rule of thumb' - extensively accepted in practice - is that in order to keep the bias sufficiently low the resolution should be chosen so that there are at least 10 grid points in the energetic area (where spectral values are significant). An analytical example given by Bendat and Piersol (1986) provides a quantitative confirmation for this rule: Assume an spectral density function is estimated from the response of a lightly damped single degree of freedom system to white noise. Then, the bias error will result in a reduction of less than 2%, when the resolution bandwidth, B_e, used is 4 times narrower than the half-power point bandwidth of the resonance peak.

Unlike the situation with the autospectral density estimate, suppression of the inherent bias error in the estimation procedure for cross estimates (to be discussed below) demands more segments (or in other words, lower resolution, which is not conflicting with random error suppression). The bias suppression in autospectrum estimates is, then, dominant. The actual choice of the number of the segments (and thus the frequency bandwidth resolution) is made by dividing the total record into as many segments as possible (to minimize the random error) while making sure that there are at least 10 grid points in the energy-rich range of frequencies. Following this procedure, the number of segments, n_d, have been chosen in Appendix VIII.1 to be 20 (B_e = 0.0195) with Model I and 40 (B_e = 0.0389) with Models II and II-M. Note the resolution with Model I is higher than that with Models II and II-M; this is due to the fact that the Model I spectra are more narrow-banded than those of Models II and II-M. Since 50% overlapping is applied, the actual number of segments used for spectral smoothing is 2 n_d - 1; this results in an equivalent number of segments, n_e = 9/11(2 n_d - 1), which will replace n_d in equations (IX.24) and (IX.25) for the error analysis. In the present case, the equivalent number of segments is 32 with Model I and 64 with Models II and II-M. The

corresponding equivalent number of degrees of freedom, ν_e (= $2\,n_e$), are 64 and 128 for Model I and Model II(-M) respectively - see Press, *et al.* (1986).

Substituting the n_e value for each model into equation (IX.25) yields a normalized random error, ϵ_r , of 17.7% with Model I estimates and 12.5% with Model II(-M) estimates.

Joint Record Spectral Functions

The term *Join Record Spectral Functions* here refers to the coherence function (γ^2_{xy}), the frequency response function (H_{xy}) and thus the gain factor ($|H_{xy}|$) and phase factor (θ_{xy}). These functions all link one time series to another.

With the case under investigation bias error in estimation of the joint record functions come from a number of sources:

1. Bias inherent in the estimation procedure
2. Bias due to propagation time delay
3. Bias in autospectral and cross-spectral density estimates
4. Measurement noise at the input point (no bias problem from uncorrelated noise at the output point)
5. Nonlinear and/or time varying system parameters

The first source of bias error results above from the fact that, in general,

$$E[\tilde{H}_{xy}] = E\left[\frac{\tilde{G}_{xy}}{\tilde{G}_{xx}}\right] \neq \frac{E[\tilde{G}_{xy}]}{E[\tilde{G}_{xx}]}$$

$$E[\gamma^2_{xy}] = E\left[\frac{|\tilde{G}_{xy}|^2}{\tilde{G}_{xx}\tilde{G}_{yy}}\right] \neq \frac{E[|\tilde{G}_{xy}|^2]}{E[\tilde{G}_{xx}]E[\tilde{G}_{yy}]} \qquad \text{(IX.26)}$$

Hence $E[\tilde{H}_{xy}] \neq H_{xy}$ and $E[\tilde{\gamma}^2_{xy}] \neq \gamma^2_{xy}$.

These bias errors are usually negligible compared to other possible errors that occur in practice. As either $n_e \to \infty$ or $\gamma^2_{xy} \to 1$, these inherent bias errors go to zero. For

example, an approximation for the normalized bias error inherent in the computation technique is given by Carter, *et al.* (1973):

$$b[\tilde{\gamma}_{xy}^2] \approx \frac{1}{n_e}(1 - \tilde{\gamma}_{xy}^2)^2 \tag{IX.27}$$

The second noted source of bias error occurs because: 1) The measurements might not be taken in a common time base and/or 2) The data acquisition and filtering could introduce a time shift between channels. The effect of the total time delay, τ_1, between $x(t)$ and $y(t)$ can be demonstrated by an example. Assume:

$$x(t) = x(t) \qquad 0 \le t \le T_s$$

$$y(t) = \begin{cases} \textit{arbitary} & 0 \le t \le \tau_1 \\ x(t - \tau_1) & \tau_1 \le t \le T_s \end{cases} \tag{IX.28}$$

where T_s is the segment record length. Then, to a first order of approximation, one can express the joint record function estimates by:

$$\tilde{G}_{xy}(f) \approx \left(1 - \frac{\tau_1}{T_s}\right) G_{xy}(f)$$

$$\tilde{H}_{xy}(f) \approx \left(1 - \frac{\tau_1}{T_s}\right) H_{xy}(f) \tag{IX.29}$$

$$\tilde{\gamma}_{xy}^2(f) \approx \left(1 - \frac{\tau_1}{T_s}\right)^2 \gamma_{xy}^2(f)$$

Thus the estimates of the joint record functions are biased. Nevertheless, these bias errors are significant only when τ_1 is not negligible compared with the segment length, T_s. The information about the possible time delay in the original data recording is not available. It is, however, believed that this delay would only be marginal. The delay associated with the data filtering and acquisition has been proven to be negligible. The nominal maximum delay between Channel 1 and Channel 12 is only $180 \cdot 10^{-6}$ s; this is 5 orders of magnitude lower than the shortest segment (25.2 s). Therefore, the bias errors caused by the propagation time delays in the present analysis are considered to be negligible.

The third source of bias is the 'heritage' from the bias errors in spectral density estimates. As addressed above, the bias errors in the autospectrum estimate is suppressed by making B_e sufficiently narrow to accurately define peaks in the spectra. Generally speaking, the suppression of bias in autospectrum estimate is most critical compared with other parameter estimates - see Bendat & Piersol (1986). In other words, bias suppression in an autospectrum estimates normally guarantee bias suppression in corresponding cross-spectral estimates. Hence, the bias passed on from spectral density estimates is considered negligible.

The fourth source of bias is measurement noise, $m(t)$, at the input, where this noise occurs at the input point but does not actually pass through the system. Assuming the true input to be $u(t)$, then the measured $\tilde{G}_{xx} = \tilde{G}_{uu} + \tilde{G}_{mm}$. It is not difficult to prove that the normalized bias error caused by the noise $m(t)$ is expressed as:

$$e_b[\tilde{H}_{xy}] = e_b[\tilde{\gamma}_{xy}^2] = -\left[\frac{G_{mm}}{G_{uu} + G_{mm}}\right] \qquad \text{(IX.30)}$$

Hence, the estimate will underestimate the quantity in question. For example, if $G_{mm} = 0.02\, G_{uu}$, then the resulting estimates would be biased downward by (0.02/1.02) ~ 2%. In the present physical process, the noise is expected to manifest itself in very high or very low frequencies. Since the signals have been high-pass and low-pass filtered, the noise $m(t)$ is expected to be of minor importance.

The fifth listed source of bias results from the violation of the assumption that the system is a constant-parameter linear system. The constant-parameter assumption is valid with the present case, while extensive nonlinearities exist. It should be noted, however, that the frequency response functions obtained using the spectral analysis technique will result in the best linear approximation (in the least squares sense) for that quantity under the specified input and output conditions. For different inputs, the frequency response function so determined are generally different, however.

Bias sources 1 through 4 listed above are external, caused either by the computation procedure or instrumentation. They should obviously be kept to minimum. Source 5 is inherent in the system being investigated and, in fact, is the phenomenon being sought; this bias gives an indication of the influences caused by various nonlinearities. Since the bias errors from the other four sources are marginal as addressed above, the bias found in the joint record function analysis is considered to be caused mainly by the existence of nonlinearities.

Unlike the bias errors, the random errors of the estimate (both for auto- and cross-spectral quantities) are determined by the known parameter of the analysis procedure, B_e (or in other words, n_e). The expressions for the normalized random error for coherence, gain factor and phase factor are summarized below - for detailed derivations, see Bendat and Piersol (1971) and (1986).

The normalized random error of the coherence function estimate is given by:

$$e_r[\hat{\gamma}^2_{xy}] \approx \frac{\sqrt{2}\,(1 - \gamma^2_{xy})}{|\gamma_{xy}|\sqrt{n_e}} \qquad n_e > 1 \tag{IX.31}$$

The restriction that $n_e > 1$ is needed since $\hat{\gamma}^2_{xy}(f) = 1$ when $n_e = 1$ independent of the actual coherence and gives a meaningless estimate for γ^2_{xy}. The failure to note this important fact is the source of a common mistake in coherence function analysis. When spectral density estimates are obtained to calculate coherence functions, one might tend to postpone the required smoothing operations on the spectral densities in favor of a single smoothing of the resulting coherence function estimate. Unfortunately, such an approach will produce a coherence function estimate of unity, even for the case of totally incoherent data.

The normalized random error of the gain factor estimate is written as:

$$e_r[|\hat{H}_{xy}|] \approx \frac{\sqrt{1 - \gamma^2_{xy}}}{|\gamma_{xy}|\sqrt{2n_e}} \tag{IX.32}$$

Random errors of phase factor estimates should not be normalized, since θ_{xy} may be zero. Instead, the standard deviation of the estimate is used:

$$s.d.[\hat{\theta}_{xy}] \approx \frac{\sqrt{1 - \gamma^2_{xy}}}{|\gamma_{xy}|\sqrt{2n_d}} \tag{IX.33}$$

where $\tilde{\theta}_{xy}$ is measured in radians.

It is interesting to note that:

$$s.d.[\tilde{\theta}_{xy}] \approx e[|\tilde{H}_{xy}|] \qquad \text{(IX.34)}$$

A common tendency for the joint record function estimates can be found by examining equations (IX.31) through (IX.33). Their random errors approach zero, either as $\tilde{\gamma}^2_{xy} \to 1$ (independent of the size of n_e), or as $n_e \to \infty$ (independent of the value of $\tilde{\gamma}^2_{xy}$).

IX.4 CONFIDENCE INTERVALS OF SPECTRAL ESTIMATES

When estimating an arbitrary random variable ϕ, if for a prescribed (small) probability, α, an interval (ϕ_1, ϕ_2) can be found so that:

$$Prob[\phi_1 < \phi < \phi_2] = 1 - \alpha \qquad \text{(IX.35)}$$

then the interval (ϕ_1, ϕ_2) is called a confidence interval with a confidence coefficient of $1 - \alpha$, or in more common terminology, with a confidence of $100(1 - \alpha)\%$. The probability, α, is called the level of significance.

The confidence coefficient is chosen to be 0.95 ($\alpha = 0.05$), or in other words, the confidence interval is assessed with a confidence of 95%.

The confidence interval is another important measure to assess the accuracy of estimates. It gives a vivid illustration of the scope of likely true values. The determination of the confidence interval is dependent upon the probability distribution of the estimates.

Autospectrum

The sampling distribution of an estimate of autospectral density function smoothed according to the procedure used in the study is approximately a *Chi*-Square Distribution with ν_e degrees of freedom. Hence a $(1 - \alpha)$ confidence interval for a power spectral density function, $G_{xx}(f)$, based upon an estimate $\tilde{G}_{xx}(f)$ is given by:

$$\left[\frac{\nu_e \tilde{G}_{xx}(f)}{\chi^2_{\nu_e;\,\alpha/2}} \leq G_{xx}(f) < \frac{\nu_e \tilde{G}_{xx}(f)}{\chi^2_{\nu_e;\,1-\alpha/2}} \right] \qquad \text{(IX.36)}$$

Here, ν_e is 64 with Model I. From the Table of Percentage Points of the *Chi*-Square Distribution it is known that $\chi^2_{64;\,0.025} = 87.89$ and $\chi^2_{64;\,0.975} = 43.89$. Substituting these data into equation (IX.36) yields:

$$\left[0.73\ \tilde{G}_{xx}(f) \leq G_{xx}(f) < 1.46\ \tilde{G}_{xx}(f) \right] \qquad \text{(IX.37)}$$

for Model I.

With Models II and II-M ν_e is 128. When $\nu_e > 120$, the χ^2 percentage is calculated by:

$$\chi^2_{\nu_e;\alpha} \approx \nu_e \left[1 - \frac{2}{9\nu_e} + z_\alpha \sqrt{\frac{2}{9\nu_e}} \right]^3 \qquad \text{(IX.38)}$$

where z_α is the desired percentage point for a Standard Normal Distribution. From the Table of Percentage Points of the Standard Normal Distribution follows that z_α is equal to 1.96 and - 1.96 for $\alpha = 0.025$ and $\alpha = 0.975$, respectively. Thus from equations (IX.36) and (IX.38):

$$\left[0.79\ \tilde{G}_{xx}(f) \leq G_{xx}(f) < 1.29\ \tilde{G}_{xx}(f) \right] \qquad \text{(IX.39)}$$

for Models II and II-M.

Coherence Function

Estimates of the coherence function in the range $0.35 \leq \gamma^2_{xy}$ based upon spectral density estimates with $\nu_e \geq 20$ degrees of freedom can be evaluated in terms of the transform:

$$w(f) = \frac{1}{2} \ln \left[\frac{1 + \tilde{\gamma}_{xy}(f)}{1 - \tilde{\gamma}_{xy}(f)} \right] = \operatorname{argtanh} \tilde{\gamma}_{xy}(f) \qquad \text{(IX.40)}$$

where $w(f)$ has an approximately normal distribution with a mean and variance of

$$\mu_w(f) = (\nu_e - 2)^{-1} + \operatorname{argtanh} \gamma_{xy}(f) \qquad \text{(IX.41)}$$

$$\sigma_w^2 = (\nu_e - 2)^{-1} \qquad \text{(IX.42)}$$

From the preceding equations, the $(1 - \alpha)$ confidence interval for a coherence function, $\gamma^2_{xy}(f)$, based upon an estimate $\hat{\gamma}^2_{xy}(f)$ can be established as follows: Because $w(f)$ is normally distributed:

$$Prob\left[z_{1-\alpha/2} < \frac{w(f) - \mu_w(f)}{\sigma_w} \leq z_{\alpha/2}\right] = 1 - \alpha \qquad \text{(IX.43)}$$

where z_α is the 100α percentage point of the Standardized Normal Distribution. In equation (IX.43), $\mu_w(f)$ and σ_w can now be replaced by equations (IX.41) and (IX.42). After rearranging terms, the resulting $(1 - \alpha)$ confidence interval of $\gamma^2_{xy}(f)$ is found to be:

$$\begin{aligned}[\ \tanh^2\{w(f) - (\nu_e - 2)^{-1} - (\nu_e - 2)^{-1/2} z_{\alpha/2}\} < \gamma^2_{xy}(f) \\ \leq \tanh^2\{w(f) - (\nu_e - 2)^{-1} + (\nu_e - 2)^{-1/2} z_{\alpha/2}\}\ ]\end{aligned} \qquad \text{(IX.44)}$$

For $\alpha/2 = 0.025$, $z_{\alpha/2} = 1.96$. The equivalent number of degrees of freedom, ν_e, is 64 and 128 with Model I and Model II(-M), respectively. Applying these data to equation (IX.44) yields:

$$\begin{aligned} &\textit{Model I} \quad : \quad [\tanh^2(w(f) - 0.183) < \gamma^2_{xy} \\ &\qquad\qquad\qquad\quad \leq \tanh^2(w(f) + 0.167)] \\ &\textit{Model II(-M)} \quad : \quad [\tanh^2(w(f) - 0.127) < \gamma^2_{xy} \\ &\qquad\qquad\qquad\quad \leq \tanh^2(w(f) + 0.119)] \end{aligned} \qquad \text{(IX.45)}$$

Gain Factor and Phase Factor

A confidence interval for a frequency response function estimate with confidence coefficient $1 - \alpha$ can be determined by a quantity $\Delta(f)$:

$$|\tilde{H}_{xy}(f) - H_{xy}(f)|^2 \leq \Delta^2(f)$$

$$\Delta^2(f) = \frac{2}{\nu - 2} F_{2,\nu-2;\alpha} [1 - \tilde{\gamma}^2_{xy}(f)] \frac{\tilde{G}_{yy}(f)}{\tilde{G}_{xx}(f)} \tag{IX.46}$$

where $F_{2,\nu-2;\alpha}$ is the 100α percentage points of an F Distribution with $n1 = 2$ and $n2 = \nu - 2$ degrees of freedom. In the present case, ν should be replaced by ν_e to count the extra accuracy gained by overlapping. It is found from the Table of Percentage Points of the F Distribution that $F_{2,62;0.05} = 3.14$ (Model I) and $F_{2,126;0.05} = 3.08$ (Models II and II-M). Applying these data, $\Delta^2(f)$ becomes:

$$\Delta^2(f) = 0.101 [1 - \tilde{\gamma}^2_{xy}(f)] \frac{\tilde{G}_{yy}(f)}{\tilde{G}_{xx}(f)} \tag{IX.47}$$

for Model I and

$$\Delta^2(f) = 0.048 [1 - \tilde{\gamma}^2_{xy}(f)] \frac{\tilde{G}_{yy}(f)}{\tilde{G}_{xx}(f)} \tag{IV.48}$$

for Models II and II-M.

Geometrically, equations (IX.46) describes a circle of radius $\Delta(f)$ centered at $\tilde{H}_{xy}(f)$. In terms of the gain factor and phase factor estimates, the approximate $1 - \alpha$ confidence intervals for the gain factor, $|H_{xy}(f)|$, and phase factor, $\theta_{xy}(f)$, are now given at each frequency, f, by:

$$\begin{bmatrix} |\tilde{H}_{xy}(f)| - \Delta(f) \leq |H_{xy}(f)| \leq |\tilde{H}_{xy}(f)| + \Delta(f) \end{bmatrix}$$
$$\begin{bmatrix} \tilde{\theta}_{xy}(f) - \Delta\tilde{\theta}(f) \leq \theta_{xy}(f) \leq \tilde{\theta}_{xy}(f) + \Delta\tilde{\theta}(f) \end{bmatrix} \tag{IX.49}$$

where $\Delta(f)$ is the positive square root of $\Delta^2(f)$ defined in equation (IX.46), and

$$\Delta\tilde{\theta}(f) = \text{argsin}\left[\frac{\Delta(f)}{|\tilde{H}_{xy}(f)|}\right] \tag{IX.50}$$